

Extracellular Matrix- and Pluripotent Stem Cell-based Tissue Engineering of the Kidney

vorgelegt von
Dipl.-Ing.
Iris Fischer

an der Fakultät III - Prozesswissenschaften
der Technischen Universität Berlin
zur Erlangung des akademischen Grades

Doktor der Ingenieurwissenschaften
- Dr.-Ing. -

genehmigte Dissertation

Promotionsausschuss:

Vorsitzender: Prof. Dr. Jens Kurreck
Gutachter: Prof. Dr. Roland Lauster
Gutachter: Dr. Andreas Kurtz

Tag der wissenschaftlichen Aussprache: 27.11.2019

Berlin 2020

„Indes sie forschten, röntgten, filmten, funkten,
entstand von selbst die köstlichste Erfindung:
der Umweg als die kürzeste Verbindung
zwischen zwei Punkten.“

Erich Kästner

Zusammenfassung

Komplexe, dreidimensionale (3D) Organmodelle sind neuartige biotechnologische Werkzeuge für die Erforschung von Regenerations- und Krankheitsmechanismen sowie für die Medikamentenentwicklung. Ein solches Modell der Niere könnte die jahrzehntelange Stagnation in der Entwicklung neuer Behandlungsmethoden für Patienten mit chronischem Nierenversagen durchbrechen, sowie die hohe Durchfallrate neuer Medikamente in klinischen Tests durch nephrotoxische Effekte reduzieren. Ziel der vorliegenden Arbeit war daher die Entwicklung eines humanen 3D Nierenmodelles.

Ein funktionsfähiges Nierenmodell sollte die Architektur und die Zelltypen der Niere, sowie die mechanischen Eigenschaften und die Zusammensetzung der extrazellulären Matrix nachahmen und zudem perfundiert sein. Daher wurde ein Scaffold-basierter Ansatz der Gewebezüchtung auf der Basis von dezellularisierten ganzen Rattennieren gewählt, die mit humanen Nierenvorläuferzellen und Endothelzellen, differenziert aus induzierten pluripotenten Stammzellen, rezellularisiert werden sollten.

Dieser Ansatz machte die Entwicklung eines Perfusionsbioreaktors und einer Steuerungssoftware nötig, die die De- und Rezellularisierung der Nieren sowie die darauffolgende *In-vitro*-Kultivierung erst ermöglichten.

Dezellularisierung ist die Entfernung aller Zellen eines Organs, bei der die extrazelluläre Matrix (EZM) in ihrer nativen Architektur und Zusammensetzung erhalten bleibt. In dieser Arbeit wurde durch den Vergleich des Einflusses verschiedener Detergenzien sowie Temperaturen gezeigt, dass für die Dezellularisierung von Nierengewebsstücken das Untertauchen in dem milden ionischen Detergens Natriumdesoxycholat (SDC) bei 4 °C optimal ist. Für die Dezellularisierung ganzer Nieren durch Perfusion ist jedoch das starke ionische Detergens Natriumdodecylsulfat (SDS) nötig. Sowohl die Minimierung der SDS-Konzentration und -Anwendungsdauer als auch der Temperatur während der Dezellularisierung verbessern dabei die Qualität der dezellularisierten EZM. Alle Ergebnisse wurden mittels eines punktebasierten Bewertungssystems, welches ebenfalls im Rahmen dieser Arbeit entwickelt wurde, objektiv und standardisiert beurteilt.

Um eine effiziente Rezellularisierungsstrategie zu identifizieren wurden Zellen mit oder ohne Hochdruck durch die Nierenarterie, mit oder ohne Vakuum durch den Ureter oder

durch eine direkte Injektion in die dezellularisierten Nieren eingesät. Der Gefäßbaum konnte erfolgreich mit Endothelzellen, die durch die Nierenarterie eingesät wurden, rezellularisiert werden. Die Rezellularisierung des Parenchyms mit Nierenvorläuferzellen resultierte jedoch mit allen getesteten Rezellularisierungsstrategien in geringen Wiederbesiedlungseffizienzen. So konnten maximal 1% des Parenchyms wiederbesiedelt werden, zudem entstanden Schäden in der Architektur und die Anordnung der Zellen entsprach nicht den physiologischen renalen Strukturen.

Parallel dazu wurde der Einfluss der mechanischen und biochemischen Eigenschaften der EZM auf die Ausreifung der Nierenvorläuferzellen untersucht. Dazu wurden diese auf Oberflächen verschiedener Steifigkeiten und EZM-Beschichtungen kultiviert. Mit steigender Steifigkeit reifen die Nierenvorläuferzellen zunehmend in renale Tubulusepithelzellen aus, wohingegen sich die Podozytenausreifung invers verhält. Zudem wurde nachgewiesen, dass das EZM-Protein Laminin, im Gegensatz zu Collagen IV, die Ausreifung der Nierenvorläuferzellen in renale Tubulusepithelzellen fördert, wobei zwischen den Laminin-Isoformen 511 und 521 kein Unterschied besteht.

Auch wenn mit den gewählten Methoden kein Nierenmodell generiert werden konnte, so markieren doch die technischen Entwicklungen und die Erkenntnisse, die in dieser Arbeit gewonnen worden, einen weiteren Schritt in Richtung eines humanen 3D Nierenmodells.

Abstract

Complex, three-dimensional (3D) organ models are novel biotechnological tools for research on regeneration and disease mechanisms as well as drug development. An organ model of the kidney is urgently needed to break through decades of stagnation in the development of new treatment methods for patients with chronic kidney disease and to reduce the high failure rate of drugs in clinical tests due to nephrotoxic effects. The aim of this thesis was therefore the development of a human 3D kidney model.

A functional kidney model should emulate the architecture and cell types of the kidney, as well as the mechanical properties and composition of the extracellular matrix. In order to emulate the function of the kidney, the model must be perfused. Therefore, a scaffold-based tissue engineering approach was chosen on the basis of decellularized whole rat kidneys, which should be recellularized with human renal precursor cells and endothelial cells differentiated from induced pluripotent stem cells.

This approach required the development of a perfusion bioreactor and control software, which enabled the de- and recellularization of the kidneys as well as the subsequent *in vitro* cultivation.

Decellularization is the process of removing all cells of an organ while preserving the extracellular matrix (ECM) in its native architecture and composition. The influence of different detergents and temperatures was analyzed, and the results showed that for the decellularization of tissue pieces immersion in the mild ionic detergent sodium deoxycholate (SDC) at 4 °C is optimal. However, decellularization of whole kidneys by perfusion required the strong ionic detergent sodium dodecyl sulfate (SDS). To improve the quality of the decellularized ECM it is beneficial to minimize the SDS concentration and application time as well as the temperature. All results were evaluated objectively and standardized by applying a point-based scoring system, which was also developed in the course of the thesis. Next, an efficient recellularization strategy had to be identified. The tested strategies included cell seeding through the renal artery with or without high pressure, seeding through the ureter with or without vacuum and direct injection into the parenchyma with a syringe. The vascular tree of the decellularized kidney was successfully recellularized with endothelial cells seeded via the renal artery. However, recellularization of the parenchyma with renal progenitor cells resulted in low seeding efficiencies in all applied seeding

approaches. A maximum of 1% of the parenchyma could be repopulated by recellularization. In addition, the recellularization caused damage to the scaffold architecture and the arrangement of the cells did not correspond to the physiological renal structures.

In parallel, the influence of mechanical and biochemical properties of the ECM on the maturation of renal progenitor cells was investigated. The cells were cultivated on surfaces of different stiffnesses and ECM coatings. With increasing stiffness, the renal progenitor cells increasingly matured into renal tubular epithelial cells, whereas podocyte maturation behaved inversely. In addition, the analysis revealed that the ECM protein laminin, in contrast to collagen IV, promotes the maturation of renal progenitor cells into renal tubular epithelial cells, although no difference was detected between the laminin isoforms 511 and 521.

Although no kidney model could be generated with the investigated methods, the technical developments and the findings of this thesis mark a further step on the way to a human 3D kidney model.

Content

1 INTRODUCTION.....	1
1.1 The need for better <i>in vitro</i> kidney models	1
1.2 The kidney	2
1.2.1 Functions, cell types and architecture of the kidney.....	2
1.2.2 Extracellular matrix of the kidney	5
1.2.3 Renal organogenesis.....	12
1.3 Tissue engineering of the kidney.....	13
1.3.1 Cell source.....	14
1.3.2 Architecture and perfusion	16
1.3.3 De- and recellularization	18
2 AIM	22
3 MATERIALS AND METHODS.....	23
3.1 Materials.....	23
3.1.1 Cells.....	23
3.1.2 Reagents	23
3.1.3 Consumables	25
3.1.4 Kits	26
3.1.5 Antibodies and fluorescent dyes.....	27
3.1.6 qPCR gene expression assays.....	27
3.1.7 Instruments.....	27
3.1.8 Software and data bases	29
3.2 Methods	30
3.2.1 Cell culture	30
3.2.2 Decellularization of porcine kidney tissue by immersion and agitation	34
3.2.3 Decellularization of whole rat kidneys by perfusion.....	35
3.2.4 Characterization of decellularized kidneys.....	38
3.2.5 Recellularization of immersion-decellularized porcine kidney scaffolds.....	40
3.2.6 Recellularization of perfusion-decellularized whole rat kidneys.....	40
3.2.7 Characterization of recellularized kidneys	42
3.2.8 Tuning of the pressure and pH controllers	43
3.2.9 PDMS gel assay	44
3.2.10 Quantitative polymerase chain reaction	45
3.2.11 Histology and immunofluorescence staining.....	46
3.2.12 Flow cytometry	48
3.2.13 Statistical analysis	49
4 RESULTS	50
4.1 Development of a perfusion bioreactor for de- and recellularization of whole kidneys	50
4.1.1 Setup.....	50
4.1.2 Software development for the control of the perfusion bioreactor	53
4.1.3 Tuning the controllers of the perfusion bioreactor	57

4.2 Identification of an optimal decellularization strategy for kidney tissue using factor screening in an immersion and agitation setting	66
4.2.1 Analysis of histology and composition after decellularization by immersion and agitation	67
4.2.2 Biocompatibility testing of immersion-decellularized kidney tissue by recellularization with intermediate mesoderm cells	72
4.2.3 A scoring system facilitates the comparison of immersion-decellularization strategies	75
4.3 Decellularization of kidneys by perfusion.....	77
4.3.1 Analysis of histology and composition after decellularization by perfusion.....	78
4.3.2 Biocompatibility testing of perfusion-decellularized kidneys by reendothelialization with human umbilical vein endothelial cells.....	80
4.3.3 Applying the scoring system for the comparison of perfusion-decellularization methods.....	83
4.4 Recellularization of perfusion-decellularized kidneys	86
4.4.1 Reendothelialization with hiPSC-derived endothelial cells.....	87
4.4.2 Recellularization of the kidney parenchyma with hiPSC-derived renal progenitor cells	90
4.5 The effect of stiffness and ECM composition on renal progenitor cell maturation	97
4.5.1 Optimization of PDMS gels for cell culture.....	98
4.5.2 Investigation of renal progenitor cell maturation	99
5 DISCUSSION	103
5.1 The perfusion bioreactor enables kidney de- and recellularization	104
5.2 Kidney decellularization.....	107
5.2.1 The decellularization scoring system standardizes the evaluation of decellularization results ..	107
5.2.2 The effect of the detergent on kidney decellularization by immersion.....	108
5.2.3 The effect of the temperature on kidney decellularization by immersion	111
5.2.4 Decellularization outcomes by perfusion differ to decellularization outcomes by immersion...	112
5.3 Generation of an <i>in vitro</i> kidney model by recellularization of decellularized kidneys	115
5.3.1 Successful reendothelialization of the renal vascular tree	115
5.3.2 Inefficient recellularization of the renal parenchyma.....	117
5.4 Stiffness and composition of the cell culture surface influence renal progenitor cell maturation	120
6 OUTLOOK.....	123
7 REFERENCES.....	125
8 APPENDIX	136
8.1 Supplemental information.....	136
8.2 Abbreviations	138
8.3 List of figures.....	140
8.4 List of tables	142
8.5 Acknowledgements	143

1 Introduction

1.1 The need for better *in vitro* kidney models

The kidney is the main excretory organ of the human body. It eliminates not only metabolic waste products, such as urea, uric acid or ammonia, but also toxins and drugs via the urine. Furthermore, it regulates water, mineral and acid-base homeostasis and acts as an important endocrine organ. It produces the hormones erythropoietin and thrombopoietin and thereby stimulates the generation of erythrocytes and platelets. Additionally, the kidney secretes the hormones renin and angiotensin-converting enzyme, which regulate blood pressure via the renin-angiotensin-aldosterone system¹.

Despite its extensive functions and great importance for the human body, the human kidney possesses a strictly limited capacity to regenerate after injury. Although cellular regeneration can reconstitute injured portions of existing nephrons, the kidney's functional units, repeated kidney injury will eventually lead to the loss of this repair capacity. Moreover, there is no nephrogenesis after birth in humans. Thus, no new nephrons arise after injury to compensate for the damage. Fortunately, under normal circumstances, the number of nephrons at birth is sufficient to maintain kidney function throughout the human lifetime, despite the lack of kidney regeneration. At the age of 60, however, their number has halved²⁻⁴.

When, in addition to the normal aging process, diseases, such as diabetes, hypertension or glomerulonephritis, damage the kidney, chronic kidney disease (CKD) can develop. CKD progresses gradually and culminates in complete renal failure, called end-stage renal disease (ESRD). Around 10% of the population suffer from CKD of which 90% are older than 65 years. The CKD prevalence is expected to rise dramatically with the ongoing aging of the population^{5,6}.

The treatment of renal failure has hardly changed in the last decades and dialysis and transplantation are still the only two treatment options. Hemodialysis is an artificial blood filtration system that substitutes the excretory function of the kidney. In the European Union about 400,000 patients rely on this treatment. However, these patients suffer from side effects, such as fatigue, headaches or low blood pressure, are vulnerable to infections and

have to attend three 4-hour sessions weekly to survive, and still have a reduced life expectancy^{5,7}. A better long-term survival and quality of life can be achieved by kidney transplantation. However, there is a dramatic shortage of donor organs. Moreover, transplant patients rely on immunosuppressive treatment to prolong the transplant's function, which increases their risk to develop cancer or diabetes. Since the underlying kidney damaging disease is often still active after transplantation, transplants will only stay functional for an average of 10 years, despite this immunosuppressive treatment and human leukocyte antigen matching before donor selection⁵.

The need for new therapies for kidney failure is therefore evident. However, countless studies in human patients, in animal models or in two-dimensional (2D) cell culture models have not achieved this goal⁸.

Moreover, these models too often fail when they are applied in preclinical screenings, since about 7% of drug candidates entering a clinical trial fail due to drug-induced nephrotoxicity. Only 8% of drugs pass these extremely expensive and time-consuming clinical trials^{8,9}.

Thus, a novel 3D human kidney model that facilitates the study of disease mechanisms, the development of new drugs, cell therapies or organ replacement strategies is urgently needed. To date no human kidney model has been developed that includes all renal cell types and shows the correct renal architecture and functions, yet the medical need demands a fast implementation. The development of such a model is therefore the major aim of this thesis.

1.2 The kidney

Before attempting to build a kidney model *in vitro*, it is necessary to fully understand function, architecture, composition and organogenesis of the kidney *in vivo*.

1.2.1 Functions, cell types and architecture of the kidney

The kidney is a paired, bean-shaped organ with a highly specialized architecture. These complex structures and the more than 20 different renal cell types are essential for the manifold renal functions¹⁰.

The functional unit of the kidney is the nephron, consisting of a glomerulus and renal tubule that drains into the collecting duct. A human kidney contains approximately 1 million nephrons¹¹.

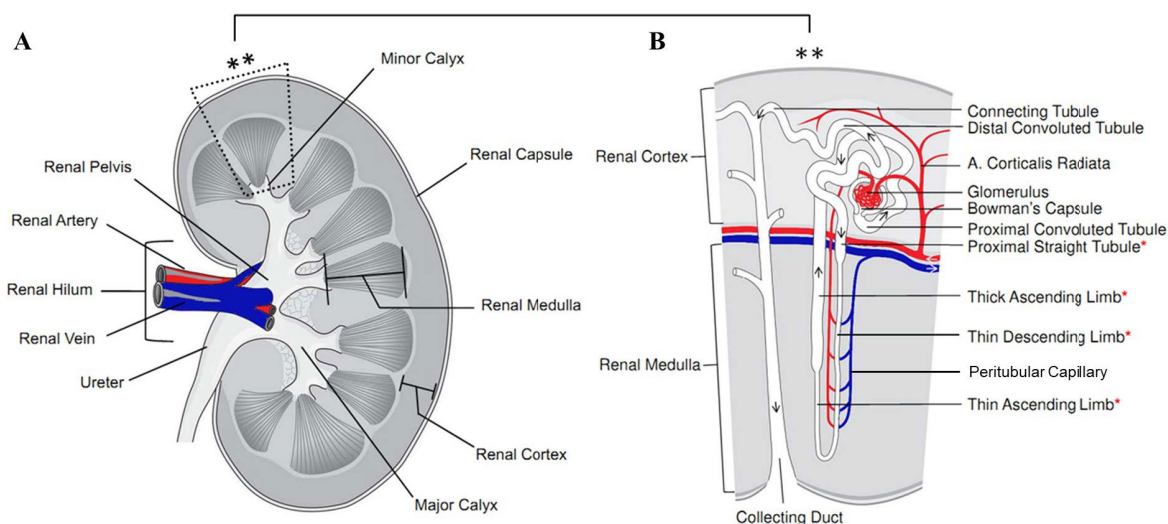


Figure 1: Anatomy of the human kidney. (A) The human kidney is a multilobular, bean-shaped organ. Macroscopically it is subdivided into cortex, medulla and pelvis, as marked. (B) Magnification of one lobule, showing one nephron, collecting duct and the vascular network, as labeled. * indicate sections that are part of the loop of Henle. Figure adapted from Westphal 2012¹², images reproduced from CellFinder database¹³.

Glomeruli are the filtration units of the kidney and are located in the cortex. The glomerulus is composed of a capillary bundle surrounded by the double-walled epithelial Bowman's capsule. The filtration barrier is formed from three layers. The first layer is formed by specialized endothelial cells that line the capillary's lumen. Their cell bodies are highly fenestrated and covered in a thick glycocalyx^{14,15}. Their basal side is attached to the unique glomerular basement membrane (GBM), the second filtration layer. The third layer of the filtration barrier is built by podocytes that line the opposite side of the GBM. Podocytes are a highly specialized epithelial cell type. Their interdigitated foot processes form the slit diaphragm. All layers are highly negatively charged by the deposition of the polyanionic glycoprotein podocalyxin^{16,17}. When blood flows from the afferent arteriole through the capillary bundle and out through the efferent arteriole, these three layers work like a filter through which only molecules smaller than 50 kDa can pass.

This filtration process produces 150 l of primary urine daily in an average adult human. The primary urine drains into the tubular part of the nephron. The task of the tubule is to reabsorb

99% of the filtered water and 90% of the solutes of the primary urine to generate the 1,5 l of final urine daily^{1,18}.

The proximal tubule is the first part of the tubule system after the glomerulus. It is convoluted and lined with cuboidal epithelium. The apical surface of the epithelium displays a characteristic brush boarder surface and the basal side is characterized by interdigitating basolateral folds. Both properties multiply the surface area of the cells and permit the fast reabsorption of water, glucose, NaCl and amino acids and secretion of drugs and ammonia into the primary urine. Basolaterally located, the sodium potassium-pump (Na^+/K^+ -ATPase) produces the ion gradient that powers the secondary active transport on the apical side by symporters for Na^+ , glucose, amino acids etc.¹⁹. Water reabsorption is a passive process. Water follows the Na^+ gradient that is maintained by the Na^+/K^+ -ATPase through the water channel aquaporin 1 (AQP1). Tubular epithelial cells secrete the reabsorbed substances into the basolaterally located renal interstitium. The tubules are surrounded by peritubular capillaries that absorb these substances and reintroduce them into the bloodstream^{20,21}.

Next, the loop of Henle dips down into the medulla. It is lined by thin epithelial cells without a brush boarder. The descending part of the loop is water permeable whereas the ascending part is water impermeable. Only in the ascending part the Na^+/K^+ -ATPase powers the ion uptake by the Na-K-Cl cotransporter. The ions pass into the interstitial space through basolateral channels, making the medulla salty. This drives the passive water reabsorption and further concentration of the urine in the descending loop of Henle^{1,18,22}.

The fluid passes next through the distal tubule, where the urine composition is fine-tuned. More ions are resorbed but in contrast to the earlier tubule parts, here the resorption is regulated. For example, the Ca^{2+} resorption is regulated by the parathormone (PTH). Furthermore, the distal tubule is part of the juxtaglomerular complex, a structure close to the glomerulus that senses the blood pressure and releases the hormone renin in response^{1,18,23}. Renin triggers the renin-angiotensin-aldosterone system (RAAS), a hormone system that regulates the systemic blood pressure and volume.

Multiple distal tubules drain into one collecting duct that regulates the final water resorption. Like the distal tubule, the collecting duct is susceptible to aldosterone and the antidiuretic hormone (ADH), two hormones that are part of the RAAS. Aldosterone, produced in the adrenal gland, increases the amount of Na^+/K^+ -ATPase, thereby causing Na^+ reabsorption which is followed by passive water reabsorption. ADH, produced in the pituitary gland, increases the expression of the water channel aquaporin 2 in the collecting duct. Both

hormones therefore decrease the amount of water that is otherwise lost with the urine and hence raise the blood pressure^{1,18,24}. Erythropoietin is produced by interstitial renal fibroblasts that surround the nephrons²⁵.

The final urine is drained from the collecting ducts into the renal pelvis, through the ureter into the bladder.

In conclusion, a functional *in vitro* kidney model can only be achieved, when the architecture of the nephron is fully emulated, when all renal cell types are arranged correctly and when the nephron is perfused.

1.2.2 Extracellular matrix of the kidney

The extracellular matrix (ECM) surrounds cells with a complex network of approximately 300 different proteins, glycosaminoglycans, ECM-binding growth factors and ECM-modifying enzymes²⁶.

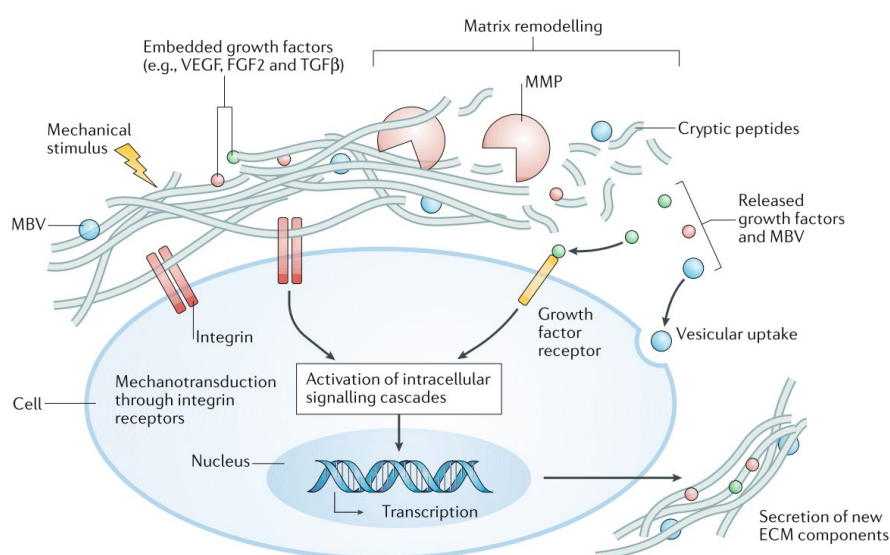


Figure 2: Interactions of cells with their surrounding ECM. Cells and ECM exist in dynamic reciprocity. The ECM provides structure and stability to tissues. Moreover, it provides mechanical and biochemical stimuli to the cells, thus activating intracellular signaling cascades and influencing gene expression. Cells secrete ECM components and matrix metalloproteinases (MMPs) to remodel the existing matrix and to release matrix bound vesicles (MBV), growth factors and cryptic peptides carrying epidermal growth factor-like (EGF) domains. Figure reproduced from Hussey et al.²⁷.

The ECM is well-known for its role to provide structural support for organs and tissues. In the last years, however, it became clear that this drastically underestimated the extent of its functions. The ECM also signals to the cells in various mechanisms, as depicted in Figure 2, and thereby influences cell survival, differentiation, proliferation, polarity, shape and motility^{26,28}.

Firstly, the ECM provides biochemical signals to the cells. Signaling molecules, such as ECM-bound growth factors, matrix bound vesicles (MBVs) and cryptic epidermal growth factor (EGF)-like domains, are released upon ECM degradation with matrix metalloproteinases (MMPs). Hence, the ECM acts as a reservoir for signaling molecules, regulates their distribution, activation and presentation to cells and establishes crucial growth factor gradients that pattern the developmental processes^{28,29}. Moreover, the ECM macromolecules provide biochemical signals to the cells. Cells in different segments of the nephron receive different signals from these molecules, since the ECM composition in the kidney is specific for every segment, as discussed in more detail in 1.2.2.1^{30,31}.

Secondly, the ECM provides mechanical stimuli to the cells. Mechanical characteristics of the cell-surrounding environment, such as stiffness, shape or shear stress, influence proliferation, apoptosis, differentiation and migration, as described in more detail in 1.2.2.2³².

The importance of the ECM is highlighted by the manifold diseases that are caused by ECM defects. Mutations, degradation, hyperproduction or compositional changes of the ECM cause or accompany numerous renal pathologies.

Genetic diseases of the ECM in the kidney include the Alport syndrome or the Pierson syndrome. Both diseases affect the integrity of the GBM and lead to proteinuria³³. Mutations in ECM proteins that are irreplaceable for proper ECM assembly result in embryonic lethality³⁴.

Non-genetic dysregulation of the kidney ECM composition, stiffness or structure contributes to renal fibrosis and invasive cancer³⁵. Interstitial kidney fibrosis is the main driver of kidney failure in end-stage renal disease. In kidney fibrosis, myofibroblasts produce large amounts of fibrillar collagen and replace thereby the functional parenchyma of the organ^{36,37}. The progression of cancer is also influenced by the state of the ECM, a concept pioneered by Mina Bissell. Cell transplantation experiments revealed that healthy ECM provides tumor-suppressive signals and can prevent malignant phenotypes even in cells with multiple

genomic abnormalities. Conversely, an altered ECM microenvironment can act as a potent tumor promoter^{38,39}.

1.2.2.1 Composition of the extracellular matrix of the kidney

The renal ECM can be divided into interstitial ECM and basement membranes³⁵, as shown in Figure 3A.

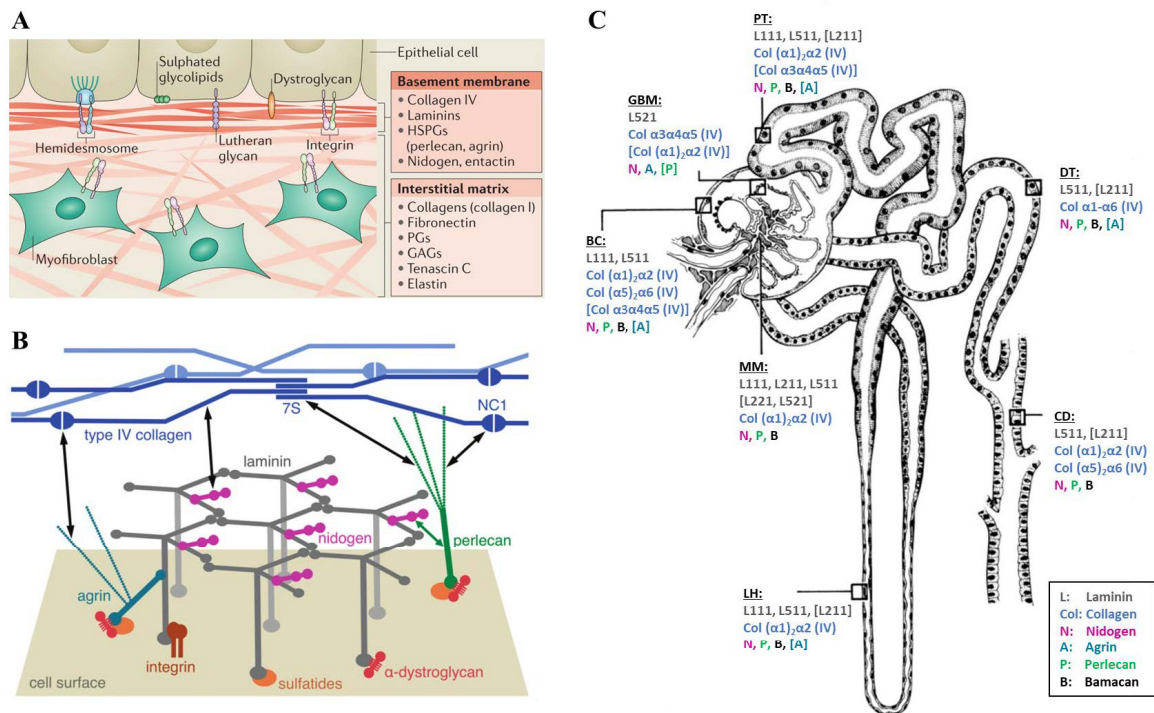


Figure 3: Structure and composition of renal basement membranes (A) The two main types of ECM. Interstitial matrix is a loose fibrillar network surrounding the cells, composed of mainly collagen I and fibronectin. The more compact basement membranes (BM) underline epithelia. Reproduced from Bonnans³⁵. (B) Model of the molecular structure of the BM. Laminin and collagen IV form independent networks that are interconnected by nidogen and the HSPGs agrin and perlecan (black double-headed arrows). The epithelial cells are anchored to the BM through integrins, α -dystroglycans and sulfated carbohydrates. Reproduced from Hohenester⁴⁰. (C) The composition of the basement membranes of the nephron is segment-specific. GBM, glomerular basement membrane; MM, mesangial matrix; BC, Bowman's capsule; PT, proximal tubule; LH, loop of Henle; DT, distal tubule; CD, collecting duct. Reproduced from Miner³¹.

The interstitial ECM is a fibrillar network that fills the zones between glomeruli, tubules, ducts and vessels. For instance, mesangial cells located between the glomerular capillary loops produce the mesangial ECM. Its main components are fibrillar collagens, fibronectin, proteoglycans, GAGs, tenascin C and elastin³⁵. In a healthy kidney this ECM compartment is less prominent than the basement membrane compartment.

A basement membrane (BM) is a thin sheet of extracellular matrix that is located at the basal side of every epithelium; it also ensheathes cardiac, smooth and skeletal muscle fibers and outlines Schwann and vascular endothelial cells. In the glomeruli, the glomerular basement membrane is part of the filtration barrier. The Bowman's capsule is covered by a basement membrane. In the tubulointerstitium, all tubules are lined with segment-specific tubular basement membranes and also peritubular capillaries are covered by a basement membrane^{31,37}. Importantly, the BM composition differs depending on the part of the nephron, as depicted in Figure 3C. This contributes to the functional specificity in distinct nephron segments³¹. BMs are mainly composed of laminin, collagen IV, nidogen, and heparan sulfate proteoglycans⁴¹:

Laminin is a large multidomain glycoprotein consisting of one α , β and γ chain. 16 different laminin isoforms have been identified to date, each with a characteristic tissue distribution^{42,43}. The molecule self-assembles into polymers that build layered sheets, anchors the BM to the cells and is crucial in the organization and assembly of the BM^{40,43,44} (see Figure 3B).

Laminin 111 (Lam-1, L111) is the most abundant laminin type in the human body. It is composed of the $\alpha 1$, $\beta 1$ and $\gamma 1$ chain, as encoded in the name. It is the first laminin trimer that arises during kidney development⁴⁴⁻⁴⁷. In the adult nephron, laminin 111 is part of the mesangial matrix as well as of the BMs in the proximal tubule, the loop of Henle and the Bowman's capsule³¹.

Laminin 511 (Lam-10, L511) is the most abundant laminin trimer in the adult kidney and is part of the BM of all tubules and collecting ducts but not of the mature GBM³¹. A deficiency of the $\alpha 5$ chain leads to a defect in GBM assembly during glomerulogenesis⁴⁴⁻⁴⁶.

In the kidney, the $\beta 2$ chain is solely expressed in the GBM. Laminin 111 and 511 trimers are eliminated during organogenesis, hence laminin 521 (Lam-11, L521) is the only laminin type present in the GBM. A null mutation in the coding gene *LAMB2* leads to the development of the Pierson syndrome. Newborns carrying this mutation die within two weeks after birth due to renal failure. This early onset of proteinuria strongly suggests that laminin 521 is crucial for the correct function of the filtration barrier⁴⁸⁻⁵⁰.

Collagen IV (ColIV) forms a second network in the basal membrane that is crucial for BM stability. The ColIV molecule is formed by three α chains, twisted into a triple helix. There

are six genetically distinct α chains. They trimerize into $(\alpha 1)_2\alpha 2$ (IV), $\alpha 3\alpha 4\alpha 5$ (IV) or $(\alpha 5)_2\alpha 6$ (IV) protomers that assemble into a felt-like network, see Figure 3B^{31,42,45,49,51–53}. $(\alpha 1)_2\alpha 2$ (IV) is ubiquitous in BMs throughout the body and the nephron, see Figure 3C. The Bowman's capsule additionally contains the $(\alpha 5)_2\alpha 6$ (IV) molecule. Interestingly, during GBM development $(\alpha 1)_2\alpha 2$ (IV) is gradually replaced by $\alpha 3\alpha 4\alpha 5$ (IV) which is solely synthesized by podocytes^{31,45,47,49}. $\alpha 3\alpha 4\alpha 5$ (IV) contains more cysteine than $(\alpha 1)_2\alpha 2$ (IV) and is therefore more densely cross-linked. It is consequently more resistant to proteolytic attack and has a superior stability. Mutations in *COL4A3*, *COL4A4* or *COL4A5* lead to the development of Alport syndrome. Since proteinuria develops only gradually in Alport patients, $\alpha 3\alpha 4\alpha 5$ (IV) is not essential for the glomerular filtration itself but rather reduces the susceptibility of the GBM to damage^{50,54,55}.

Collagen I is a fibrillar collagen. It is the most abundant ECM protein in mammals and is responsible for maintaining the structural integrity of the tissue. Comparable to its relative collagen IV, it is composed of three α chains, twisted into a triple helix. In contrast to collagen IV, collagen I forms a long fibril instead of a network and is not part of the basement membranes but of the interstitial matrix^{56,57}.

Nidogen is a ubiquitous basement membrane glycoprotein. It is present in all BMs of the kidney, as depicted in Figure 3C. It serves as an important linker between the laminin and collagen networks in the BM^{58,59}.

Heparan sulphate proteoglycans (HSPGs) are large polyanionic molecules consisting of a core protein coupled with long heparan sulfate side chains. Heparan sulfate (HS) is a glycosaminoglycan (GAG) of repeating, enzymatically modified glucuronic acid and N-acetylglucosamine units^{60–62}. HSPGs link the BM components, as depicted in Figure 3B, and bind the growth factors basic fibroblast growth factor (bFGF), vascular endothelial growth factor (VEGF), platelet-derived growth factor (PDGF) to the ECM. The HSPG **Perlecan** is part of all BMs of the kidney, except of the GBM where **Agrin** is the dominant HSPG, as shown in Figure 3C³¹. A deletion of either of these genes is lethal for the embryo^{60,63,64}.

In conclusion, for the generation of an *in vitro* kidney model it has to be taken into consideration that the function of the kidney goes hand in hand with the correct composition of the ECM. The segment-specific ECM composition provides specific microenvironments to every renal cell type and should be emulated in a functional *in vitro* kidney model.

1.2.2.2 Mechanical forces direct cell behavior

Cells are highly sensitive to the mechanical properties of the surrounding ECM and to mechanical stimuli, such as shear stress or tensile and compressive forces, from their neighboring cells. Mechanical stimuli influence cell proliferation, apoptosis, differentiation and migration^{26,65,66}.

Cells sense their mechanical environment through their primary cilium, mechanosensitive ion channels, cell-cell and cell-ECM connections, as shown in Figure 4A.

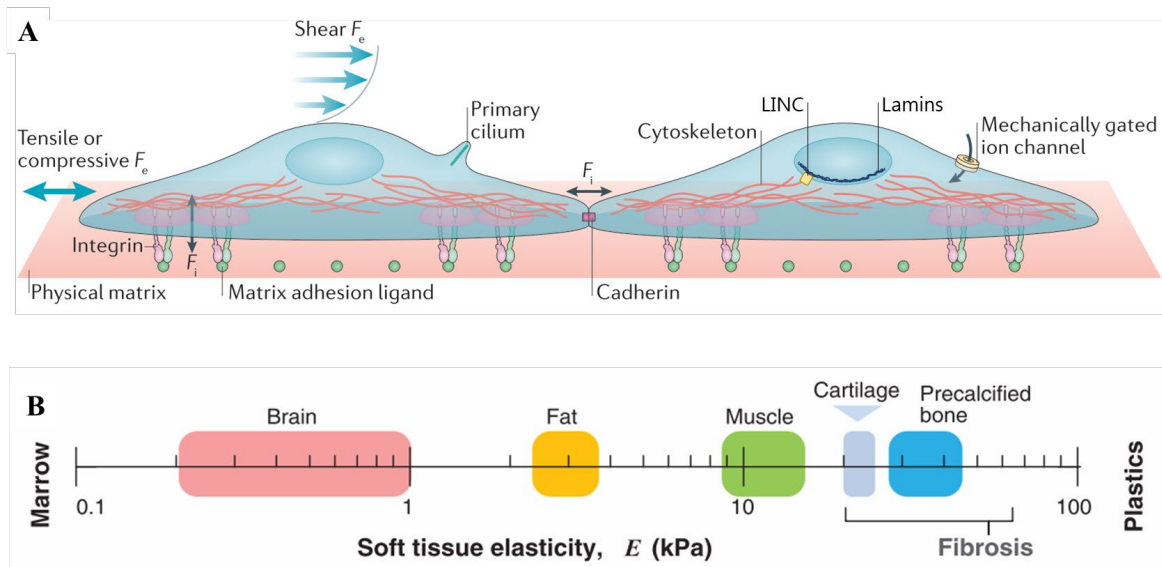


Figure 4: The effect of extracellular matrix properties on the cell (A) Cells sense extrinsic forces, F_e , such as shear and tensile or compressive forces, through their primary cilium, mechanically gated ion channels, through integrin-mediated cell-ECM adhesion and cadherin-mediated cell-cell adhesion. The cell generates intrinsic forces, F_i , and transfers these onto the ECM or neighboring cells. The cells translate these mechanical forces into biochemical signals, using multiple signaling pathways, or transmit the force via actin filaments and the LINC complex onto lamins in the nucleus, or react to nucleus deformations directly with changes in gene expression and in cell behavior and function. Adapted from Vining & Mooney⁶⁶. (B) Tissues exhibit a range of stiffness, quantified by the elastic modulus (E modulus). The E modulus of kidney tissue compares to fat tissue. Reproduced from Discher et al.⁶⁷.

The primary cilium is a microtubule based, slender cell protuberance present on most cells of the human body. In the kidney, the primary cilium is the mechanosensing receptor for fluid flow in the tubules. The flow exerts shear stress onto the cells that is crucial for a physiological cell morphology and function. Defects in this mechanosensing mechanism lead to the development of polycystic kidney disease. The replication of fluid flow in the *in vitro* model is therefore critical to achieve a native cell phenotype and to model diseases⁶⁸⁻

70.

Cells also sense the mechanics of the ECM they attached to. They connect to the ECM via integrins. Integrins are ECM binding receptors that are organized in clusters, called focal adhesions. They link the ECM to the actin filaments of the cytoskeleton via a set of linker proteins^{71,72}. Through this connection the cells probe the stiffness of the ECM. To this end, they apply a force onto the ECM by pulling with myosin II mini-filaments on the actin filaments that transfer the force to the integrins and then onto the ECM. A stiff ECM will resist that force and the integrins will not move. However, a soft ECM will deform, the bound integrins move and reduce the loading rate on the cytoskeletal force-bearing elements^{32,73-75}.

Upon that stimulus the integrins activate a number of signaling molecules intracellularly that initiate multiple mechanosensitive signaling pathways and result in activation of transcription factors and changes in gene expression^{32,66,76}.

Another major pathway of mechanotransduction is the direct physical linkage of the ECM to the deoxyribonucleic acid (DNA) via the cytoskeleton. Cytoskeletal fibers transmit the force via the LINC complex through the nuclear membrane onto the intermediate filaments of the nucleus, the lamins. Lamins bind directly to DNA and transcription factors, completing thus the force transmission⁷⁷⁻⁷⁹.

Moreover, the nucleus itself also acts as a mechanosensor. Nucleus deformation, for example in stretched cells on convex surfaces⁸⁰ or stiff substrates⁸¹, increases the lamin expression and regulates ECM directed differentiation.

The mechanical properties of a tissue, ECM or cell culture scaffold are described by various terms. Materials can behave in a plastic, elastic or viscous manner or a combination of these. ECM is a viscoelastic material. For materials with elastic properties the elastic modulus (E modulus) measures the resistance to being elastically deformed when a stress is applied. It is defined as the ratio of stress and strain. Stress is given as force per area. Strain is a normalized measure of deformation after a stress was applied. The stiffer a material, the higher is the elastic modulus. Soft tissues like brain, kidney, lung and muscle have an E modulus of up to 15 kPa. The higher the content of fibrillar collagen in a tissue, the stiffer it becomes. For example, fibrotic tissues, cartilage or precalcified bone have an E modulus of around 20-70 kPa. Calcified cortical bone reaches an E modulus of 14 GPa (Figure 4B)^{82,83}. In standard 2D cell culture, cells are grown on tissue culture plastic made from polystyrene which has an E modulus of around 3 GPa. In contrast, the human kidney has an E modulus

of around 2,5 kPa, approximately 6 orders of magnitude lower than plastic^{82,83}. Considering the impact of mechanical forces on cell behavior, it is not surprising that cells originating from the kidney, cultured on tissue culture plastic, show a different or even artificial behavior than *in vivo*.

In conclusion, an accurate, functional kidney model has to mimic the natural mechanical properties of the kidney and cannot rely on 2D cell culture on tissue culture plastic without flow.

1.2.3 Renal organogenesis

The mammalian kidney arises from the mesoderm. After neurulation, the trunk mesoderm is subdivided into chorda-mesoderm, paraxial mesoderm, intermediate mesoderm, and lateral plate mesoderm. The intermediate mesoderm (IM) develops into the urogenital system, including the kidneys and the gonads⁸⁴.

The anterior IM develops into the nephric duct (ND). Starting at the level of the sixth somite it elongates caudally and undergoes mesenchymal to epithelial transition (MET). The ND then buds and forms the ureteric bud (UB), initiating thereby the formation of the metanephros. Meanwhile the posterior IM differentiates into the metanephric mesenchyme (MM) that condenses around the branching UB tips into the SIX homeobox 2 (SIX2) positive cap mesenchyme (CM). UB and CM are in a reciprocal signaling relationship that causes further branching of the UB, and self-renewal and differentiation in the CM. After multiple rounds of branching, elongation and differentiation, the UB triggers the CM into MET. The CM develops into the renal vesicle (RV), a simple epithelial structure with a lumen, and after further elongation and segmentation into the S-shaped body (SSB). Finally, endothelial cells invade the proximal end of the SSB, and podocytes develop, thereby forming the mature nephron. The UB develops into the collecting ducts of the mature kidney (Figure 5)^{85–89}.

For the generation of an *in vitro* kidney model, the renal progenitor cells from MM and UB could be the ideal starting cell population, as these two cell types will give rise to all renal cell types in a self-organized differentiation process.

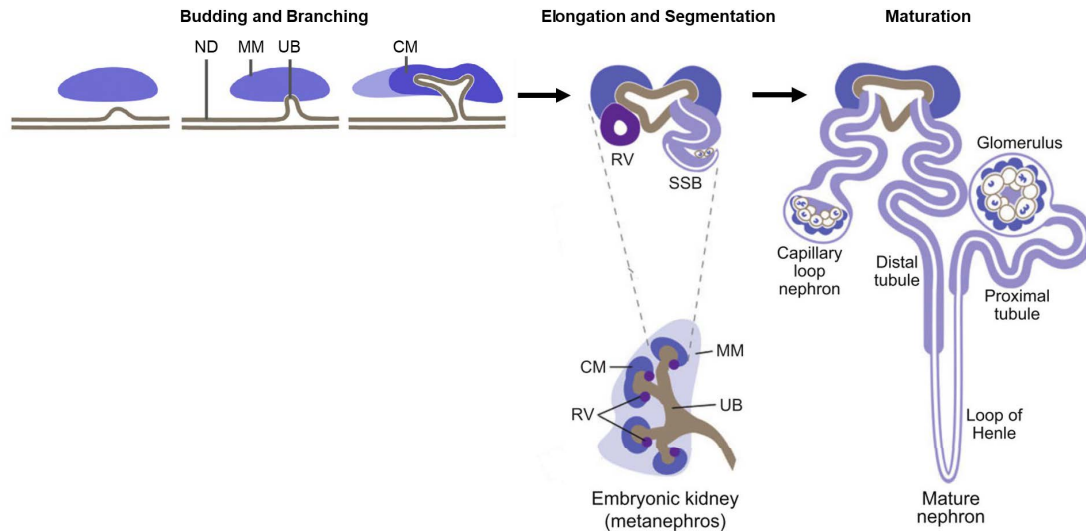


Figure 5: Development of the mammalian kidney. The ND buds into the UB, triggering the condensation of the MM into CM. Reciprocal signaling between CM and UB induces branching in the UB and the formation of epithelial RV in the CM. The RV elongates and differentiates via the SSB state into the mature nephron. The UB develops into the collecting ducts. ND, nephric duct; MM, metanephric mesenchyme; UB, ureteric bud; CM, cap mesenchyme; RV, renal vesicle; SSB, S-shaped body. Adapted from Takasato and Little^{88,89}

1.3 Tissue engineering of the kidney

Tissue engineering is a multidisciplinary approach to generate functional tissue *in vitro*. Tissue engineering requires the arrangement of the tissue-specific cell types into the tissue-specific architecture. To achieve this goal, scaffolds or self-organizational strategies are usually applied^{90,91}.

To date, engineered tissues are already being applied as 3D *in vitro* models in drug development, disease modeling or in the investigation of cell-matrix interactions. Simple tissues, for example a tissue engineered bladder, have even reached clinical application⁹². Considering the ongoing progress in tissue engineering, it will most likely be possible to produce fully functional complex organs for transplantation in the future.

The kidney's elaborate architecture and exceptionally diverse functions makes tissue engineering of the kidney an extremely complex task.

As highlighted in the previous chapters, three criteria have to be met to engineer a functional *in vitro* kidney model. Firstly, an appropriate cell source has to be identified that gives rise to all renal cell types. Secondly, the nephron architecture, as well as the composition and

mechanical properties of the ECM have to be replicated to ensure proper cell function and phenotype. And thirdly, the *in vitro* model has to be perfusable to enable glomerular filtration, to apply shear stress and to supply nutrients.

1.3.1 Cell source

The kidney comprises more than 20 different kidney cell types¹⁰. One way to obtain all these cell types would be to isolate primary adult human kidney cells. However, human kidneys are a rare resource and urgently needed for transplantation. Moreover, primary adult kidney cells have naturally a high donor-to-donor variability, a limited proliferative capacity and they dedifferentiate upon prolonged cultivation, which makes it impossible to generate the cell numbers needed for kidney tissue engineering^{70,93,94}.

Cell lines have a stable phenotype, are proliferative and easily available. Hence, the majority of current kidney models are based on renal cell lines. Cell lines such as the MDCK cells have been used for decades but are of non-human origin. The human immortalized renal epithelial line HK2 line has also been excessively tested. However, it was found that HK2 cells only show limited proximal tubular functions and markers and that their response to nephrotoxins differs from *in vivo* data. First studies of newer immortalized human renal epithelial lines, such as NKi-2 or RPTEC/TERT1, hint towards a better-preserved functionality. Nevertheless, an immortalized cell line does not exist for every renal cell type^{8,70}.

Human induced pluripotent stem cells (hiPSCs) are a novel source of human somatic cells for disease modeling and drug screenings, see Figure 6⁹⁵. hiPSCs were discovered in 2006 by the Japanese Nobel prize winner Shinya Yamanaka. hiPSCs are reprogrammed from human adult fibroblasts that were transduced with the reprogramming factors OCT3/4, SOX2, KLF4, and c-MYC. hiPSCs can differentiate into all three germ layers and generally behave similar to embryonic stem cells (ESCs)^{96,97}. ESCs are harvested from the inner cell mass of the blastocyst. The developing embryo is destroyed in this process resulting in the ethical dilemma surrounding the use of ESCs⁹⁸. hiPSCs are not afflicted with these concerns. The reprogramming technique enables the generation of patient-specific hiPSCs and opens

the door for autologous tissue engineering or cell therapies⁹⁹. For example, hiPSC lines from PKD patients or genetically engineered lines carrying the same mutations show the cystic disease phenotype in an organoid culture¹⁰⁰.

The differentiation of hiPSCs is classically directed by the variation of their chemical environment. Signaling processes during embryogenesis *in vivo* are recapitulated *in vitro* by the addition of growth factors and small molecules to a diverse range of cell culture media and by coating tissue culture plastic plates with a thin layer of ECM molecules. However, for many cell types current hiPSC differentiation protocols lead to immature or fetal phenotypes in standard *in vitro* culture systems¹⁰¹. To generate more mature phenotypes *in vitro*, the research field currently focuses on improving the mechanical cell environment^{67,102}. Providing natural shear stress, geometry and stiffness improved many differentiations, such as hepatocyte¹⁰³ and cardiomyocyte¹⁰⁴ differentiations. Huge improvements in self-organization and maturation were already achieved, when cells were cultured in hydrogels¹⁰⁵, decellularized scaffolds¹⁰⁶ or in organoids¹⁰⁷.

In the last years impressive progress was made in the differentiation of hiPSCs into the renal lineage. Multiple protocols for the differentiation into renal progenitor cells (RPCs) were published. These protocols mimic the signaling during renal organogenesis, as described in 1.2.3. MM or UB cells are derived via mesoderm induction. These RPCs have the potential to differentiate into all renal tubular epithelial cells, podocytes and also mesenchymal cells and to self-organize into nephron-like structures when they are cultured in 3D and were therefore chosen as the cell source for the tissue engineering approach in this thesis¹⁰⁸.

Moreover, endothelial cells (ECs) can be differentiated from hiPSCs through mesoderm induction, followed by an endothelial specification step. These cells will be used to engineer the vascular compartment of the kidney model¹⁰⁹.

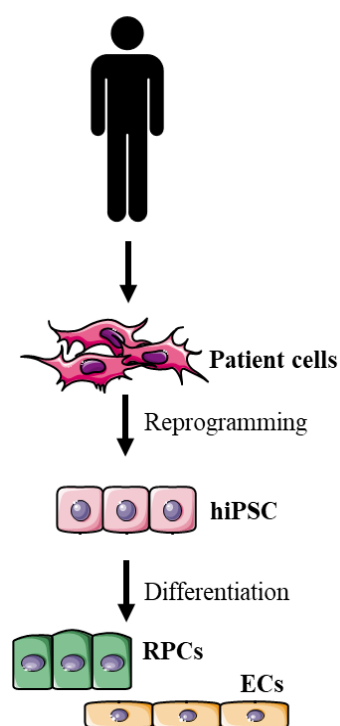


Figure 6: Human induced pluripotent stem cells (hiPSCs) are reprogrammed from human somatic cells. hiPSCs can serve as a cell source for kidney tissue engineering, as they can proliferate and differentiate into renal progenitor cells (RPCs) and endothelial cells (ECs).

1.3.2 Architecture and perfusion

2D cultures of human cell lines on tissue culture plastic are classically applied as *in vitro* kidney models. These models are simple, cost-effective, well-established and high-throughput and therefore ideally suited for large-scale compound screens. However, the application of these models did not result in the improvement of kidney failure treatments and too often do not detect drug-induced nephrotoxicity in preclinical studies, as already mentioned before. This poor predictivity is caused by the lack of physiological relevance of these simple 2D models^{8,70}.

Microfluidic models improve the physiological relevance by including shear stress. In microfluidic models the cells are cultured in confluent monolayers within perfused channels on microfluidic chips. Shear stress increases the expression of functional relevant transporters and ion channels in proximal tubular cells and provokes the formation of primary cilia and microvilli. Hence, the phenotype of the cultured proximal tubular cells improves and consequently it was found that the responses of these cells to nephrotoxins like cisplatin are closer to *in vivo* responses than from cells in static 2D kidney models. The microfluidic chip design facilitates parallelized, high-throughput screenings of drug candidates. However, these models are essentially still 2D systems. Moreover, they mostly incorporate only one cell type in an artificial architecture on plastic or silicone of artificial stiffness^{8,70,110,111}.

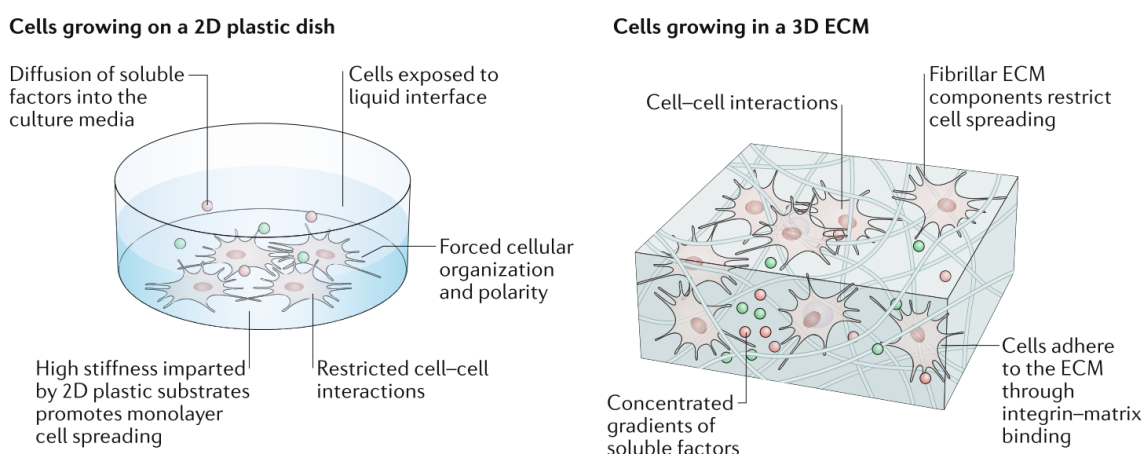


Figure 7: Differences between 2D and 3D *in vitro* tissue models. 3D cell culture provides *in vivo* like conditions to the cultured cells, whereas cells cultured in 2D are exposed to artificial conditions. Figure reproduced from Hussey et al.²⁷.

Tissue engineered 3D *in vitro* models have already been proven to be more accurate than 2D *in vitro* models¹¹². The dilemma of 2D cell culture is the lack of ECM and thus the lack of 3D cell-ECM and cell-cell interactions and the artificial stiffness of the culture surfaces, see Figure 7. Cells grown in 2D are therefore hindered in developing a native cell morphology and function. Cells grown in 3D conditions, however, are able to establish cytokine gradients and to self-organize into tissue-like structures, called organoids^{27,66}.

When hiPSC-derived renal progenitor cells are brought into a 3D environment, they replicate the renal organogenesis. They self-organize into S-shaped bodies that mature further into nephrons. These kidney organoids are therefore a very promising approach to build a functional kidney model. They incorporate a big spectrum of renal cells that produce their own ECM in a nephronal architecture^{85,113–117}. At present however, only 50% of the cells inside these organoids are tubule cells or podocytes and the organoids lack the high ordered organization of kidneys. The nephrons are randomly scattered throughout the organoid and neither an organized connection of the nephrons to a collecting duct system nor an organized vascular network is present. Therefore, no perfusion is possible. Hence, cells lack the exposure to shear stress and single cell analysis revealed consequently already that none of the kidney cell types inside the organoids are fully mature¹⁰⁸. Moreover, without vascularization the center of the organoid is poorly supplied with nutrients and oxygen. And most importantly, the organoid model cannot emulate the perfusion-based function of the kidney.

The complex anatomy of the kidney is hard to recreate. Therefore, a rational starting point for kidney tissue engineering is to provide a scaffold to the cells that already defines the architecture. To date, there is no technology that can copy that delicate structure. The resolution of 3D printing, for example, is not high enough. Only isolated parts of the nephron have been reproduced with 3D printing as yet¹¹⁸.

Kidney ECM based scaffolds would not only provide the correct architecture but due to the natural stiffness and segment-specific composition also the specific microenvironments to every renal cell type. These microenvironments could provide important differentiation and maturation signals to RPCs. Furthermore, it is of great advantage that kidney ECM based

scaffolds preserve the native vascular network. It is therefore possible to perfuse the kidney models that were created with these scaffolds.

Importantly, ECM proteins are highly conserved among different taxa. All bilaterians share the proteins that make up the core of the basement membrane^{26,119,120}. Moreover, all mammalian kidneys have the same basic nephron structure. At the macroscopic level the kidney architecture varies, as shown in Table 1, but these differences do not impact the functionality^{121,122}. It is therefore possible to generate ECM scaffolds from rats or pigs and to repopulate them with human cells.

Table 1: Species differences in renal structure¹²¹

Parameter	Rat	Pig	Human
Renal organization	Unilobular	Multilobular	Multilobular
Single kidney weight [g]	0,75	77	157
Number of nephrons	$3 \cdot 10^4$	$1 \cdot 10^6$	$1 \cdot 10^6$
Glomerular radius [μm]	61	83	100
Tubule radius [μm]	29	n/a	36
Proximal tubule length [mm]	12	n/a	16

In 2013, a promising proof of concept study was published by Song et al.¹²³. They reported the generation of a whole organ *in vitro* kidney model that produced rudimentary urine, by decellularization of a rat kidney and recellularization of that scaffold with primary rat neonatal kidney cells and human endothelial cells. The same approach could be upscaled to produce kidneys for transplantation, when using a porcine kidney as a scaffold. Based on this study the approach of whole organ kidney tissue engineering with decellularized whole rat kidneys and hiPSC-derived RPCs was chosen in this thesis. Whether the decellularized kidney scaffold promotes full, site-specific maturation of the reseeded RPCs needs to be investigated.

1.3.3 De- and recellularization

Decellularization is the process of removing all cells from a cell culture, tissue or whole organ, while retaining the extracellular matrix. Decellularized ECM is a suitable biological scaffold for numerous tissue engineering approaches¹²⁴.

Decellularized porcine small intestinal submucosa and urinary bladder matrix are acellular biologic surgical meshes that have been used in millions of patients without evidence of

adverse immunological reactions against these xenogenic biomaterials²⁷. Building on this work, the decellularization of whole organs was developed in 2008 when Harald Ott first decellularized whole porcine hearts¹²⁵. Whole organ decellularization requires the perfusion of decellularization agents through the native vasculature. The scaffold retains the organ's complex geometry and can be reseeded with patient-derived cells for whole organ tissue engineering⁹³.

Decellularization is achieved by initial lysis of cell membranes, followed by the removal of all cellular debris. A combination of physical, chemical and enzymatic treatments is necessary to achieve full decellularization. To provoke the rupture of the cell membrane, sonication or freeze–thaw cycles are usually applied. Another common cell lysis treatment is osmotic shock with hypotonic or hypertonic solutions. After cell lysis, it is necessary to solubilize the cell membranes and to remove cytoplasmic components. Detergents are chemical surfactants that are usually applied in this second phase of decellularization^{126,127}. These amphiphilic substances comprise a lipophilic hydrocarbon tail and a hydrophilic polar head group. They are therefore able to form micelles and to dissolve lipids in aqueous solutions. The hydrophilic-lipophilic balance (HLB) of a detergent is a measure for the balance of size and strength of the opposing hydrophilic and hydrophobic groups. Increasing HLB values correspond to an increasing hydrophilic character. Ionic detergents, such as sodium deoxycholate (SDC) and sodium dodecyl sulfate (SDS), are harsher and have a higher HLB than zwitterionic detergents, such as CHAPS, or non-ionic detergents, such as Triton X-100 (TX-100). The HLB of SDS, SDC and TX-100 are 40, 16 and 13, respectively^{128,129}. Chemicals less commonly applied for decellularization are alkaline or acidic substances, e.g. peracetic acid (PAA), and chelating agents, e.g. ethylenediaminetetraacetic acid (EDTA) and egtazic acid (EGTA). Enzymatic treatment with proteases, such as trypsin, are normally avoided since they decrease the mechanical strength of the tissue and randomly digest ECM proteins. Nucleases, particularly DNase, facilitate nucleic acid removal^{126,127}. α -galactosidase

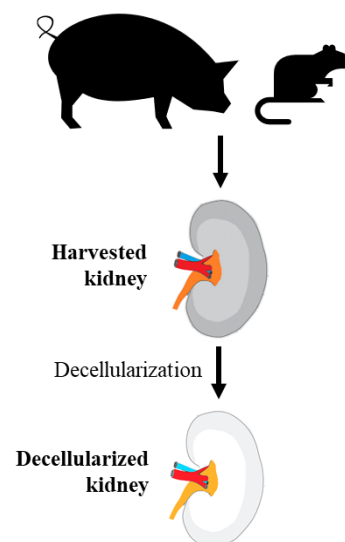


Figure 8: Decellularization of whole rat or pig kidneys removes the cells and retains the extracellular matrix of the organ. The decellularized kidney serves as a scaffold for 3D kidney tissue engineering.

removes the Gal epitope that is known to cause xenorejection in humans¹³⁰. The sequence, duration and temperature in which these steps are performed are essential for the outcome. Agitation or perfusion facilitates the transport of decellularization agents through the tissue or whole organ to the cells and the removal of cellular debris. Agitation is sufficient for decellularization of cell culture monolayers or simple, thin tissues. For whole organ decellularization, however, perfusion through the vascular network is necessary and extremely effective^{93,131}. An effective decellularization is important for later reseeding with cells or transplantation into patients since cellular antigens and nucleic acids are targets for immune cells^{126,132,133}.

The native composition, ultrastructure, and macroscopic 3D architecture of organ-derived ECM scaffolds provide the necessary microenvironment to support attachment, proliferation, and differentiation of reseeded cells, as discussed before. However, every decellularization technique invariably disrupts the ECM to some degree. One goal of this thesis was therefore to identify a decellularization protocol that maximizes cell removal and minimizes ECM loss and damage^{93,131}. It was hypothesized that the damage to the ECM could be reduced by applying a milder detergent than SDS and by decreasing the temperature from the usually applied room temperature to 4°C.

Recellularization is the process of seeding cells into a previously decellularized organ or tissue. If the aim is to restore the functionality of the decellularized organ, the success of a recellularization can be measured by the same criteria as the regeneration after organ damage: Firstly, the cell number must be close to the number present prior to

decellularization¹³⁴. A pig kidney comprises approximately $7,7 \cdot 10^{10}$ cells. A single rat kidney comprises approximately $7,5 \cdot 10^8$ cells^{121,135}. Hence, the cells applied for kidney tissue engineering must have an extensive proliferative capacity. Cells must proliferate either after seeding inside the scaffold or in a mass expansion process before seeding.

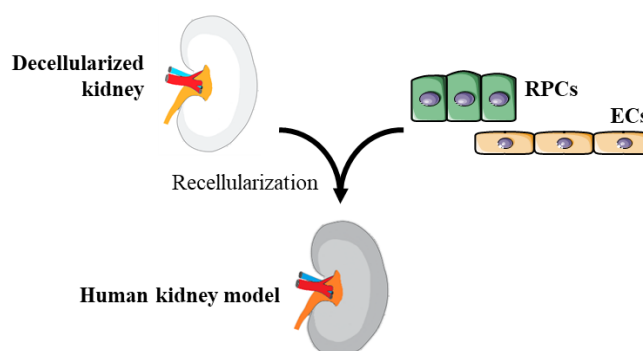


Figure 9: Recellularization. Decellularized rat kidneys will be recellularized with hiPSC-derived renal progenitor cells and endothelial cells to generate a tissue engineered 3D kidney model.

Secondly, to achieve functionality, the reseeded cells must be positioned in the exact compartment as they existed prior to decellularization¹³⁴. Reseeding can be performed by perfusing cells into the kidney through three different seeding ports. The artery and the vein grant access to the vascular compartment, the ureter to the tubular compartment. Injection with a canula into the parenchyma is a fourth option¹³⁶. Whether the seeded RPCs migrate inside the scaffold and thereby repopulate every compartment or whether the seeding strategy has to push the cells into every niche, has to be investigated.

Cell engraftment, proliferation, maturation and application of the model in, for example, nephrotoxicity studies may necessitate a culturing time spanning many weeks. During this period the seeded cells require the supply of nutrients and oxygen for cell survival and function. Recellularization is therefore performed in a perfusion bioreactor^{93,136,137}

2 Aim

The aim of this thesis was to establish a whole organ model of the human kidney on the basis of hiPSC-derived renal progenitor cells and decellularized rat kidney scaffolds.

To achieve this goal, the minor aims were:

- i. To develop a perfusion bioreactor system including a control software and automated pressure and pH control to allow whole organ de- and recellularization.
- ii. To optimize a decellularization protocol for kidneys that maximizes cell removal and minimizes ECM loss and damage.
- iii. To reendothelialize the vascular compartment of the decellularized kidney with hiPSC-derived endothelial cells.
- iv. To recellularize the whole rat kidney scaffold with hiPSC-derived renal progenitor cells, to test the hypothesis that the decellularized kidney matrix promotes their site-specific differentiation and maturation by preserved architectural, mechanical and biochemical features.
- v. To determine which of these mechanical and biochemical features influence the maturation of hiPSC-derived renal progenitor cells.

3 Materials and Methods

3.1 Materials

3.1.1 Cells

Table 2: Cells

Name	Source/Manufacturer
<i>hiPSC lines</i>	
BCRTi005-A	Urinary cells, reprogrammed with sendai virus and OCT4, SOX2, KLF4, cMYC Rossbach et al. ¹³⁸
BIHi004-A	Skin fibroblasts, episomal reprogramming with OCT4, SOX2, KLF4, LIN28, L-MYC Hossini et al. ¹³⁹
WISCi004-B (GFP+)	Fetal lung fibroblasts, lentiviral reprogramming with OCT4, SOX2, NANOG, LIN28 Yu et al. ¹⁴⁰
<i>Primary cells</i>	
HUVEC	Pellobiotech

3.1.2 Reagents

Table 3: Reagents

Name	Manufacturer
<i>Buffers</i>	
DPBS	Thermo Fisher Scientific
DPBS, calcium, magnesium	Thermo Fisher Scientific
TRIS-base	Sigma-Aldrich
<i>Cell culture media</i>	
Advanced RPMI 1640	Thermo Fisher Scientific
DMEM w/o phenol red	Biochrom
DMEM/F-12	Thermo Fisher Scientific
EGM-2	Lonza
Essential 8 Medium	Thermo Fisher Scientific
Knockout DMEM	Thermo Fisher Scientific
Neurobasal medium	Thermo Fisher Scientific
PFHMII	Thermo Fisher Scientific
REGM	Lonza
STEMdiff APEL 2	StemCell Technologies
StemPro-34 SFM	Thermo Fisher Scientific
<i>Cell culture media supplements</i>	
Activin A, recombinant human	Peprotech
Amphotericin B, 100x	Biochrom
Antibiotic-Antimycotic, 100x	Thermo Fisher Scientific
B-27 supplement without Vitamin A, 50x	Thermo Fisher Scientific
bFGF, recombinant human	Peprotech
BMP4, recombinant human	Peprotech

Name	Manufacturer
CHIR99021	StemCell Technologies
FCS Superior	Biochrom
Forskolin	Abcam
GDNF, recombinant human	Peprotech
GlutaMAX	Thermo Fisher Scientific
N-2 supplement, 100x	Thermo Fisher Scientific
PenStrep, 100x	Biochrom
Retinoic acid	Stemgent
ROCK inhibitor Y26732	WAKO Chemicals
SB431542	Sigma-Aldrich
VEGF 165, recombinant human	Peprotech
<i>Cell culture surface coatings</i>	
Collagen IV (Col (α 1)2 α 2 (IV)), human placenta	Sigma-Aldrich
Fibronectin, human plasma	Corning
Geltrex LDEV-free hESC-qualified	Thermo Fisher Scientific
Laminin 511, recombinant human	BioLamina
Laminin 521, recombinant human	BioLamina
Ultrapure water with 0,1% gelatin	Millipore
<i>Chemicals</i>	
Citrate	Sigma-Aldrich
Cysteine-HCl	Sigma-Aldrich
DMSO	Sigma-Aldrich
Dopamine	Sigma-Aldrich
EDTA, 0,5 M	Thermo Fisher Scientific
HCl, 6 M	Carl Roth
Heparin, 5000 U/ml	Biochrom
NaCl	Sigma-Aldrich
NaOH, 1 M	Carl Roth
Trypan Blue stain, 0,4%	Thermo Fisher Scientific
Roti-Phenol/Chloroform/Isoamyl alcohol, 25:24:1	Carl Roth
Roti-Chloroform/Isoamyl alcohol, 24:1	Carl Roth
Resazurin	Sigma-Aldrich
SDC	Sigma-Aldrich
SDS	Sigma-Aldrich
Sodium acetate	Sigma-Aldrich
TritonX-100	Sigma-Aldrich
<i>Enzymes</i>	
DNase I	Roche
Papain	Sigma-Aldrich
Proteinase K	Sigma-Aldrich
StemPro Accutase cell dissociation reagent	Thermo Fisher Scientific
Trypsin, 0,25%	Thermo Fisher Scientific
Trypsin/EDTA, 0,05 %/0,02 %	Biochrom
<i>Histology/Immunofluorescent staining</i>	
Albu Max II lipid rich bovine serum albumin	Thermo Fisher Scientific
Bovine albumin fraction V, 7,5% solution	Thermo Fisher Scientific
Cytofix	BD
Donkey serum	Merck Millipore
Eosin Y	Carl Roth
Ethanol, \geq 99,8%	Carl Roth
FcR blocking reagent, human	Miltenyi
Formaldehyde buffered solution, 4%, pH 7,5	Herbeta
Immunoselect mounting medium DAPI	Dianova
Mayer's acid hemalum	Carl Roth
Permeabilizing Solution 2	BD
Roti-Histokitt	Carl Roth

Name	Manufacturer
Surgipath paraplast plus	Leica
Xylol	Carl Roth

3.1.3 Consumables

Table 4: Consumables

Name	Manufacturer
Cell culture	
Serological pipette, 5 ml, 10 ml, 25 ml, 50 ml	Corning
Medium bottle, 100 ml, PET, sterile	Greiner Bio-One
MS MACS columns	Miltenyi
Falcon tissue culture treated flasks, vented ,75 cm ² , 175 cm ²	Corning
Falcon tissue culture treated microplates, 6-, 12-, 24-, 96-wells	Corning
Falcon tubes, 15 ml, 50 ml	Corning
Cell scraper, 25 cm	Sarstedt
Cell strainer, 40 µm	Corning
Countess cell counting chamber slides	Thermo Fisher Scientific
CryoTubes, 1,8 ml	Nunc
General consumables	
Biopsy punch, 4 mm	Pfm medical
Cannula, 27 G	BD
Combitips advanced, 0,1 ml, 0,5 ml, 2,5 ml, 5 ml, 10 ml, 25 ml	Eppendorf
Eppendorf tubes, 0,5 ml, 1,5 ml, 2 ml	Eppendorf
Falcon FACS tubes, 5 ml	Corning
MACSQuant washing solution	Miltenyi
PCR plate, 384-well, MicroAmp EnduraPlate optical	Thermo Fisher Scientific
PCR strips, 0,2 ml	Biozym
Pipette tips, 10 µl	Eppendorf
Pipette tips, 1000 µl	Greiner Bio-One
Pipette tips, 200 µl	Sarstedt
Pipette tips, SafeSeal professional, 10 µl, 20 µl, 200 µl, 1000 µl	Biozym
Syringe, 1 ml	B. Braun Medical AG
Syringe, 3 ml, Luer-Lock	BD
Syringe, 50 ml, Luer-Lock	BD
Syringe, GASTIGHT, #1710, 100 µl	Hamilton
Histology	
Cassettes, Q Path MacroStar II	VWR
Microscope slide, 75x25 mm, SuperFrost Plus	Langenbrinck
Glass cover slip, 24x60 mm	Langenbrinck
ImmEdge hydrophobic barrier PAP pen	Vector Laboratories
Perfusion bioreactor	
3-way stopcock	Smiths medical
Bubble stones, AS30	Tetra
Combifix adapter, Luer female/female	B. Braun Medical AG
Combifix adapter, Luer male/male	B. Braun Medical AG
DURAN GL 45 blue PP screw cap with 3x GL 14 ports	SCHOTT DURAN
DURAN Hose connection screw cap blue PP, GL 14	SCHOTT DURAN
DURAN Insert for hose connection screw cap, GL 14, 3,2mm	SCHOTT DURAN
DURAN Laboratory bottle, GL 45, 1000 ml	SCHOTT DURAN
DURAN Laboratory bottle, GL 45, 2000 ml	SCHOTT DURAN
DURAN Laboratory bottle, GL 45, 50 ml	SCHOTT DURAN
DURAN Laboratory bottle, GL 45, 500 ml	SCHOTT DURAN

Name	Manufacturer
DURAN Neck thread GL 14, red PBT cap with lip seal	SCHOTT DURAN
DURAN pressure equalization set, GL14, 0,2 µm membrane filter	SCHOTT DURAN
Female Luer-Lock to barb connector, 1/16"	Quosina
Female Luer-Lock to barb connector, 1/8"	Quosina
Female Luer-Lock to barb connector, 5/32"	Quosina
Gas tubing, TUS, softpolyurethane	SMC
Luer stopper	Fresenius Kabi
Male Luer-Lock to barb connector, 1/16"	Quosina
Male Luer-Lock to barb connector, 1/8"	Quosina
Perfusor Line, 150 cm, 1,0x2,0 mm, PE	B. Braun Medical AG
Perfusor Line, 150 cm, 1,5x2,7 mm, PVC	B. Braun Medical AG
Perfusor Line, 50 cm, 1,5x2,7 mm, PVC	B. Braun Medical AG
pH sensor flow through cell	Presens
Plastic ring, M3	Suki
pO ₂ sensor flow through cell	Presens
Pressure sensor dome	Memscap
Pump tubing, PharMed BPT, ID 0,89 mm	IDEX Health&Science
Pump tubing, PharMed, ID 3,2 mm, WS 1,6 mm	IDEX Health&Science
Rotilabo syringe filter, PTFE	Carl Roth
Surgery	
Scalpel, sterile, disposable, #11	Schreiber Instrumente
Wooden applicators with cotton head, 150x2,2 mm	Karl Hecht GmbH
Swabs, non-woven	Charité
Feeding needle, 24 G	Agntho's
Neoflon, 26 G	BD
Disposable cup, 100ml	Sarstedt
Silk, 7/0 USP, 100m	Resorba
Tissue culture dishes, 100 mm	VWR

3.1.4 Kits

Table 5: Kits

Name	Manufacturer
Blyscan GAG assay	Biocolor
CD144 MicroBead Kit, human	Miltenyi
ELISA Kit, hbFGF	R&D Systems
ELISA Kit, hVEGF	Ani Biotech Oy
RNeasy Plus Mini Kit	Qiagen
Sylgard 184 silicone elastomer kit	Dow Corning
Sylgard 527 A&B silicone dielectric gel	Dow Corning
TaqMan Fast Advanced Master Mix	Thermo Fisher Scientific
TaqMan Reverse Transcription Reagents	Thermo Fisher Scientific
Total Collagen Assay Kit	Quickzyme

3.1.5 Antibodies and fluorescent dyes

Table 6: Primary and secondary antibodies and nucleic acid dyes

Name	Clone	Species of origin	Manufacturer
Primary antibodies			
CD31	EPR3094	rabbit	Abcam
Collagen I	COL-1	mouse	Abcam
Collagen IV	polyclonal	rabbit	Abcam
Fibronectin	polyclonal	rabbit	Abcam
Laminin	polyclonal	rabbit	Abcam
LHX1	OTI2D5	mouse	Novus Biologicals
PAX2	polyclonal	rabbit	Thermo Fisher Scientific
Conjugated antibodies			
CD144-FITC	REA199	human	Miltenyi Biotec
CD31-APC	AC128	human	Miltenyi Biotec
mouse IgG-AlexaFluor 647	polyclonal	donkey	Thermo Fisher Scientific
rabbit IgG-AlexaFluor 647	polyclonal	donkey	Thermo Fisher Scientific
Nucleic acid dyes			
DAPI			Thermo Fisher Scientific
Live/Dead Blue			Thermo Fisher Scientific
PI			Sigma-Aldrich

3.1.6 qPCR gene expression assays

Table 7: TaqMan gene expression assays

Gene name	TaqMan Ref number	Manufacturer
<i>AQP1</i>	Hs01028916_m1	Thermo Fisher Scientific
<i>ATP1A1</i>	Hs00167556_m1	Thermo Fisher Scientific
<i>PODXL</i>	Hs01574644_m1	Thermo Fisher Scientific
<i>SIX2</i>	Hs00232731_m1	Thermo Fisher Scientific
<i>SLC12A2</i>	Hs00169032_m1	Thermo Fisher Scientific
<i>SLC12A3</i>	Hs01027568_m1	Thermo Fisher Scientific
<i>SYNPO</i>	Hs00702468_s1	Thermo Fisher Scientific
<i>WT1</i>	Hs01103751_m1	Thermo Fisher Scientific
<i>GAPDH</i>	Hs03929097_g1	Thermo Fisher Scientific
<i>RNA18S5</i>	Hs03928990_g1	Thermo Fisher Scientific

3.1.7 Instruments

Table 8: Instruments

Name	Manufacturer
Cell culture	
Aspiration system, VacuSafe and Vacuboy	IBS Integra Biosciences
CountessII automated cell counter	Thermo Fisher Scientific
Incubator, 11-13625	Binder
Incubator, Heracell 240i CO ₂	Thermo Fisher Scientific
Laminar flow hood, Herasafe KS9	Thermo Fisher Scientific
Laminar flow hood, L226 IVF	K-Systems

Name	Manufacturer
MiniMACS separator	Miltenyi
Mr. Frosty freezing container	Nalgene
Pipetboy	IBS Integra Biosciences
Vortex-2-Genie	Scientific Industries Inc.
Water bath, DC10	Thermo Fisher Scientific
<i>Centrifuges</i>	
Centrifuge, Allegra X22	Beckman Coulter
Centrifuge, Combi-Spin FVL-2400N	bioSan
Centrifuge, Heraeus Fresco	Thermo Fisher Scientific
Centrifuge, Heraeus Multifuge X3R	Thermo Fisher Scientific
Centrifuge, Micro	Carl Roth
<i>General</i>	
Heating and drying oven, FED 56	Binder
Heating and drying oven, VENTI-Line	VWR
Magnetic stirrer, D-6010	neoLab
Multipipette Xstream	Eppendorf
PCR FlexCycler	Analytik Jena
Pipette Research plus, 2,5 µl, 10 µl, 20 µl, 200 µl, 1000 µl	Eppendorf
Platform shaker, Titramax 1000	Heidolph
Roller mixer, SRT9D	Stuart
Thermomixer comfort	Eppendorf
Ultrasonic processor, UP100H	Hielscher Ultrasound Technology
Vacuum concentrator, 5301	Eppendorf
Vacuum desiccator, DURAN DN200	SCHOTT DURAN
Vacuum pump, DUO 2.5	Pfeiffer Vacuum
<i>Histology</i>	
Flattening table for clinical histopathology, HI1220	Leica
Heating and drying oven, Heraeus function line	Thermo Fisher Scientific
Heating plate	Rommelsbacher
Microtome blade, S35	Feather
Microtome, RM2255	Leica
Paraffin dispenser	MEDAX
Paraffin tissue floating bath	MEDAX
Pressure cooker, ASH22-4.5	Krüger
Tissue processor, TP1020	Leica
<i>Imaging and Quantification</i>	
ABL 700 series, blood gas analyzer	Radiometer Medical
AFM, MFP3D-Bio	Asylums Research
Bose Test Bench, LM 1 ElectroForce	Bose
Flow cytometer, LSR-II Fortessa	BD
Flow cytometer, MACS Quant VYB	Miltenyi
Microscope, Axiovert 40CFL	Zeiss
Microscope, Leica DMI8	Leica
NanoDrop 1000	NanoDrop Technologies
Operetta high content imaging system	Perkin Elmer
pH-meter, PB 11	Sartorius
Plate reader, Mithras LB 940	Berthold Detection Systems
Plate reader, SpectraMax 340PC-384	Molecular Devices
Precision balance	Sartorius
qPCR cycler, QuantStudio 6 Flex	Thermo Fisher Scientific
<i>Perfusion bioreactor</i>	
Amplifier for pressure sensor SP844	HJK Sensoren + Systeme
CompactDAQ chassis, NIcDAQ-9174	National Instruments
Gas blender, GB-103	MCQ
Incubator, ICP260, compressor-cooled	Memmert
Membrane oxygenating chamber	Radnoti

Name	Manufacturer
NI-9201, C Series voltage input module	National Instruments
NI-9217, C Series temperature input module	National Instruments
Peristaltic pump, IP65	Ismatec
pH sensor, pH-1 mini v2	Presens
pO ₂ sensor, Fibox 3	Presens
Pressure sensor, SP844	Memscap
Pump head, MS/CA 4-12	Ismatec
<i>Surgery</i>	
Forceps, Dumont #5	Fine Science Tools
Forceps, Dumont #7b	Fine Science Tools
Halogen cold light source, KL 1500 compact	Leica
Scissors, extra fine bonn, 13mm	Fine Science Tools
Scissors, student vannas spring, 5 mm	Fine Science Tools
Sealing machine, EM20	Enthral medical
Stereomicroscope, MZ75	Leica

3.1.8 Software and data bases

Table 9: Software and data bases

Name	Reference / Manufacturer
Columbus image analysis server	PerkinElmer
FCS Express 5 Plus	Denovo Software
FlowJow 8.8.2	TreeStar
GraphPad Prism 5.0	GraphPad Software, Inc.
Harmony high-content imaging and analysis software	Perkin Elmer
LabVIEW 2013	National Instruments
Leica Application Suite X	Leica
Mendeley Desktop 1.19.3	Mendeley
Microwin 2000	Associated with Mithras LB 940
MS Office 2010	Microsoft
NCBI	http://www.ncbi.nlm.nih.gov/
PubMed	http://www.ncbi.nlm.nih.gov/pubmed/
QCapture Pro 6.0	QImaging
Quant studio real-time PCR software	Thermo Fisher Scientific
SoftMax Pro 7.0	Molecular Devices

3.2 Methods

3.2.1 Cell culture

3.2.1.1 Standard work and culture conditions

Cell culture handling was performed at room temperature under sterile conditions in class II laminar flow hoods. Cells were cultured at 37 °C, 5% CO₂ and 95% air humidity.

3.2.1.2 Coating of cell culture surfaces

Cell culture surfaces were coated with various ECM molecules, depending on the application.

Geltrex stock vials were thawed at 4 °C overnight and diluted 1:10 in Knockout Dulbecco's Modified Eagle's Medium (DMEM), these working solutions were stored at -20 °C. At the time of use the working solutions were further diluted 1:6 in Knockout DMEM, added to the tissue culture plate and incubated at 37 °C for 30 min.

Fibronectin was prediluted in distilled water (diH₂O) and stored as a 1 mg/ml stock solution at -20 °C. At the time of use the stock solution was diluted 1:40, 2 µg/cm² fibronectin were added to the tissue culture plate and incubated for 30 min at 37 °C. Ready-made 0,1% gelatin solution was added to the tissue culture plastic ware for 30 min at 37 °C.

8 µg/cm² collagen IV (Col (α1)₂α2 (IV)), diluted in PBS (Mg²⁺, Ca²⁺) was incubated for 24 h at 4 °C.

Ready-made 0,1 mg/ml stock solutions of laminin 511 and 521 were diluted in PBS (Mg²⁺, Ca²⁺) to the working concentration. 1 µg/cm² was added to the tissue culture for 24 h at 4 °C. The coating solutions were removed, and the culture surface was washed with PBS once prior to cell seeding.

3.2.1.3 hiPSC culture

Human induced pluripotent stem cells were cultured in E8 medium under hypoxic conditions. The medium was changed daily. hiPSC cultures were checked daily for differentiated regions under the microscope. These were mechanically removed with the scraping tool.

The cells were routinely split 1:6 every 5 to 7 days. The well was washed once with 0,5 mM EDTA. To detach the cells 1 ml 0,5 mM EDTA was added for 3-5 min at 37 °C.

Once the borders of the colonies started to roll up the EDTA was aspirated and 3 ml of E8 medium was added. The colonies were dislodged with a cell scraper and broken into smaller colonies by pipetting them up and down three times with a 5 ml pipette. 500 μ l cells suspension was then transferred to a new Geltrex-coated well prefilled with fresh E8 medium.

3.2.1.4 hiPSC single cell harvest with Accutase

hiPSCs were washed with 1 ml Knockout DMEM. Next, 1 ml Accutase was added per 6-well. After 5 min incubation at 37 °C, 1 ml of E8, 10 μ M Rho-associated protein kinase-inhibitor (ROCKi) was added. Cells were flushed off the culture surface and the cell suspension was homogenized by pipetting the solution carefully up and down a couple of times. The cell suspension was centrifuged for 5 min at 300 g and the pellet was resuspended in 2 ml E8, 10 μ M ROCKi. The cell number was determined using the Countess II Automated Cell Counter.

3.2.1.5 hiPSC-derived intermediate mesoderm cells

The GFP positive hiPSC line WISCi004-B was differentiated into intermediate mesoderm cells (IMCs) using a modified protocol by Lam et al.¹¹³. In brief, hiPSC were harvested as single cells using Accutase, as described in 3.2.1.4, and 4×10^5 cells seeded into each well of a Geltrex coated 6-well plate in E8 medium. Medium was changed at day 3 to advanced RPMI, 1x GlutaMAX, 5 μ M CHIR99021, 100 U/ml penicillin and 100 μ g/ml streptomycin for 36 h. For the next 72 h, the differentiation media was changed to advanced RPMI, 1x GlutaMAX, 100 ng/ml bFGF, 2 μ M retinoic acid, 100 U/ml penicillin and 100 μ g/ml streptomycin. Subsequently, the cells were cultured for 24 h in advanced RPMI, 1x GlutaMAX, 100 U/ml penicillin and 100 μ g/ml streptomycin. The cells were harvested as single cell suspension using Accutase.

3.2.1.6 hiPSC-derived renal progenitor cells

hiPSCs BIHi004-A were differentiated into renal progenitor cells (RPCs) using the protocol by Hariharan et al.¹¹⁷. hiPSC colonies were grown to 90% confluence. Then the medium was changed to AB4RA medium (APEL2 medium, 5% PFHMII, 10 ng/ml Activin A, 30 ng/ml bone morphogenic protein 4 (BMP4), 1 μ M retinoic acid and 100 U/ml penicillin and

100 µg/ml streptomycin). Medium changes were repeated on day one and two of the differentiation. On day 4 the medium was changed to GDNF medium (APEL2 medium, 5% PFHMII, 150 ng/ml glial cell-derived neurotrophic factor (GDNF), 100 U/ml penicillin and 100 µg/ml streptomycin). The GDNF medium was changed every second day. The cells were harvested on day 8 as single cell suspension using Trypsin.

For cryopreservation the cells were transferred into a 15 ml falcon and centrifuged at 300 g for 5 min. The supernatant was removed, and the pellet was resuspended in fetal calf serum (FCS) containing 10% DMSO. 5×10^6 cells were transferred into each cryo-vial. The vials were slowly cooled down to -80 °C using a Mr. Frosty freezing container overnight. The next day the vials were transferred to liquid N₂ tanks and stored at -196 °C.

3.2.1.7 hiPSC-derived renal tubular epithelial cells

Renal tubular epithelial cells (RTECs) were differentiated in 6 days from hiPSC-derived RPCs. RPCs were thawed or freshly harvested on day 8 of differentiation, see 3.2.1.6. The frozen vials were thawed in a 37 °C water bath. The cell suspension was then transferred into cold DMEM, 10% FCS and centrifuged at 300 g for 5 min. The supernatant was removed, and the cell pellet resuspended in renal epithelial growth medium (REGM) medium.

hiPSC-derived RPCs were seeded onto 1 µg/cm² laminin-521 coated cell culture plates with a cell density of $1,25 \times 10^5$ fresh cells/cm² or $2,25 \times 10^5$ thawed cells/cm². Cells were cultured for six days with medium changes every other day.

3.2.1.8 hiPSC-derived endothelial cells

Endothelial cells were differentiated from the hiPSC lines BIHi004-A or BCRTi005-A according to a protocol by Patsch et al.¹⁰⁹. hiPSCs were harvested as single cells with Accutase, as described in 3.2.1.4. 5×10^4 cells/cm² were seeded into Geltrex coated T175 cell culture flasks in E8 medium, 10 µM ROCKi. The next day, day 0 of the differentiation, the medium was changed to 120 ml priming medium made from DMEM/F-12:Neurobasal 1:1, 2% B-27 without Vitamin A, 1% N-2, 25 ng/ml BMP4 and 7 µM CHIR99021. At day 3 and 4 the medium was exchanged with 60 ml endothelial cell induction medium consisting of StemPro-34 serum free medium, StemPro-34 nutrient supplement, 1% GlutaMAX, 200 ng/ml VEGF, 2 µM forskolin and 100 U/ml penicillin and 100 µg/ml streptomycin.

At day 5 the cells were harvested, sorted with magnetic-activated cell sorting (MACS) and reseeded into expansion medium. First, the cell layer was washed with 10 ml PBS. Next, 5 ml prewarmed 0,05% Trypsin-EDTA were added for 4 min at 37 °C. The digestion was stopped by adding 10 ml MACS buffer made from PBS, 0,5% FCS, 2 mM EDTA. The cell suspension was centrifuged for 5 min at 300 g, the cell pellet was resuspended in 80 µl MACS buffer/10⁷ cells. 20 µl MicroBeads conjugated to monoclonal anti-human CD144 antibodies/10⁷ cells were added and the cells were incubated for 15 min at 4 °C, to magnetically label the CD144+ cells. Then, the cells were washed with 2 ml MACS buffer, resuspended in 500 µl MACS buffer and transferred onto an MS MACS-column that was rinsed with 500 µl MACS buffer and placed into the magnetic field before. The column was washed thrice with 500 µl MACS buffer to wash out unlabeled CD144- cells. To collect the magnetically bound CD144+ cells, the column was removed from the magnetic field and flushed with 1ml MACS buffer.

For endothelial cell maturation and expansion, the sorted cells were seeded onto 0,1% gelatin or 2 µg/cm² fibronectin coated plates and cultured in either EGM-FCS-SB medium, EC-SFM or StemPro-34 medium, as listed in Table 10. Medium was changed every other day. Cells were splitted with Trypsin approximately every 6 days, when they reached 80% confluence. Differentiation and sorting efficiency as well as phenotype stability were checked by flow cytometry before and after MACS and at every cell split, see 3.2.12.

Table 10: List of the expansion media for hiPSC-derived endothelial cells

EC expansion medium	Composition	Seeding density	Reference
EGM-FCS-SB	EGM-2 without hydrocortisone 20 % FCS 10 mM SB431542 1% P/S	5000 cells/cm ²	Ren et al. 2015 ¹⁴¹
EC-SFM	EC serum free medium 1% human serum 30 ng/ml VEGF 20 ng/ml bFGF	5000 cells/cm ²	Orlova et al. 2014 ¹⁴²
StemPro-34	StemPro-34 serum free medium StemPro-34 supplements 1% GlutaMAX 50 ng/ml VEGF 1% P/S	26000 cells/cm ²	Patsch et al. 2015 ¹⁰⁹

3.2.1.9 Human umbilical vein endothelial cells

Human umbilical vein endothelial cells (HUVECs) were cultured in T175 cell culture flasks in 15 ml endothelial growth medium 2 (EGM-2) supplemented with 10% FCS, 100 U/ml penicillin and 100 µg/ml streptomycin. The medium was changed every other day. HUVECs were seeded with a density of 7000 cells/cm² and were splitted with Trypsin approximately every 6 days, when they reached 80% confluence. Cells until passage eight were used for experiments.

3.2.2 Decellularization of porcine kidney tissue by immersion and agitation

3.2.2.1 Organ preparation

Cadaveric porcine kidneys were collected from infant (1-3 months) piglets and stored at -20 °C for at least 24 h. All animal experiments were performed under the guidelines of the German Animal Protection Law with approval of the local responsible authorities (Landesamt für Gesundheit und Soziales Berlin). Decellularization of kidneys was performed by immersion and agitation of tissue samples in decellularization solutions. Frozen porcine kidneys were thawed, and the renal cortex was sampled into cubes with the size of approximately 0,5 x 0,5 x 0,5 cm.

3.2.2.2 Decellularization procedure

The tissue cubes were washed three times for 5 min in DMEM w/o phenol red. After incubation for 24 h in diH₂O, which was changed once after 4 h, the tissue samples were immersed in three different detergents: 1% (w/v) SDS, 1% (v/v) TX-100 or 1% (w/v) SDC for 7-10 days. The decellularization solutions were initially changed after 8 h and thereafter every 48 h. Agitation was applied by using a shaker at 50 rpm throughout the incubation. Decellularization was carried out at 4 °C, at room temperature (RT; 22-24 °C) or at 37 °C to examine the influence of the temperature. The decellularization was terminated when no further changes in transparency and macroscopic appearance were observed for 48 h. The transparent tissue samples were washed three times in DMEM, then incubated in 350 IU/mL DNase I in DMEM for 18 h at 37 °C and finally washed again three times in DMEM supplemented with 100 U/ml penicillin and 100 µg/ml streptomycin and 2,5 mg/ml amphotericin B (AntiAnti) for 18 h at RT.

To assess cell attachment and the elastic modulus, 50 μm frozen kidney sections were mounted on poly[octadecene-*alt*-(maleic anhydride)] (POMA)-coated glass-coverslips³⁰ and decellularization performed at 4 °C as described above.

Table 11: Overview of decellularization by immersion and agitation conditions

	Wash	Decellularization			Wash
Temperature	RT	4 °C, RT, 37 °C			RT
Duration	0,25 h	24 h	168-240 h	18 h	18 h
Reagents	DMEM	diH ₂ O	1% SDC 1% SDS 1% TX-100	DMEM + 350 IU/ml DNase I	DMEM

diH₂O, distilled water; DMEM, Dulbecco's Modified Eagle's Medium w/o phenol red; RT, 22-24°C; SDS, sodium dodecyl sulfate; SDC, sodium deoxycholate; TX-100, Triton X-100

3.2.3 Decellularization of whole rat kidneys by perfusion

3.2.3.1 Organ preparation

Kidneys were collected from cadaveric 12-week-old Wistar rats that were injected with 500 U heparin prior to sacrifice. After disinfecting the abdominal fur, the abdomen was opened by cutting the skin and abdominal muscles. The intestine was carefully removed from the abdominal cavity and placed at the left side of the rat, without disrupting the intestinal wall. Both ureters were cleared from fat with cotton swabs and cut close the bladder.

Next, the renal arteries were prepared for cannulation. Abdominal fat and connective tissue were removed. The renal vein was detached from the renal artery and cut close to the kidney. The aorta was cut between the superior mesenteric artery and the right renal artery, between right and left renal artery and below the left renal artery, as depicted in Figure 10A. The resulting aorta sections were cut open to produce patches attached to the renal arteries. These patches facilitate the insertion of the cannula into the renal arteries. A sterile feeding needle was used as the artery cannula. It was prefilled with PBS, 50 U/ml Heparin, 1% AntiAnti and pushed into the renal artery. The ball-head of the feeding needle was placed between the inferior suprarenal artery and the branching of the renal artery, see Figure 10B. The cannula was fixed, and the cannulation sealed by placing a ligature directly behind the ball-head of the feeding needle with a double surgical knot with a 7-0 silk suture. The cannulated kidney was removed from the abdomen by cutting away the adipose capsule and the adrenal gland.

The released kidney was flushed with 5 ml PBS, 50 U/ml Heparin, 1% AntiAnti to remove blood from the vessels inside the organ.

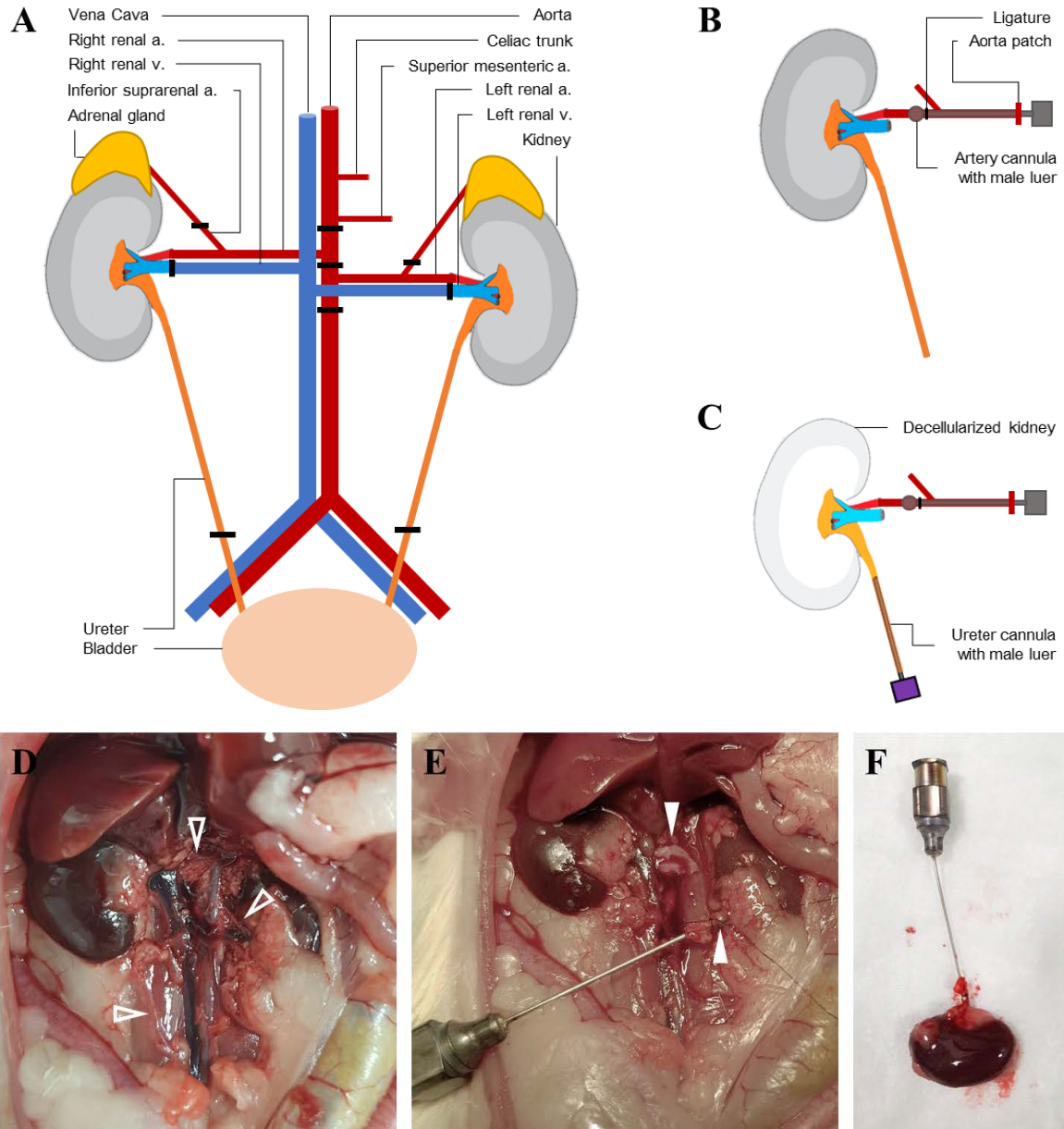


Figure 10: Organ preparation for decellularization of whole rat kidneys by perfusion (A) Schematic overview of the anatomy of the urinary tract and the abdominal blood vessels of a rat. Black lines indicate the cutting sites during the cannulation procedure. (D) A photograph of the same area. Arrows indicate the prepared left and right renal arteries and the ureter. (E) The arteries were cut into patches, as indicated by white arrows. The patches could easily be cannulated with a ball-headed feeding needle. (B,F) The cannulated kidney was removed from the body, to this end the vein and ureter were cut. (C) After decellularization by perfusion through the artery, the ureter was cannulated for recellularization via the ureter.

3.2.3.2 Assembly of the decellularization perfusion bioreactor

The perfusions system was assembled under sterile conditions in class II laminar flow hoods. All parts were sterile prior to assembly. Two kidneys were decellularized in one perfusion bioreactor.

Therefore, two kidneys were placed into one decellularization chamber, a 1000 ml laboratory bottle with a hose connection screw cap and connected via the cannulated arteries to one perfusor line each. The perfusor lines were threaded through the IN-ports 1 and 2 of the hose connection screw cap and connected to the pump tubing. The pump tubing was then connected via

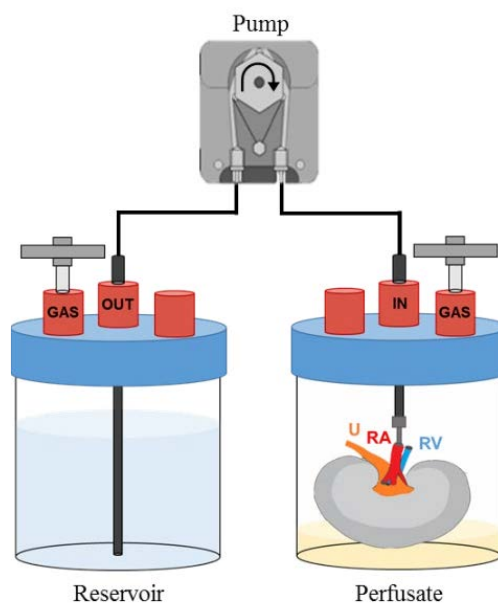


Figure 11: Schematic setup of the decellularization perfusion bioreactor

a 3-way stopcock to the OUT-port of the decellularization agent reservoir. The decellularization agent reservoir was also assembled from a 1000 ml laboratory bottle with a hose connection screw cap.

All connections were made with Luer-Lock components. The system was prefilled with decellularization agents before perfusion start.

3.2.3.3 Decellularization procedure

The perfusion bioreactor was either placed at room temperature or in 4 °C to examine the influence of the temperature. The pump tubing was clamped into the perfusion pump and the perfusion was started with a flow rate of 0,5 ml/min. The kidneys were first perfused with PBS containing 50 U/ml Heparin and 1% AntiAnti for 30 min to remove residual blood. Next, kidneys that were decellularized according to the SDC protocol were perfused for 120 h with 1% SDC and then washed with PBS, 1% AntiAnti for 36 h (Table 12). Kidneys that were decellularized according to the SDS/TX-100 protocol (adapted from Song et al.¹²³) were perfused with 1% SDS, diH₂O and 1% TX-100 for 16 h, 30 min and 30 min, respectively (Table 13). Fully filled decellularization chambers and empty decellularization agent reservoirs were exchanged under the sterile flow hood. Decellularized kidneys were stored at 4 °C in PBS, 1% AntiAnti.

Table 12: SDC protocol conditions for decellularization by perfusion

	Wash	Decellularization	Wash
Temperature	4 °C, RT	4 °C, RT	4 °C, RT
Duration	0,5 h	120 h	36 h
Reagents	PBS, 50 U/ml heparin, 1% AntiAnti	1% SDC	PBS, 1% AntiAnti

diH₂O, distilled water; PBS, phosphate buffered saline; RT, 22-24°C; SDC, sodium deoxycholate; AntiAnti, mixture of penicillin, streptomycin and amphotericin B

Table 13: SDS/TX-100 protocol conditions for decellularization by perfusion

	Wash	Decellularization			Wash
Temperature	4 °C, RT	4 °C, RT			4 °C, RT
Duration	0,5 h	16 h	0,5 h	0,5 h	36 h
Reagents	PBS, 50 U/ml heparin, 1% AntiAnti	1% SDS	diH ₂ O	1% TX-100	PBS, 1% AntiAnti

diH₂O, distilled water; PBS, phosphate buffered saline; RT, 22-24°C; SDS, sodium dodecyl sulfate; TX-100, Triton X-100; AntiAnti, mixture of penicillin, streptomycin and amphotericin B

3.2.4 Characterization of decellularized kidneys

3.2.4.1 DNA quantification

Samples were snap frozen and pulverized by grinding in a precooled mortar, then dried for 1,5 h using a vacuum concentrator and digested in 0,2 mg/ml proteinase K solution (in 100 mM Tris, 5 mM EDTA, 0,2% SDS, 0,2 M NaCl) overnight at 55 °C. After inactivating the proteinase K for 10 min at 96 °C, the DNA was extracted by phenol-chloroform extraction. DNA concentration was quantified using a Nanodrop spectrometer and normalized to the tissue dry weight.

3.2.4.2 Glycosaminoglycan quantification

Sulfated GAGs were quantified in native and decellularized kidneys using the Blyscan GAG assay. 30 mg of pulverized sample was digested with 125 µg/ml papain solution (in 0,1 M sodium acetate, 5 mM cysteine-HCl, 50 mM EDTA, pH 6,0) for 16 h at 65 °C. GAGs were precipitated with dimethylmethylene blue dye and dissolved in the dye dissociation reagent. The absorbance at 595 nm was measured using a microplate reader and compared to a chondroitin-4-sulfate standard.

3.2.4.3 Collagen quantification

Total collagen was quantified by measuring the hydroxyproline content with the Total Collagen Assay Kit. 5 mg of pulverized sample was hydrolyzed with 6 M HCl at 95 °C overnight. Hydroxyproline residues were oxidized and stained according to the manufacturer's instructions. The absorbance was measured at 570 nm and compared to a hydrolyzed collagen I standard.

3.2.4.4 Cytokine quantification

230 mg sample powder was lyophilized, the dry weight determined and then dissolved in 1 ml RIPA buffer (150 mM NaCl, 50 mM Tris, 1% TX-100, 0,5% SDC, 0,1% SDS). Lysates were sonicated for 20 s, incubated for 20 h at 4 °C on a shaker and centrifuged at 13000 g for 10 min. The VEGF and bFGF content in the supernatants were determined with the hVEGF ELISA Kit and the hbFGF ELISA Kit. Both kits were used according to the manufacturer's instructions. The absorbance was measured at 450 nm and 650 nm. Cytokine concentrations were normalized to the tissue dry weight.

3.2.4.5 Elastic modulus

The elastic modulus of glomerular structures in decellularized and native porcine kidney ECM was determined with atomic force microscopy (AFM), as published earlier¹⁴³. In short, the frozen tissue was mounted and decellularized on a glass cover slip (see 3.2.2.2). The glomerular ECM was probed by force measurements with an MFP3D-Bio AFM using a spherical probe with a radius of 3,35 µm and an indentation depth of ~300 nm.

The bulk elasticity of the PDMS gels was assessed in an unconfined compression experiment with the Bose test bench LM 1 ElectroForce. 4 mm punch biopsies were compressed at a rate of 1 mm/min with a 225 N load cell. The displacement was set to 10% of the biopsy's height and the displacement data were sampled at 100 Hz. The elastic bulk modulus was calculated as the best-fit slope of the resulting stress/strain curve.

3.2.5 Recellularization of immersion-decellularized porcine kidney scaffolds

Intermediate mesoderm cells were suspended in advanced RPMI, 1x GlutaMAX, 100 U/ml penicillin and 100 µg/ml streptomycin. 3×10^5 cells/cm² were seeded on the decellularized ECM mounted on a glass cover slip (see 3.2.2.2). Glass coverslips and cell culture treated polystyrene were used as controls. Experiments were performed in triplicates. 24 h after seeding the cells on the matrix, the cumulative cell viability was assessed with the resazurin reduction assay (see 3.2.7.1).

3.2.6 Recellularization of perfusion-decellularized whole rat kidneys

3.2.6.1 Assembly of the recellularization perfusion bioreactor

The perfusions bioreactor was assembled under sterile conditions in class II laminar flow hoods. All parts were sterile prior to assembly. The bioreactor was assembled from a 50 ml laboratory bottle, filled with 20- 50 ml medium, and a hose connection screw cap providing three ports. The gas-port was connected to a 0,2 µm gas filter. The end of a 150 cm perfusor line dipped into the medium. The other end of the same line was threaded through the OUT-port of the screw cap and connected to a 3-way stopcock, which served as a sample port to draw medium samples for glucose, lactate and lactate dehydrogenase (LDH) measurements (see 3.2.7.1). The 3-way stopcock was connected to the pump tubing, which was connected to the membrane oxygenator. A 50 cm perfusor line was used to connect the membrane oxygenator to the pH sensor, pO₂ sensor, pressure sensor and a second 3-way stopcock in series. The 3-way stopcock was connected to the IN-port of the screw cap to which the decellularized kidney was attached via the cannulated artery after all hoses were prefilled with medium. The assembled bioreactor was placed inside an incubator, where the gas inlet of the oxygenator was connected to a humidifier and then to a gas mixing device, the pump tubing was clamped into the perfusion pump and all sensors were connected to the measuring instruments. The incubator heated to 37 °C. The perfusion bioreactor was controlled via the control software. All connections were made with Luer-Lock components.

3.2.6.2 Recellularization strategies

Decellularized rat kidneys were preconditioned for recellularization by perfusion with 30 ml medium in the recellularization-perfusion bioreactor for several hours. Cells were either seeded via the artery, the ureter or via injection into the cortex with a syringe.

For **arterial seeding with low pressure** 3×10^7 RPCs, 5×10^7 HUVECs or 5×10^7 ECs were harvested, resuspended in 1 ml REGM or EGM-2, respectively, and filled into a syringe. Bubbles were pushed out of the syringe and the renal cannula was filled with medium to ensure no bubble would be pushed into the decellularized kidney. Next, the cell suspension was injected through the cannula in the renal artery into the decellularized kidney with a speed of approximately 2 ml/min. Swelling of the kidney was observed if no leakage occurred. The kidney was then placed into the bioreactor and the artery cannula was connected via Luer-Lock to the IN-port perfusor line. The bioreactor was placed overnight in the incubator without perfusion to facilitate cell attachment. The perfusion culture was started the next morning.

Kidneys were **partially digested with trypsin** before cell seeding to facilitate the cell migration from the vascular tree into the renal tubules. Therefore, 1 ml 0,25% trypsin in REGM and 1% AntiAnti were injected into the renal artery followed by 1 h incubation at 37 °C. The digest was stopped by injecting 1 ml DMEM, 10% FCS and subsequent perfusion with PBS at 0,5 ml/min for 30 min to remove residual trypsin. Next, the preconditioning and arterial seeding with low pressure was performed.

For **arterial seeding with high pressure** 3×10^7 RPCs were harvested, resuspended in 2 ml REGM and filled into a syringe. The decellularized kidney was placed into the bioreactor and the cells were injected into the cell seeding port. The perfusion was started immediately with 25 ml/min for 15 min.

For seeding via the **ureter without vacuum**, the ureter was cannulated using a 26-gauge Neoflon catheter, as illustrated in Figure 10C. The decellularized ureter is very thin, therefore the tip of the catheter was beveled without producing a sharp tip that would tear the ureter easily. An incision was made in the proximal ureter, the cannula inserted and fixed with a ligature. 3×10^7 RPCs resuspended in 1 ml REGM were injected slowly into the kidney through the ureter cannula. The kidney was connected via the arterial cannula to the perfusion bioreactor and cultured under static conditions overnight before perfusion culture started.

When the cells were seeded via the **ureter with vacuum**, 3×10^7 RPCs in 100 μ l REGM were injected into the ureter cannula. The decellularized kidney was then placed in the recellularization bioreactor and connected via the ureter cannula to the IN-port perfusor line. The gas-port was connected to a vacuum pump and 100 mbar vacuum was applied to suck 500 μ l REGM from the cell seeding port into the ureter. The perfusion culture was started after overnight static culture.

In the **syringe seeding** process 3×10^7 RPCs were resuspended in 1 ml or 100 μ l REGM and filled into a 1ml or 100 μ l syringe. Cells were injected into the cortex with 10x 100 μ l or 20x 5 μ l injections using a 27-gauge needle. The perfusion culture was started the next morning.

3.2.6.3 Perfusion culture

Recellularized kidneys were cultured for three to six days in the perfusion bioreactor. 20-50 ml medium was circulated with 0,25-0,5 ml/min. The arterial high pressure seeding experiment was perfused with 4 ml/min according to the protocol by Caralt et al.¹⁴⁴. The medium was exchanged every second day. RPCs were cultured in REGM, HUVECs were cultured in EGM-2 and hiPSC-ECs were cultured in EGM-FCS-SB medium. 5% CO₂ and 95% air were perfused through the membrane oxygenator for pH control. pH and pressure were constantly monitored with the LabView control software. Medium samples were drawn at the sample port with a 1 ml syringe for glucose, lactate and LDH quantification every 12-24 h, see 3.2.7.1. Before terminating the perfusion culture, the resazurin reduction assay was performed, see 3.2.7.2.

3.2.7 Characterization of recellularized kidneys

3.2.7.1 Glucose, lactate, LDH measurement in the culture medium

600 μ l medium were drawn from the sample port of the recellularization perfusion bioreactor. 250 μ l were injected into the ABL 700 for glucose and lactate quantification. 350 μ l were sent to Labor Berlin for the determination of the LDH concentration.

3.2.7.2 Resazurin reduction assay

Resazurin is a soluble dye that is reduced to resorufin by cells, proportional to their metabolic activity and number. Resorufin is highly fluorescent and serves as a noninvasive tool to measure cellularity and growth within ECM scaffolds¹⁴⁵.

Resazurin was added to a final concentration of 44 μM to the culture medium. Perfusion or static cell culture was continued for 90 min. The relative fluorescent units (RFU) of the fluorescent resorufin were measured by excitation at 535 nm and readout at 615 nm in a multiplate reader.

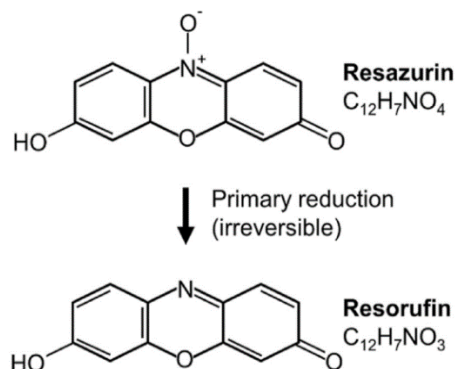


Figure 12: Resazurin is reduced to the fluorescent resorufin by metabolically active cells¹⁴⁵.

3.2.7.3 Quantification of cells by image analysis

Cell attachment on immersion-decellularized porcine kidneys was assessed by scanning the samples with the Operetta high content imaging system after 30 h and 72 h. Attached GFP-positive cells were distinguished from non-attached GFP-positive cells and counted by running the analysis sequence “Count attached GFP+ cells” with the Columbus image analysis server (see Figure S1).

The cell number in recellularized rat kidneys was determined after the termination of the perfusion culture. 4',6-diamidino-2-phenylindole (DAPI) stained paraffin sections of the recellularized kidneys (according to 3.2.11) were scanned with the Operetta high content imaging system and analyzed with the Columbus image analysis server using the analysis sequence “Count DAPI-nuclei on kidney sections” (see Figure S2). The counted cells were normalized to the scanned images per kidney section.

3.2.8 Tuning of the pressure and pH controllers

To tune the pressure and the pH controller the system was first characterized by recording the step response. Therefore, the control variable (CV) was changed and the process variable (PV) recorded.

With these data the controller was tuned. The reference-variable response was recorded to check the tuning. Therefore, the setpoint was changed and the control variable and process variable recorded. With these data the control deviation and the control settling time was determined. Additionally, the disturbance response for the pressure controller was recorded. All settings are shown in Table 14.

Table 14: System settings for controller tuning

Response	Action	Pressure controller	pH controller
step response	CV change	5 rpm → 10 rpm or 40 rpm	0% CO ₂ → 10% CO ₂
reference-variable response	SP change	10 mmHg ↔ 30 mmHg	pH 7,4 ↔ pH 7,2
disturbance response	disturbance	3-way stopcock of cell seeding port closed	300 mg Citrate bolus and 300 mg NaOH bolus

3.2.9 PDMS gel assay

PDMS gels of three different stiffnesses were produced. Sylgard kit 527 or 184 were used in distinct silicone base to curing agent ratios according to the desired stiffness of the PDMS, as shown in Table 15. The base and curing agent were thoroughly mixed, degassed and 200 µl gel were poured into each well of a 12-well plate. The PDMS was cured for 12 h at 55°C. The bulk *E* modulus of the cured gels were determined as described in 3.2.4.5.

Table 15: PDMS preparations

<i>E</i> modulus	Product	Base	Curing agent	Ratio
4 kPa	SYLGARD 527 A&B Silicone Dielectric Gel	9,81 g	10,19 g	0,96
200 kPa	SYLGARD 527 A&B Silicone Dielectric Gel	2,03 g	17,93 g	0,115
2 MPa	SYLGARD 184 Silicone Elastomer Kit	18,19 g	1,81 g	10

PDMS requires a polydopamine coating to reduce hydrophobicity to and improve cell attachment. Therefore, the PDMS was treated with 0,01% dopamine in 10 mM Tris-HCl, pH 8,5, for 24 h at RT. Residual dopamine was removed by washing with PBS for 7 days. The polydopamine coated PDMS was then coated in another step with extracellular matrix proteins. 1 µg/cm² laminin 511, 1 µg/cm² laminin 521 and/or 8 µg/cm² collagen IV in PBS including Mg²⁺ and Ca²⁺ were added to well plate for 24 h at 4°C.

Cryopreserved hiPSC-derived renal progenitor cells were thawed and seeded onto the PDMS surfaces and differentiated into hiPSC-derived renal tubular epithelial cells, as described in 3.2.1.7. Six days after cell seeding, the ribonucleic acid (RNA) was harvested for qPCR analysis.

3.2.10 Quantitative polymerase chain reaction

RNA isolation from cells was performed using the RNeasy Plus Mini kit according to the manufacturer's instructions. The RNA concentration was determined with the NanoDrop and the RNA was stored at -80 °C. Next, the RNA was reverse transcribed into complementary DNA (cDNA) using the TaqMan Reverse Transcription Reagents cDNA kit following the manufacturer's instructions. The reverse transcription polymerase chain reaction (RT-PCR) reaction mix and cycling conditions are displayed in Table 16 and Table 17. The cDNA was diluted 1:1 with diH₂O and stored at 4 °C.

Table 16: TaqMan RT Reaction Mix

Component	Concentration	Volume
RT Buffer	10x	2,0 µl
MgCl ₂	25 mM	1,4 µl
dNTP mix	10 mM	4,0 µl
Random hexamer primer	50 µM	1,0 µl
RNase Inhibitor	20 U/µL	1,0 µl
MultiScribe RT	50 U/µL	1,0 µl
Template RNA	<1 µg/rxn	9,6 µl

Table 17: RT-PCR cycling conditions

Temperature	Time
25 °C	10 min
37 °C	30 min
95 °C	5 min
4 °C	indefinitely

Quantitative polymerase chain reaction (qPCR) was performed using the TaqMan Fast Advanced Master Mix and TaqMan Gene Expression Assays for *AQP1*, *ATP1A1*, *PODXL*, *SIX2*, *SLC12A2*, *SLC12A3*, *SYNPO* and *WT1*. According to the manufacturer's instructions 1 µl cDNA was used per reaction in a total volume of 10 µl, as shown in Table 18. The assay was conducted in 384-well PCR plates in the QuantStudio 6 Flex Real-Time PCR System.

Cycling conditions are shown in Table 19. *GAPDH* and *RNAI8S5* were used as housekeeping genes. Relative gene expression was calculated with the $2^{-\Delta\Delta C_t}$ method.

Table 18: TaqMan qPCR Reaction Mix for a 384-well plate

Component	Concentration	Volume
TaqMan Fast Advanced Master Mix	2x	5 μ l
TaqMan Gene Expression Assay	20x	0,5 μ l
Nuclease-free water		3,5 μ l
cDNA template		1 μ l

Table 19: qPCR cycling conditions

Temperature	Time	
50 °C	2 min	
95 °C	20 s	
95 °C	1 s	} 40 cycles
60 °C	20 s	

3.2.11 Histology and immunofluorescence staining

3.2.11.1 Paraffin embedding and sectioning

Native and decellularized kidney tissues were fixed in 4% phosphate-buffered formaldehyde solution for 24 h at RT. The fixed samples were then dehydrated in 12 steps in a tissue processor, as shown in Table 20, and embedded in paraffin.

Table 20: Dehydrating steps before embedding of tissue in paraffin blocks

Step	Reagent	Time	Step	Reagent	Time
1	70% EtOH	1 h	7	100% EtOH	2 h
2	80% EtOH	1 h	8	100% EtOH	3 h
3	80% EtOH	2 h	9	Xylol	1 h
4	96% EtOH	2 h	10	Xylol	1,5 h
5	96% EtOH	2 h	11	Paraffin, 65 °C	2 h
6	100% EtOH	2 h	12	Paraffin, 65 °C	2 h
				Total time	21,5h

Paraffin blocks were cut into 5 μ m sections using a microtome and stored at RT. Before HE or immunofluorescence staining the sections were deparaffinized and rehydrated according to the protocol depicted in Table 21.

Table 21: Rehydration of paraffin sections

Step	Reagent	Time
1	Xylol I	10 min
2	Xylol II	10 min
3	100% EtOH I	2 min
4	100% EtOH II	2 min
5	96% EtOH	2 min
6	80% EtOH	2 min
7	70% EtOH	2 min
8	diH ₂ O	10 s

3.2.11.2 HE staining

Hematoxylin and eosin (HE) staining was performed on rehydrated paraffin sections according to the protocol shown in Table 22. In short, sections were stained for 5 min in Mayer's acid hemalum, washed 15 min in tap water and stained for 2 min in Eosin Y. Sections were then dehydrated again and mounted with Roti-Histokitt. Imaging was performed using an inverse microscope.

Table 22: HE staining on rehydrated paraffin sections

Step	Reagent	Time
1	Mayer's acid hemalum	5 min
2	Running tap water	15 min
3	Eosin Y	2 min
4	diH ₂ O	10 s
5	96% EtOH	1 min
6	100% EtOH I	2 min
7	100% EtOH II	2 min
8	Xylol I	10 min
9	Xylol II	10 min

3.2.11.3 Immunofluorescence staining

Immunofluorescence staining on paraffin sections requires antigen retrieval treatment before the staining. Table 23 displays the applied antigen retrieval treatments for each antibody used. Thereafter, samples were permeabilized with 20 mM Tris-Base, 500 mM NaCl, 0,1% TX-100, pH 7,5 (T-TBS) three times for 5 min.

The samples were then blocked for 10 min with 1% bovine serum albumin (BSA) in 20 mM Tris-Base, 500 mM NaCl, pH 7,5 (TBS) and for 30 min with 5% donkey serum and 1% BSA in TBS before immunostaining. Primary antibodies were applied overnight at 4 °C. All

antibodies were diluted in 5% donkey serum and 1% BSA in TBS as listed in Table 23. After washing with T-TBS, slides were incubated with the secondary antibody Alexa647-conjugated polyclonal donkey anti-rabbit IgG in 1:500 dilution for 1h at RT. Finally, after washing in T-TBS for 5 min, sections were mounted with immunoselect antifading mounting medium including DAPI.

The same protocol was adapted to stain non-paraffin embedded samples, e.g. cells from cell culture experiments. Cells were fixed for only 10 min in 4% phosphate-buffered formaldehyde solution. No antigen retrieval treatment is necessary for these samples. These samples were not mounted, therefore staining with DAPI for 5 min and washing with diH₂O twice for 5 min was added to the end of the staining protocol.

For negative staining controls, the primary antibody was omitted.

Imaging was performed using either an inverse microscope or the Operetta high content imager and Columbus image analysis server.

Table 23: Antigen retrieval treatments for immunofluorescence staining on paraffin sections

Antibody	Dilution	Antigen retrieval
anti-fibronectin	1:300	TE buffer, pH 8, 10 min in pressure cooker
anti-laminin	1:100	TE buffer, pH 8, 10 min in pressure cooker
anti-collagen IV	1:200	TE buffer, pH 6, 10 min in pressure cooker
anti-collagen I	1:100	TE buffer, pH 8, 10 min in pressure cooker
anti-CD31	1:100	Dako Target Retrieval Solution, 20 min at 95 °C in water bath

3.2.12 Flow cytometry

Flow cytometric analysis of LHX1 and PAX2 was used to quantify the differentiation efficacy of hiPSC-derived IM cells. Cells were stained with LIVE/DEAD Fixable Blue Dead Cell Stain Kit for 30 min, permeabilized with BD FACS Permeabilizing Solution 2 for 15 min and blocked in 10% donkey serum for 30 min. Thereafter, cells were incubated for 30 min at RT with the anti-PAX2 and anti-LHX1 at 1:50 dilutions. After washing with 2% FCS in PBS, cells were incubated with 1:1000 AlexaFluor 647-conjugated donkey anti-rabbit IgG or AlexaFluor 647-conjugated donkey anti-mouse IgG for 30 min in the dark. Stained cells were analyzed using an LSR-II Fortessa flow cytometer and data analysis was conducted in FlowJo Version 9.

Flow cytometric analysis of CD31 and CD144 was used to check the differentiation efficacy of hiPSC-derived EC cells. 50000 cells were resuspended in 40 µl MACS buffer (PBS,

0,5% FCS, 2 mM EDTA), 10 μ l FcR Blocking Reagent, 2 μ l anti-CD31-APC and 1 μ l anti-CD144-FITC and stained for 10 min at 4 °C. After washing in 2 ml MACS buffer, the stained cells were resuspended in 200 μ l MACS buffer and 0,5 μ l Propidium Iodid, measured with MACSQuant VYB and analyzed with FCS Express 5 Plus software.

3.2.13 Statistical analysis

Quantitative results are reported as means \pm standard error of the mean (SEM). Data were tested for normal distribution using the D'Agostino-Pearson omnibus K2 normality test. Data sets with normal distribution were analyzed for significant differences with the unpaired t-test or one-way analysis of variance (ANOVA) followed by Tukey's post test. Non-parametric tests were applied to data sets without normal distributed. The Mann-Whitney test or Kruskal-Wallis and Dunn's post test were utilized. All statistical testing was performed using GraphPad Prism 5. The significance level was set to 0,05.

4 Results

4.1 Development of a perfusion bioreactor for de- and recellularization of whole kidneys

4.1.1 Setup

For de- and recellularization of whole rat kidneys it is compulsory to perfuse the organ with either decellularization reagents or cells and cell culture medium. Therefore, a perfusion bioreactor that permits de- and recellularization in the same system was developed (Figure 13 and Figure 14).

For recellularization, cell culture conditions have to be provided. Therefore, sterility has top priority. Thus, the system was designed to be assembled under a class II laminar flow hood and to minimize reopening during the whole culture period. The kidney is placed in a bioreactor and via Luer-Lock attached with the cannulated artery to sterile tubing. The cell culture medium is also filled into the bioreactor and circulated with a peristaltic pump using sterile pump tubing. The medium is perfused into the renal artery, then drains through ureter, renal vein and decellularized parenchyma back into the bioreactor.

The perfusion speed influences the pressure applied to the kidney. To avoid damage to the delicate kidney structures or to the reseeded cells by an exceedingly high pressure, the pressure has to be monitored and the perfusion speed has to be controlled. Therefore, a pressure sensor was included into the perfusion circuit.

Another factor to ensure cell culture conditions is to maintain a physiological pH of the perfusion medium. Most cell culture media contain a bicarbonate buffer system. This permits control of the pH via CO₂ gassing. Therefore, an optical flow through pH sensor and an oxygenator were integrated into the perfusion circuit. The oxygenator contains 1 m gas permeable silicone tubing that is perfused with culture medium and surrounded by gas. The oxygenator is aerated by a gas mixing device that controls the CO₂ percentage.

In first test runs of the system, excessive medium evaporation that led to an increase in medium osmolarity could be observed, caused by low humidity of the used gas mixture. This problem was solved by the installation of a gas humidifier between oxygenator and gas

mixing device. Additionally, an oxygen flow through sensor was integrated into the perfusion bioreactor. Lastly, for temperature control, the whole system was placed inside an incubator, set to 37 °C. The system is equipped with two ports. One port for cell seeding and one for medium sampling.

All sensors, the peristaltic pump and the gas mixing device are connected to a computer running the control software. The exact specifications are listed in Table 24.

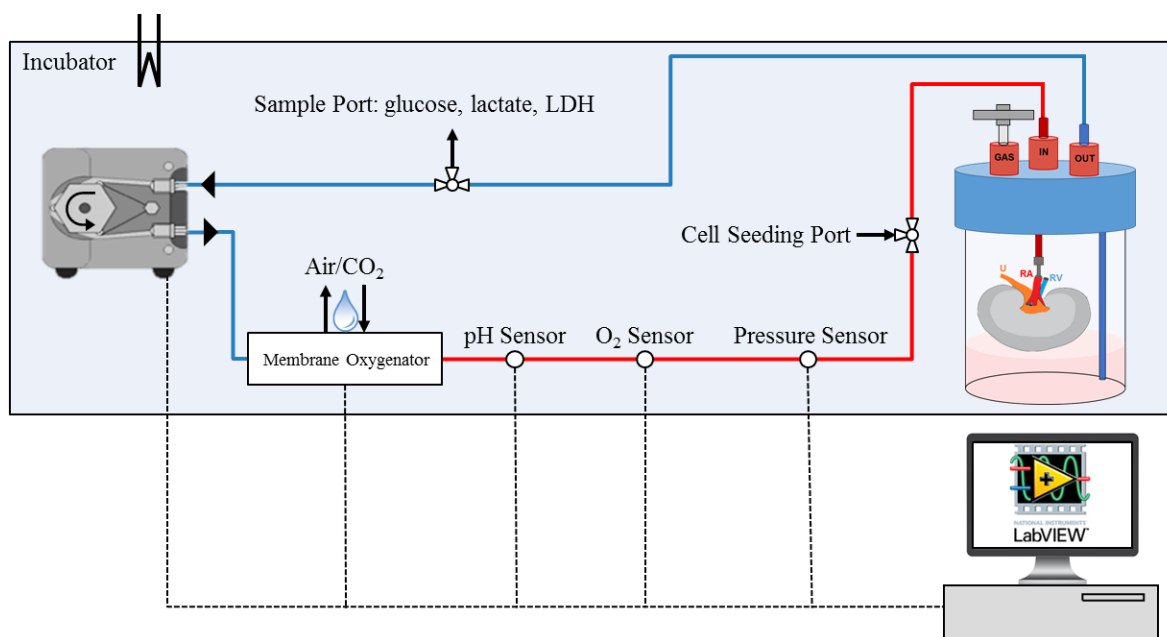


Figure 13: Schematic setup of the recellularization perfusion bioreactor. The perfusion bioreactor is placed inside an incubator for temperature control. The cannulated kidney is connected to the perfusion tubing inside a sterile chamber. Decellularization agents or cell culture medium are circulated via a peristaltic pump whose speed is controlled to attain the required perfusion pressure. A membrane oxygenator is used to adjust the pH of the medium via the CO₂ content in the gas flow. The gas is humidified before entering the membrane oxygenator to reduce evaporation. Ports are installed for medium sampling and cell seeding. A LabVIEW based control software monitors and controls the perfusion bioreactor.

Table 24: Overview over the technical background of the perfusion bioreactor

	Pressure controller	pH controller
Control variable	Pump speed	CO ₂
Control element	Peristaltic pump, connected to a PC via serial interface, communication via a provided LabVIEW driver	Gas mixing device, connected to a PC via USB, communication protocol provided and implemented in LabVIEW via VISA elements
Process variable	Pressure	pH
Sensor	Pressure sensor, amplifier connected to the voltage input module NI9201 in the NIcDAQ-9174 chassis, communication via DAQmx elements in LabVIEW	Fiber optic pH sensor, connection to the PC via serial interface, communication protocol provided and implemented in LabVIEW via VISA elements
Setpoint	Pressure setpoint	pH setpoint

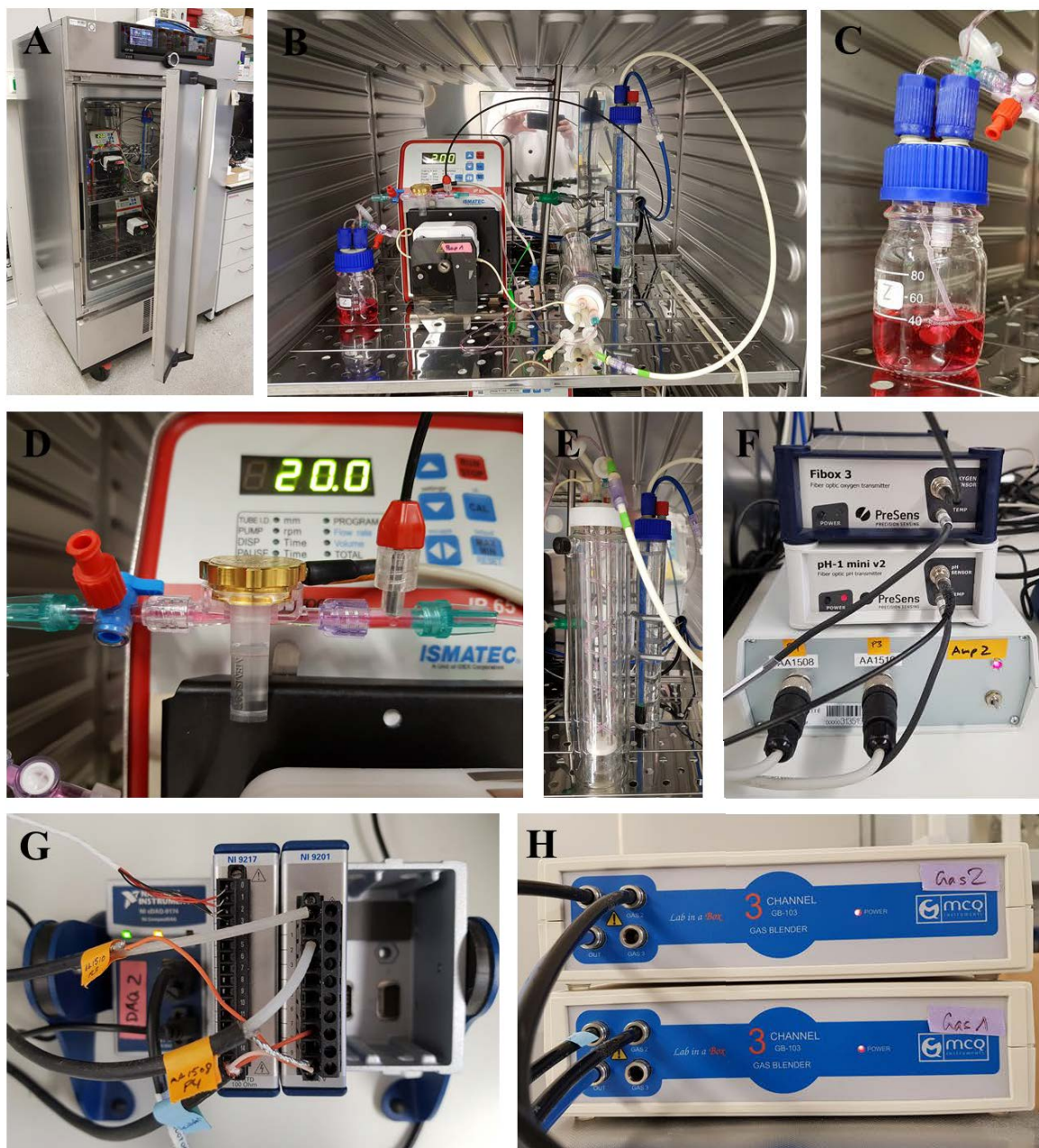
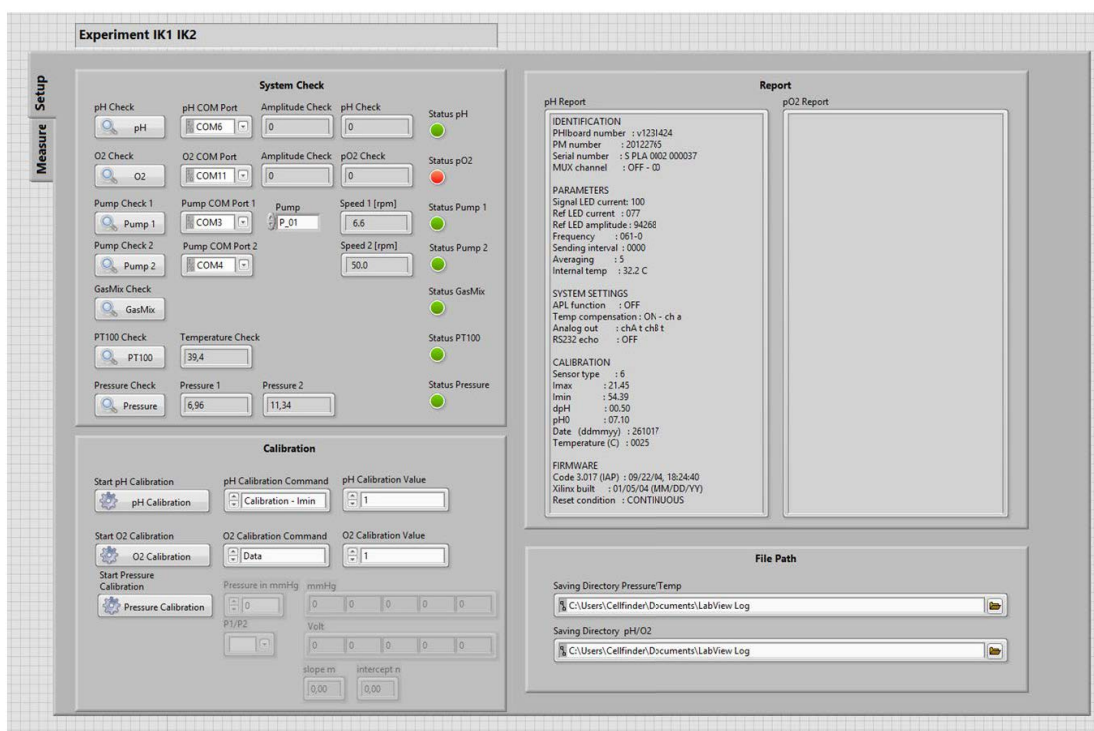


Figure 14: Setup of the perfusion bioreactor. (A) The bioreactor is installed in an incubator. (B) The fully assembled and running system. The peristaltic pump pumps the medium from the bioreactor through the oxygenator and the flow through sensors back into the kidney inside the bioreactor. (C) The bioreactor harbors the cannulated, decellularized kidney. The PT100 temperature sensor is located close to the bioreactor. (D) A more detailed view of the seeding port, the flow through pressure dome connected to the pressure transducer and the optical flow through pH sensor connected to the optical fiber of the fiber optic pH transmitter, from left to right. (E) A detailed view of the oxygenator with medium perfused silicone tubing and the gas humidifier in the back. (F) The fiber optic oxygen transmitter, the fiber optic pH transmitter and the amplifier of the pressure transducer. (G) The PT100, pressure sensor amplifiers and incubator are connected via a cDAQ system to the PC. (H) The gas mixing device mixes CO₂ and air and gasses the oxygenator.

4.1.2 Software development for the control of the perfusion bioreactor

The control software allows full control of the perfusion bioreactor. After software start the user is asked to enter the experiment title. Thereafter the first user interface opens, the setup tab (Figure 15A). Here, the system check can be followed by the user. The software establishes the communication with all connected devices, namely the pH sensor, oxygen sensor, temperature sensor, pressure sensor, peristaltic pumps and the gas mixing device. Successful establishment of the connections is visualized by green indicators and for the pH and oxygen sensors by displaying system status reports from the connected hardware (see Figure 15A). In case the connection cannot be established, the software flashes red indicators, and offers the possibility to change the communication (COM) port settings, as demonstrated in Figure 15A for the oxygen sensor. The setup tab also includes the functions for calibrating the pH, oxygen and pressure sensors. Oxygen and pH sensors are disposables and each new batch of sensors requires updating of the calibration with the calibration data provided by the supplier. For the calibration of the pressure sensor, the user is requested to apply five defined pressures to the sensor and the software records the resulting voltage signals from the sensor, calculates a regression line and saves these calibration data in a calibration file. The user can set the path to the directory where the calibration file is saved. Once the system check is complete the user can change to the measurement tab and start the measurement by pressing the start button (Figure 15B). By ticking the according boxes, the user can choose which parameters will be measured and saved. Moreover, the intervals in which pressure and pH are measured can be set independently. The pH does not fluctuate in a matter of seconds like the pressure. Therefore, it is not necessary to measure the pH in the same interval as the pressure. Furthermore, the pH measurement works with an optical sensor that drifts if too often illuminated. The measured values are displayed numerically and graphically. The measurement tab also contains the control interface. The user can decide between manual and automatic control of pressure and pH. In the manual control mode, the user directly adjusts the control variables (CV) pump speed or CO₂ percentage and total gas flow. In the automatic control mode, the user defines setpoints for the process variables (PV) pressure and pH, and the system adjust the control variables accordingly. All variables, settings and measurement data are saved in an excel file. Additionally, the software allows to write comments into that file, e.g. “medium change”. Errors in the soft- and hardware are displayed. The software can be stopped immediately by a button or after a given time by a timer.

A



B

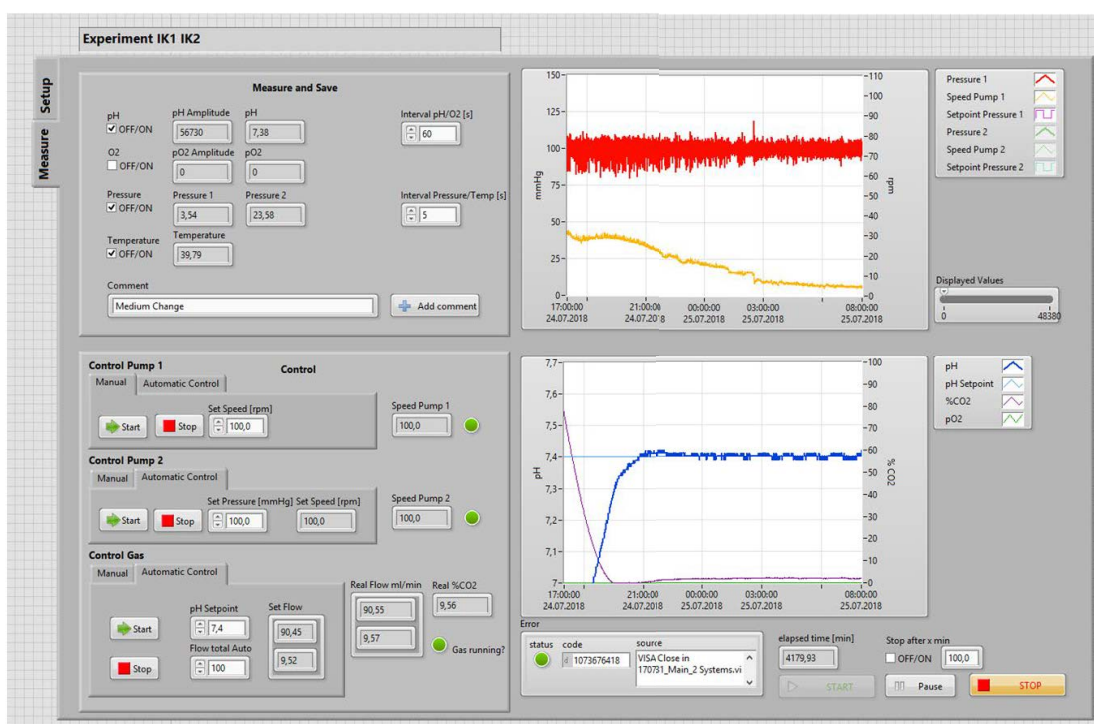


Figure 15: User interface of the control software for the perfusion bioreactor. (A) After starting the software, the Setup-tab opens. The system runs through an initializing procedure. The user can adjust COM ports and file paths and calibrate the sensors. A successful system check is indicated by green indicators and appearing reports. (B) The measurement can be started on the Measure-tab. The user can choose if pH, oxygen, pressure and temperature will be measured and at which interval. These data are displayed in the charts on the right side that additionally also display the data for pump speed and CO₂. All data are also saved as excel sheets. In the control area the user can set the perfusion speed manually or set a pressure setpoint in the automatic control tab. The gas composition for the membrane oxygenator can also be set manually, or automatically by defining a pH setpoint. System errors are displayed, and the software can be stopped manually or by a timer after a given time.

The software was written in LabVIEW. The code was structured as a queued state machine. A state machine is optimal for preprogrammed sequential processes but fails when user input is required. A producer consumer architecture on the other hand is the adequate structure for handling user interface events but fails at preprogrammed sequential tasks. The queued state machine combines these two architectures. It follows preprogrammed sequences like a state machine, but user inputs can interrupt the state machine at any time and insert more important tasks into the workflow. The workflow is managed by a queue. Tasks can be added to the front or end of the queue, depending on their importance.

The perfusion bioreactor control software runs two sequential processes in parallel. One producer loop feeds the queues of two consumer loops that work as independent state machines. Consumer loop 1 handles the pump and pressure control. Consumer loop 2 handles the gas and pH control. Implementing the process in two consumer loops enables the pH and pressure measurement at different intervals, as described earlier.

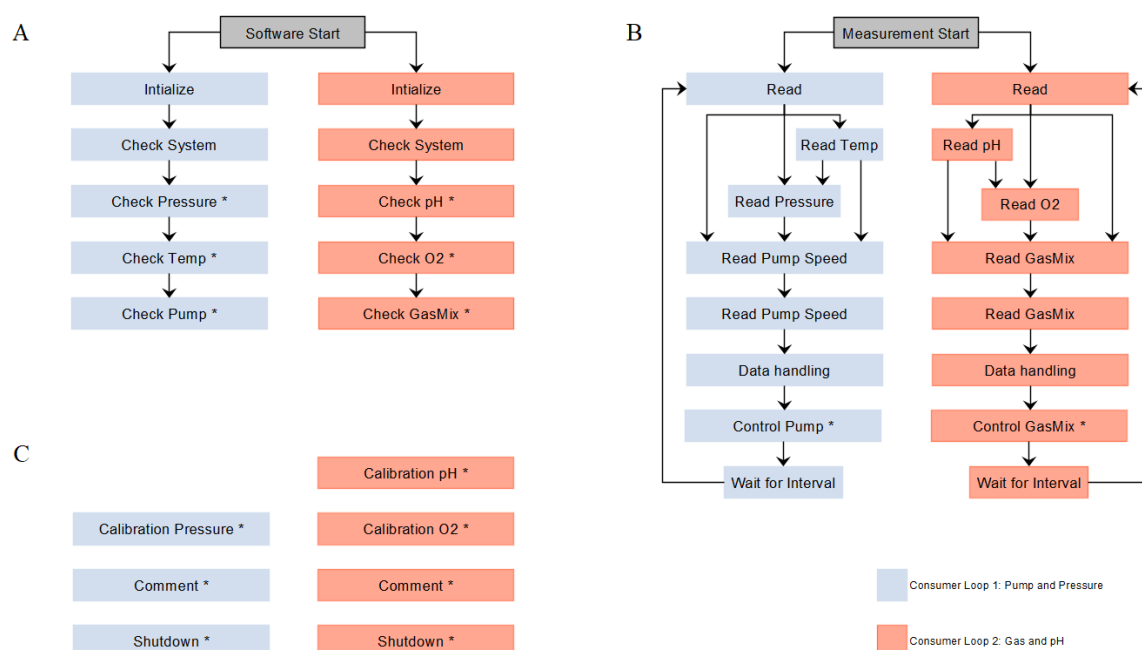


Figure 16: Architecture of the control software for the perfusion bioreactor. The software is programmed as a queued state machine. Two producer consumer structures run in parallel. Consumer loop 1 handles the pump and pressure control. Consumer loop 2 handles the gas and pH control. (A) Initialization sequence. After software start, an initializing sequence is started in which 5 states that initialize and check the system are executed. Thereafter, the software is ready to start the measurement. (B) Measurement sequence. The parameters pressure, temperature, pump speed, pH, O₂ and oxygenation gas composition are read, according to the user's selection. The data handling state saves and plots the data and hands them to the control state in which either the automated controller or manual control settings are executed. A new measurement cycle is started after the interval has elapsed. (C) Additional states that are solely activated by user input. * indicates states that can be called independently.

After software start, the state machine enters the initializing state that establishes the connection between the hardware and the control software via the VISA and DAQmx functions of LabVIEW, resets variables, and creates the excel sheet for saving the measured data. The initializing state directly calls the check system state that then calls the check pressure, temperature and pump or the check pH, O₂ and GasMix states, depending on the consumer loop. These states test the connection to these hardware components by reading out data. No further state is executed automatically thereafter (Figure 16A).

A user input, pressing the start button, is necessary to start the preprogrammed measurement process (Figure 16B). The read state is executed first. It calls read temperature, pressure and pump speed, or read pH, O₂ and GasMix data, depending on the consumer loop and the user's selection. Thereafter, the data handling states are executed. Data are bundled, saved in excel sheets and displayed on the user interface. Subsequently, the control states are called. The pump and gas mixing device can either be controlled manually or the software determines the error between the process variable and setpoint and adjusts the control variable automatically (Table 24). Next, the software enters the wait state and pauses until the set interval has elapsed. Then the measurement process is started from the beginning.

Using the advantage of the queued state machine, states that are part of the state machine and additional states can be called independently from the preprogrammed measurement process (Figure 16C). For example, the shutdown state can be called anytime to stop the software.

4.1.3 Tuning the controllers of the perfusion bioreactor

4.1.3.1 Tuning of the pressure controller

Pressure control in the perfusion bioreactor works via pump speed regulation. The de- or recellularization processes are subject to the impact of disturbances, for example a clogged vessel in the kidney, or an accidentally closed valve in the perfusion bioreactor. Therefore, the process pressure has to be constantly compared to the pressure setpoint. In case of a deviation, the resulting control error (E) is translated by the controller into a control variable change. The pump speed is adjusted until the pressure setpoint is met (Figure 17).

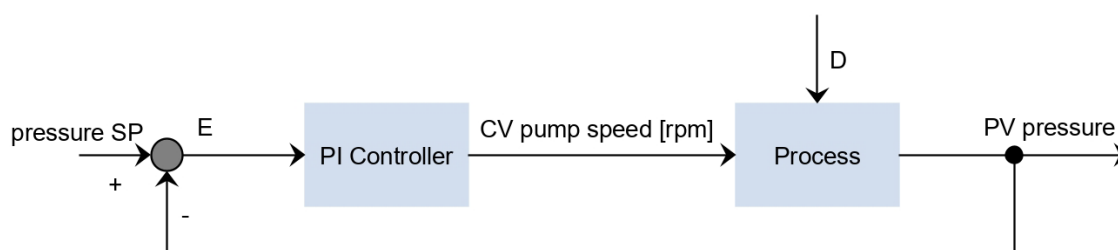


Figure 17: Block diagram of the pressure feedback loop. The process variable (PV), the actual pressure in the system, is compared with the pressure setpoint (SP). The control error (E) is used by the controller to adjust the control variable (CV), the pump speed. The process, the perfusion bioreactor, reacts to the new pump speed and the resulting pressure is again sent as a feedback to the controller. Disturbances (D) can influence the pressure and have to be compensated by an appropriate controller reaction.

To ensure an accurate reaction of the controller, the controller had to be specifically tuned for this process. First, the process was characterized by recording a step response. The CV pump speed was changed, and the response of the PV pressure was recorded. Since decellularized kidneys are a biological material that naturally shows high variability, the step response was recorded for three kidneys. Figure 18 shows that every kidney reacted differently to the pump speed change. All three step responses classified the process as a first-order system (PT_1 element). That means the pressure reacts to the pump speed change without any dead time, but the process variable reaches the new steady state with a delay. The speed of the PV change reaches its maximum right after CV change and decreases thereafter. PT_1 elements are characterized by two parameters, the time constant T and the proportional action coefficient K_s .

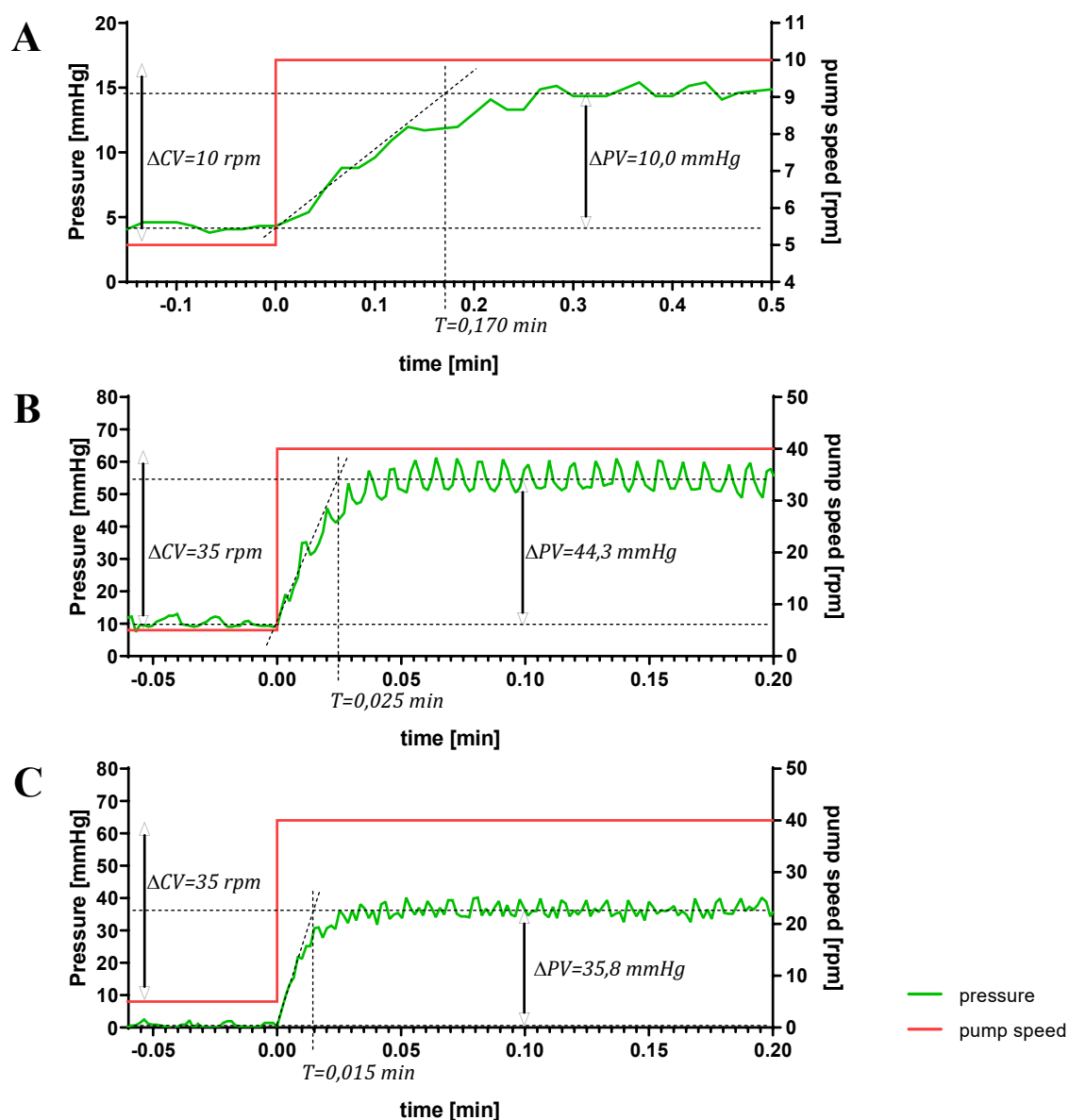


Figure 18: Step response to pump speed change. The control variable pump speed (CV) was changed while the response of the process variable pressure (PV) was recorded for three different kidneys (A,B,C). The step response categorized the system as a PT1 element. The time constant and proportional action coefficient varied for every kidney.

The intersection of the tangent at the steepest part of the PV curve and the final PV value defines the process time constant. The time constant is a measure for the speed in which the process reacts to the CV change. Every tested kidney reacted with a characteristic time constant T :

$$T_A = 0,170 \text{ min} \quad T_B = 0,025 \text{ min} \quad T_C = 0,015 \text{ min}$$

The proportional action coefficient K_s describes the correlation of PV change after CV change. Again, all three tested kidneys reacted to the CV change with a different K_s :

$$K_{sA} = \frac{\Delta PV_A}{\Delta CV_A} = \frac{10,0 \text{ mmHg}}{5,0 \text{ rpm}} = 2,0 \frac{\text{mmHg}}{\text{rpm}}$$

$$K_{sB} = \frac{\Delta PV_B}{\Delta CV_B} = \frac{44,3 \text{ mmHg}}{35,0 \text{ rpm}} = 1,3 \frac{\text{mmHg}}{\text{rpm}}$$

$$K_{sC} = \frac{\Delta PV_C}{\Delta CV_C} = \frac{35,8 \text{ mmHg}}{35,0 \text{ rpm}} = 1,0 \frac{\text{mmHg}}{\text{rpm}}$$

Since T and K_s were different for every tested kidney, the perfect controller tuning would require the identification of T and K_s for every kidney placed inside the bioreactor. As this is not feasible, a compromise had to be made and universally working tuning parameters had to be identified. Therefore, the mean time constant and the mean proportional action coefficient of the three step responses were calculated:

$$\bar{K}_s = 1,4 \frac{\text{mmHg}}{\text{rpm}} \quad \text{and} \quad \bar{T} = 0,070 \text{ min}$$

These two process characteristic parameters are the basis for the identification of the controller tuning parameters. The PID controller is the most widely used control algorithm. It is defined by three main control effects. The proportional action, P, changes the CV proportional to the control error. The integral action, I, changes the CV proportional to the integrated control error and is applied to eliminate the control offset. Lastly, the derivative action, D, changes the CV proportional to the derivative of the control error. D speeds up the response but is less commonly used. The PID controller output is the sum of these three terms. The corresponding adjustable PID tuning parameters are the proportional gain K_p , the integral time T_i and the derivative time T_d ¹⁴⁶. The process characteristic parameters K_s and T were translated into the controller tuning parameters K_p , T_i and T_d by applying the T-sum tuning rule, also called KUHN tuning method¹⁴⁷, which is displayed in Table 25.

Table 25: Tuning methods used for adjusting the pressure and pH controller¹⁴⁷

Controller		K_p	T_i	T_d
PID	KUHN	$\frac{2}{K_s}$	$0,8T$	$0,194T$
PI	KUHN	$\frac{1}{K_s}$	$0,7T$	

The tuning parameters for the PID controller are:

$$K_p = 1,4 \quad T_i = 0,056 \quad T_d = 0,014$$

The tuning parameters for the PI controller are:

$$K_p = 0,7 \quad T_i = 0,049$$

Additionally, a setting for a slow PI controller was selected manually:

$$K_p = 0,05 \quad T_i = 0,05$$

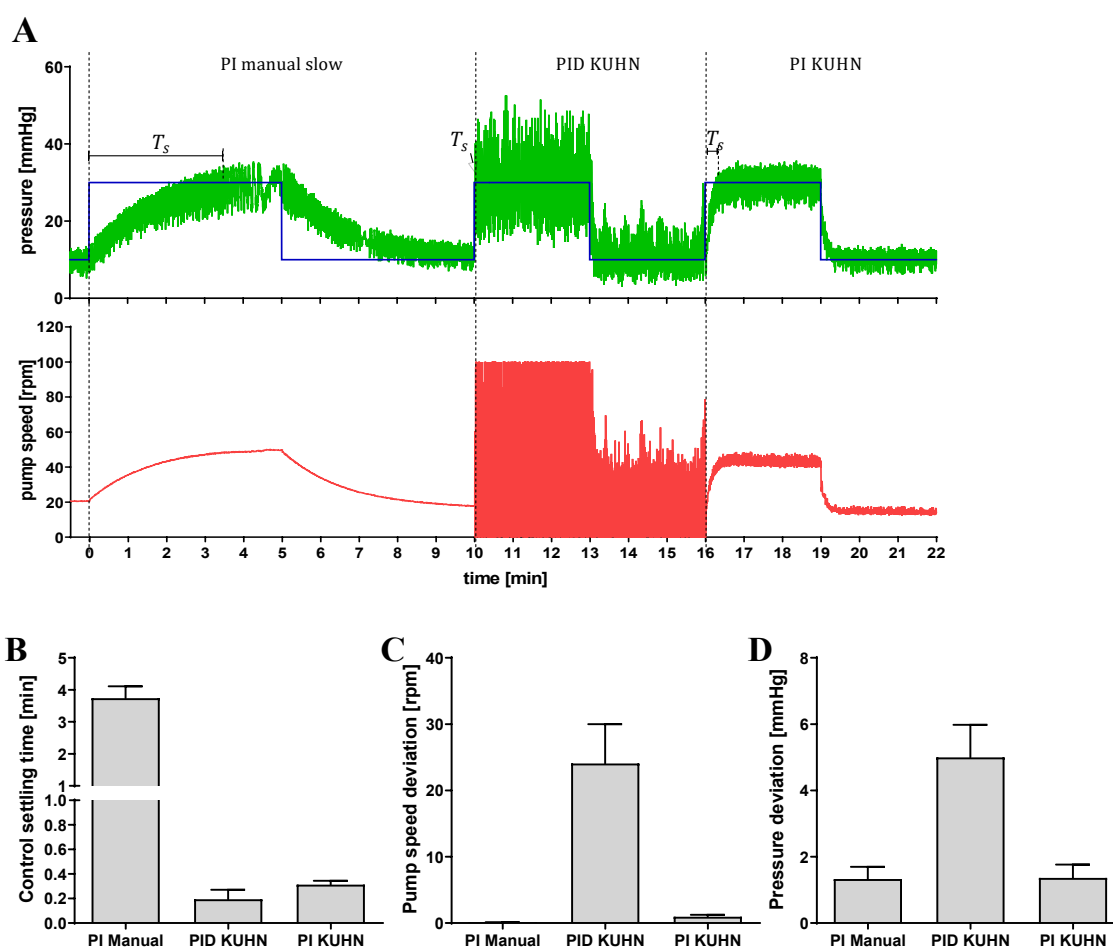


Figure 19: Reference-variable response of the control system. (A) The reaction to a pressure setpoint change of a manually tuned, slow PI, PI KUHN and PID KUHN controller were recorded. The manually tuned controller reacts slow but stable, the system is overdamped. The PID controller reacts very fast but leads to high deviations in pump speed and pressure, the system is underdamped. The PI KUHN controller reacts fast and results in a stable process, the system is critically damped. (B) The control settling time, (C) the average absolute deviation from the mean pump speed and (D) the average absolute deviation from the mean pressure were identified from the responses.

These controller settings were tested in a reference-variable response. The pressure setpoint was changed from 10 to 30 mmHg. The pump speed change by the controller and the response of the process pressure were recorded (Figure 19A). The control settling time T_s describes the time required by the controller to adjust the PV to the new setpoint. The higher the tuning parameters are, the faster reacts the controller. The PID KUHN controller therefore has the shortest T_s with 0,2 min. The PI KUHN controller requires 0,3 min, only slightly longer. The manually tuned PI controller needs nearly 4 min (Figure 19B). However, the PID controller constantly changes the pump speed in a very wide range, whereas the manual PI and the PI KUHN controllers have way less fluctuation in the CV. Therefore, the absolute deviation from the mean pump speed is much higher in the PID controller (Figure 19C). Hence, the pressure oscillates much more around the setpoint in the PID controlled system (Figure 19D). The manual PI controller results in an overdamped system and the PID KUHN controller in an underdamped system. The PI KUHN controller results in a critically damped system, it is fast and stable. Therefore, this is the preferred controller tuning for stable yet fast pressure control.

Next, the PI KUHN tuned system was tested on how it reacts to a disturbance. Therefore, the valve that is used as the seeding port was closed to simulate a clogged vessel (Figure 20). The pressure in the system rises immediately from 20 to 100 mmHg. The PI controller required only 0,6 s to stop the pump completely. This reaction will prevent damage to the recellularized kidney due to too high perfusion pressures. When the valve was reopened the pressure was released and the pump started again.

In conclusion, the PI KUHN controller handles the pressure control satisfactory.

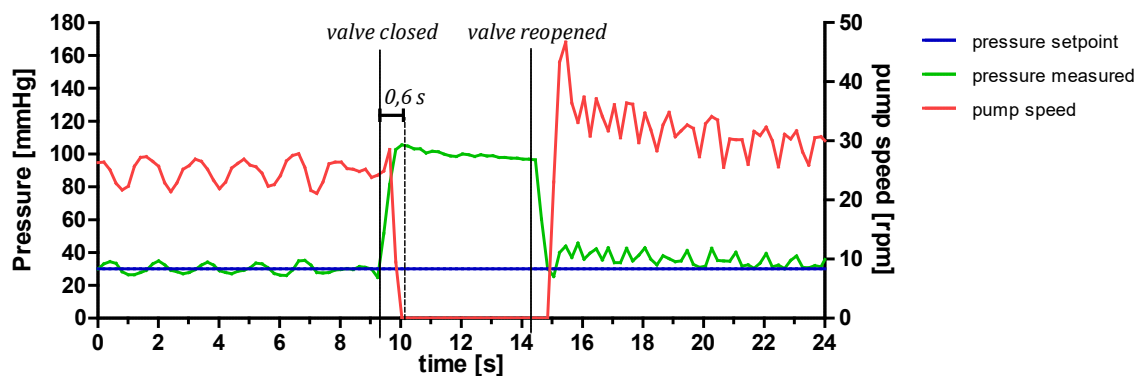


Figure 20: Disturbance response of the pressure control system. The PI KUHN controller stops the pump 0,6 s after the pressure rises due to a closed valve in the perfusion bioreactor.

4.1.3.2 Tuning of the pH controller

The pH is a critical factor for cell culture. A physiological pH of 7,4 has to be maintained in the cell culture medium for optimal cell viability. In most cell culture media a bicarbonate buffer system permits the control of the pH by adjusting the CO₂ concentration in the medium. However, fixing the CO₂ concentration at 5%, as it is applied in standard cell culture incubators, cannot compensate for any disturbances, such as lactic acid that is secreted by viable cells and lowers the pH of the cell culture medium. To stabilize the pH at a constant physiological level during the recellularization culture, a pH controller was implemented. The percentage of CO₂ used for gassing the medium is the control variable of this process control system (Figure 21).

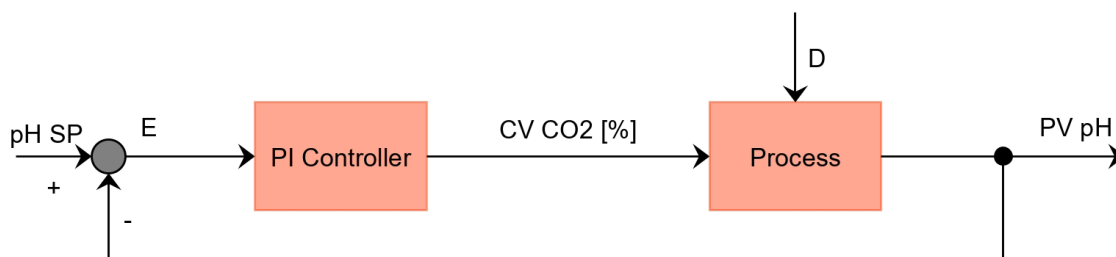


Figure 21: Block diagram of the pH feedback loop. The process variable (PV), the actual pH in the system, is compared with the pH setpoint (SP). The control error (E) is used by the controller to adjust the control variable (CV), the CO₂ content in the gas that flows through the membrane oxygenator. The process, the perfusion bioreactor, reacts to the new CO₂ content and the resulting pH is again sent as a feedback to the controller. Thereby pH disturbances (D) can be compensated.

To identify the optimal controller setting, the process was characterized by a step response first (Figure 22). Therefore, the CO₂ percentage in the gas mixture that flows through the oxygenator was changed from 0 to 10%, and the change of the pH was recorded. The pH decreased by 0,61 with increasing CO₂ concentration. The step response characterized the process as a second-order system (PT₂ element). PT₂ elements are defined by a delayed reaction of the PV to the CV change. In contrast to PT₁ elements the speed of the PV change is not highest immediately after the CV change. Instead it rises slowly, reaches the maximum in an inflection point and declines until the PV reaches its new steady state. The intersection of the tangent at the inflection point and the starting PV value defines the process dead time $T_u=8,9$ min. The intersection of the tangent at the inflection point and the final PV value defines the process time constant $T_g=8,6$ min. The tangent at the inflection point simplifies the process to a PT₀T₁ element, a PT₁ element with dead time.

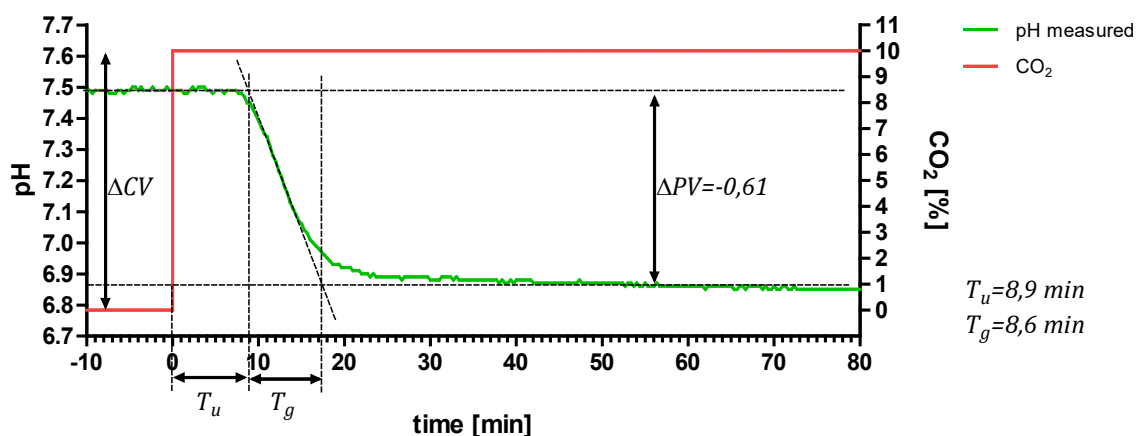


Figure 22: Step response to CO₂ change. The control variable CO₂ [%] (CV) was set from 0 to 10% while recording the response of the process variable pH (PV). The step response categorized the system as a PT₂ element.

The controllability of a PT₂ process is defined by the ratio:

$$\frac{T_g}{T_u} = \frac{8,6 \text{ min}}{8,9 \text{ min}} = 0,96$$

Ratios smaller than 3 define systems that are hard to control due to the high dead time. Ratios higher than 10 define systems with a good controllability. The pH in the perfusion bioreactor is therefore a process variable that is difficult to control.

The time constant of the system is the sum:

$$T = T_u + T_g = 17,5 \text{ min}$$

The proportional action coefficient of the controlled system results from:

$$K_S = \frac{\Delta PV}{\Delta CV} = \frac{6,88 - 7,49}{10,0\% - 0,0\%} = -0,06 / \% \text{ CO}_2$$

By applying the tuning rules of KUHN, which are displayed in Table 25, the resulting tuning parameters for the PID controller are:

$$K_P = -32,8 \quad T_i = 14,0 \quad T_d = 3,4$$

The tuning parameters for the PI controller are:

$$K_P = -16,4 \quad T_i = 12,3$$

Both settings were tested in the perfusion bioreactor in a reference-variable response, as shown in Figure 23. The pH setpoint was changed from 7,4 to 7,2 and back and the responses of the CV and PV were recorded. The PI controller reacted fast and adjusted the CV without much fluctuation. The setpoint was reached without PV offset or oscillation. However, due to its poor controllability the new setpoint was only met after 74 min. The PID algorithm was 7 min faster than the PI algorithm and the PV reached the new setpoint without any constant offset. However, the CV was fluctuating more, and the PV oscillated around the setpoint. Therefore, the PID settings did not control the pH stably. Hence, the PI algorithm is more suitable for pH control in the perfusion bioreactor.

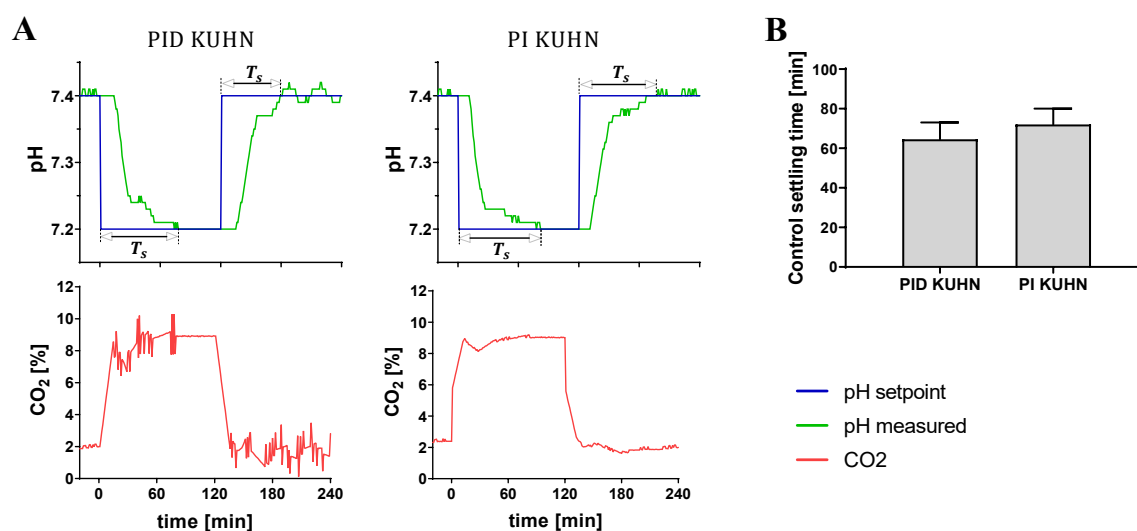


Figure 23: Reference-variable response of the pH control system. (A) The reference-variable response to a setpoint change was recorded for PI and PID controllers tuned by the KUHN method. Both controllers adjusted the PV to the new setpoint, but the PID controller showed a higher fluctuation in the CV and the PV oscillated around the setpoint; whereas the PI algorithm controlled the pH more stably. (B) The PID controller achieved a shorter control settling time.

Next, the tuned PI controller was tested for its reaction to a disturbance in the process. Here a change in the pH was provoked by adding 300 mg citrate or NaOH into the medium of the bioreactor. Citrate reduced the pH to 7,23. The system required 55 min to restore the pH to the setpoint of 7,30. Although an overshoot was not observed in any of the reference-variable responses, here a small overshoot had to be compensated. The system reached the pH setpoint after a further 73 min. NaOH increased the pH to 7,58. The controller restored the pH to 7,40 after 59 min. However, the overshoot was bigger than in the citrate disturbance and the system needed 102 min more to fully compensate the disturbance (Figure 24). The

overshoot was most likely generated by a longer dead time than in the step and reference-variable responses. In these experiments the dead time was shorter because only the time that the medium needed to be pumped from the membrane oxygenator to the pH sensor influenced the dead time. Here, the time that the medium needed from the bioreactor to the membrane oxygenator is added to the total dead time. Therefore, the pH controller calculated with a lower integral time T_i , than required, leading to higher integral action and a too rapid controller reaction in the disturbance response. This proves again the bad controllability of this process. By increasing T_i the overshoot could be decreased. However, metabolite secretion during perfusion culture only changes the pH gradually, not as fast and profound as it was provoked in the disturbance response. Additionally, varying pump speeds during the perfusion culture also influence the pH control. Due to these possible variations and the bad controllability no perfect tuning parameters for the pH controller will be identified. Nevertheless, the identified parameters are satisfactory for most scenarios.

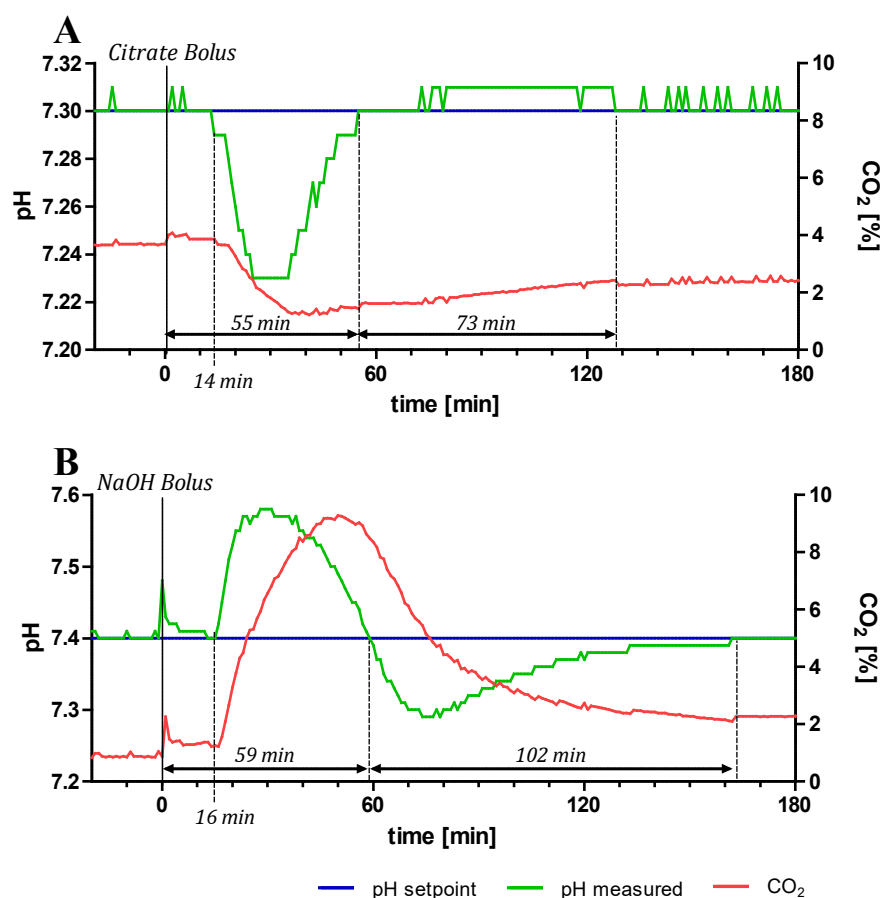


Figure 24: Disturbance response of the pH control system. (A) 300 mg citrate or (B) NaOH were added to 50 ml cell culture medium in the bioreactor. The response of the pH control system was recorded. Both disturbances provoke an overshoot. The pH is fully restored to the setpoint after 2 to 3 h.

4.2 Identification of an optimal decellularization strategy for kidney tissue using factor screening in an immersion and agitation setting

Decellularization is a procedure in which cells of an organ or tissue are removed while the ECM remains. This is achieved by chemical and physical treatments that lyse the cells and solubilize and remove cell debris. In a process called recellularization the decellularized tissue is used as a scaffold and reseeded with cells. To achieve a successful recellularization the scaffold has to be of high quality. Ideally, the cellular material should be removed completely, and the ECM should stay in its native state. Therefore, the identification of a decellularization protocol that balances these two criteria is of utmost importance. Decellularization of tissue cubes by immersion and agitation offers the opportunity to test many different protocols in parallel in a factor screening approach.

Here, cubes from porcine kidneys were treated by immersion and agitation in different detergents, namely 1% SDC, 1% SDS or 1% TX-100, and at different temperatures, either 4 °C, RT (22-24 °C) or 37 °C, to investigate which decellularization strategy produces scaffolds in top quality for recellularization. It was hypothesized that less harsh detergents and lower temperatures would better preserve the ECM. To that end, cell removal, ECM composition and biocompatibility were investigated after decellularization (Figure 25).

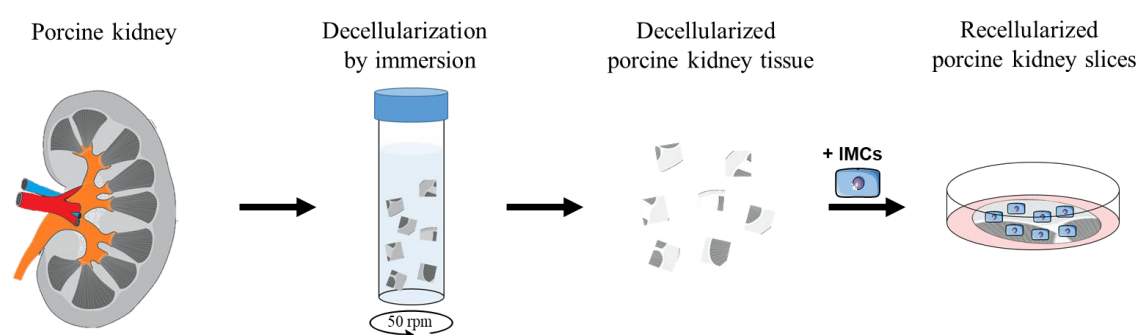


Figure 25: The experimental process of the de- and recellularization of porcine kidneys by immersion and agitation. Porcine kidney cubes were decellularized by immersion and agitation in SDC, SDS or TX-100 at 4 °C, RT or 37 °C. Sections of the decellularized cubes were recellularized with hiPSC-derived intermediate mesoderm cells (IMCs) under static culture conditions to investigate the scaffold's biocompatibility.

4.2.1 Analysis of histology and composition after decellularization by immersion and agitation

Upon decellularization the macroscopic appearance of the kidney cubes changed from brown to milky yellow and finally to white and transparent indicating the increasing cell removal. Differences in the decellularization efficacy were reproducibly observed between the different temperatures and detergents.

SDC treated tissues became most transparent at 4 °C (Figure 26), and remained milky at RT and 37 °C. Hematoxylin and eosin (HE) staining of paraffin sections confirmed that the most effective, although still incomplete, removal of cell components was achieved at 4 °C, while RT and 37 °C samples showed substantial amounts of cellular residues, especially in the core of the immersed tissue cube. Thus, SDC poorly penetrates the center of the cubes. DAPI staining, which labels double stranded DNA (dsDNA), confirmed the absence of intact nuclear structures, but cellular debris and parts of the scaffold were stained with DAPI, especially in the 4°C and RT samples. Thus, dsDNA fragments are still present in the debris or adhere to the ECM. Interestingly, the intensity of the DAPI stain does not correlate with the remaining cellular material. Although there is more cellular material left in the 37 °C samples, less DAPI staining is detected than in the 4 °C sample. Immunofluorescence staining of the ECM components laminin, collagen IV and fibronectin showed their preservation at all temperatures. Compared to native tissue, merely tubular laminin is reduced, whereas it is preserved in the glomeruli.

Kidney tissue treated with SDS shrank about 10% - 20% in volume. 4 °C and RT samples appeared translucent, whereas the 37 °C samples were still yellow after decellularization (Figure 27). HE staining proved the complete decellularization of 4 °C and RT samples, but only the 4 °C sample had a well-preserved architecture, whereas the RT sample showed zones of collapsed glomeruli and tubules. Histology confirmed also the incomplete decellularization of the 37 °C sample as they contained cellular debris, which was also confirmed by DAPI staining. Comparable to the SDC samples, and all stained ECM proteins were well preserved apart from tubular laminins. The nephron architecture was not impaired. After decellularization with TX-100, all treated tissue cubes appeared macroscopically yellow/whitish regardless of the applied temperature (Figure 28). HE and DAPI staining revealed intact nuclei throughout the cube, especially in the 37 °C sample. Cytoplasmic components were only marginally reduced in comparison to native tissue. The architecture and ECM proteins laminin, collagen IV and fibronectin are undamaged, as shown by

immunofluorescent analysis. Therefore, TX-100 alone is not able to break up the majority of cells and to separate them from the ECM.

In summary, SDS at 4 °C performed best regarding cell and dsDNA removal. SDC at 4 °C also clears the tissue of most of the cellular material, however, zones exist where cellular debris and dsDNA are still present. Therefore, a DNase digest was added after detergent treatment. TX-100 insufficiently decellularized the kidney tissue.

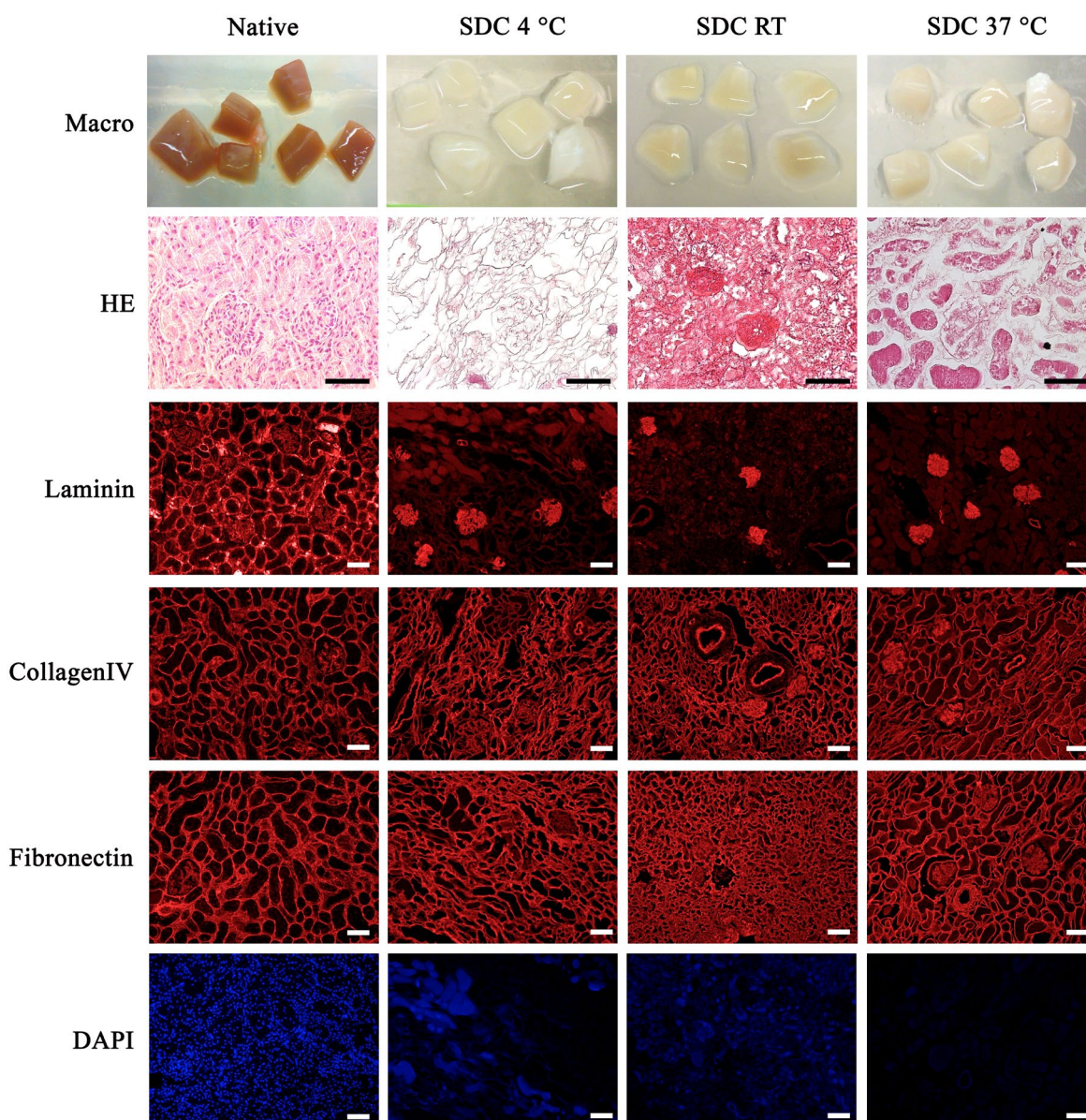


Figure 26: Macroscopic and histological analysis of native and SDC-decellularized porcine kidney cubes at 4 °C, RT and 37 °C. Native porcine kidneys appeared brown. Native vessels, tubules and glomeruli are filled with epithelial and endothelial cells, as shown by HE and DAPI staining. The ECM molecules laminin, collagen IV and fibronectin were detected in the ECM lining the tubules and blood vessels. SDC at 4 °C gave the best results. At RT and 37 °C, SDC showed poor penetration into the center of the cubes, which were not completely decellularized. DAPI-stained dsDNA was detected in zones filled with cellular debris and on the ECM. Only laminin staining was reduced in the tubules. The architecture was preserved. Scale bar: 50 μ m.

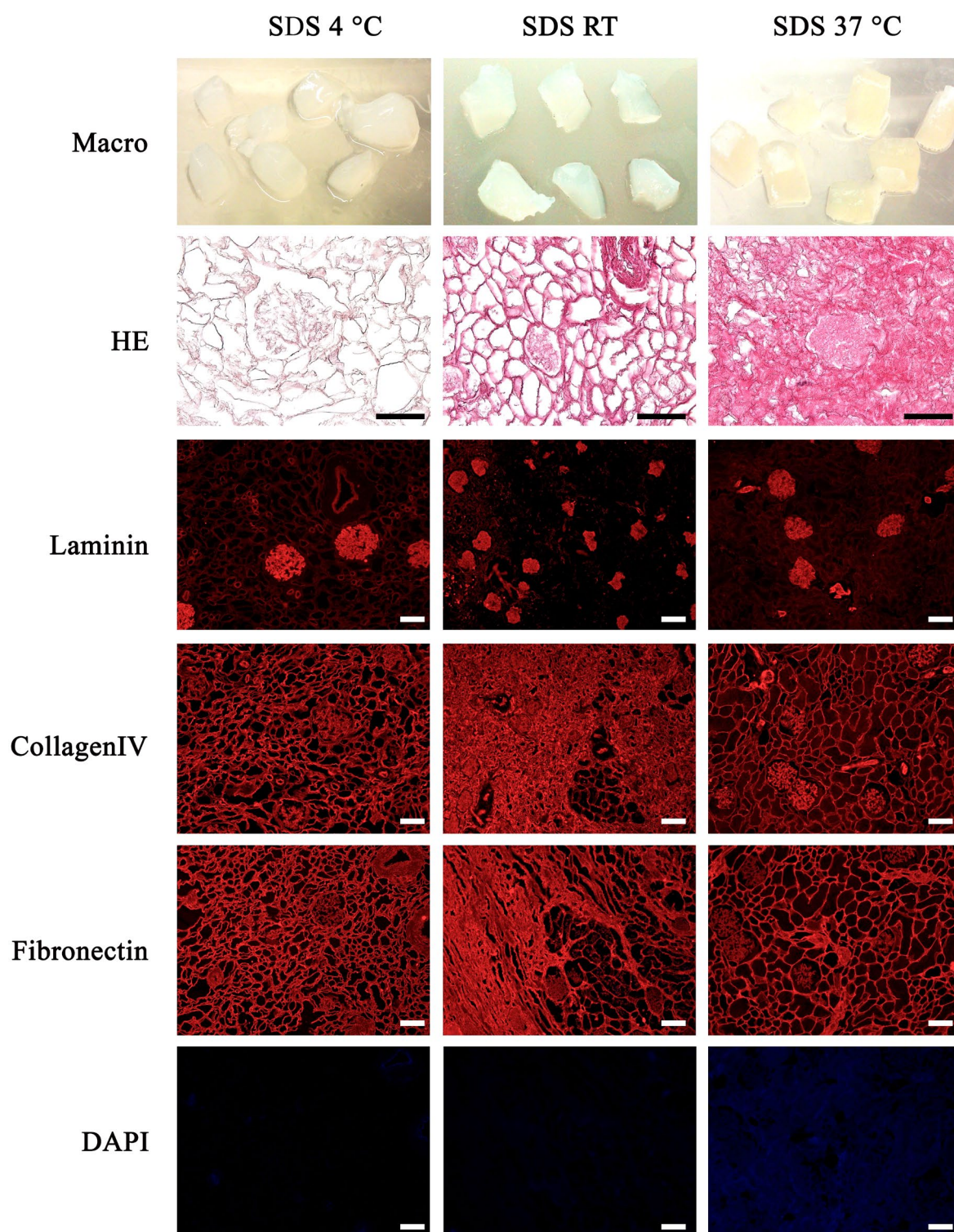


Figure 27: Macroscopic and histological analysis of SDS-decellularized porcine kidney cubes at 4 °C, RT and 37 °C. SDS-decellularization at 4 °C and RT resulted in translucent tissue. The cubes shrank during decellularization. Neither HE-stained cell debris, nor DAPI-stained dsDNA was detected. At RT, wide areas of the architecture were collapsed. Decellularization at 37 °C was incomplete, since dsDNA and cellular material were detected. Only laminin staining was reduced in the tubules. Scale bar: 50 μ m.

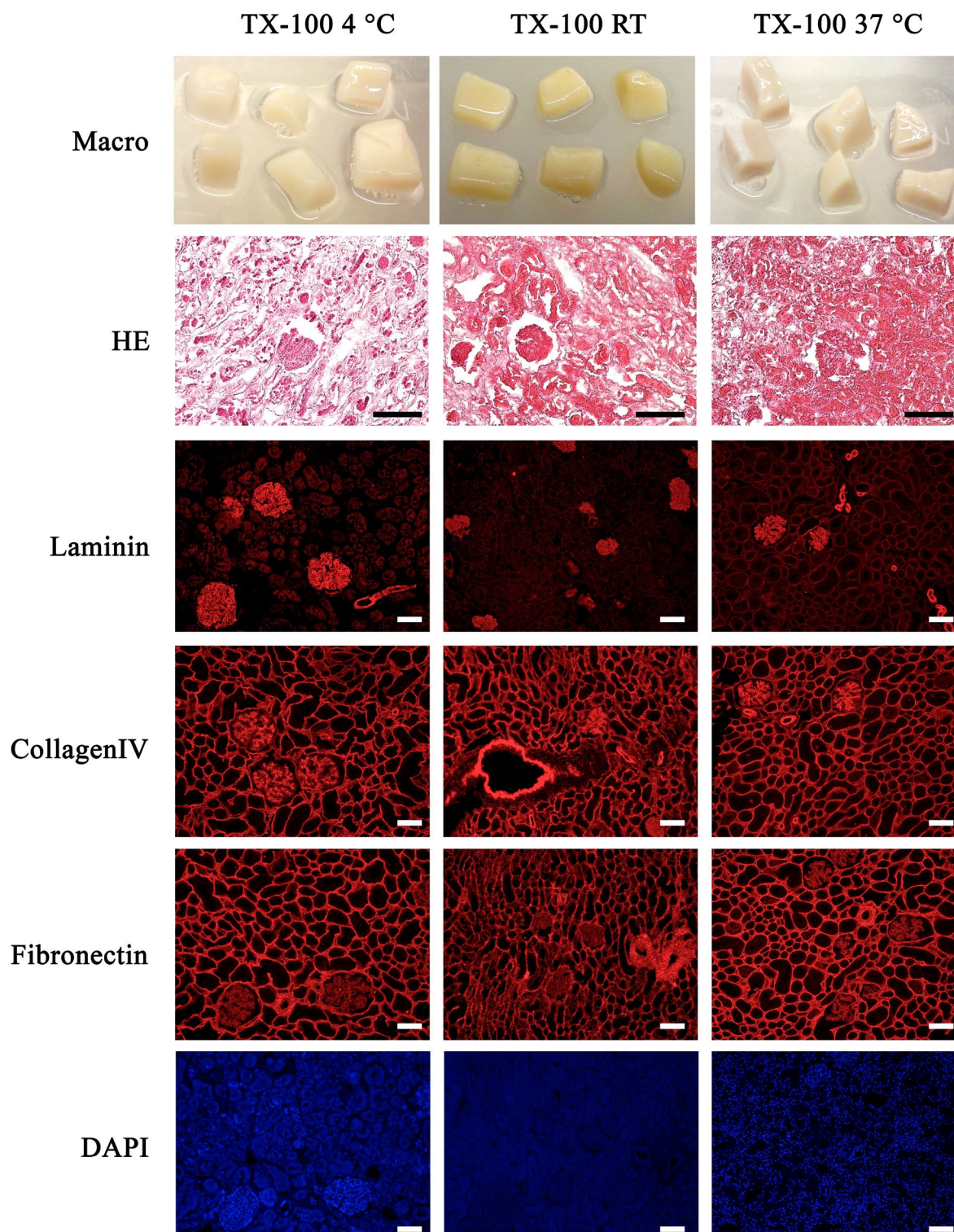


Figure 28: Macroscopic and histological analysis of TX-100-decellularized porcine kidney cubes at 4 °C, RT and 37 °C. No decellularization condition using TX-100 yielded in fully decellularized scaffolds. The higher the applied temperature the more cellular debris remained, corroborated by strong DAPI signals. Tissue cubes therefore appeared milky white. Scale bar: 50 μ m.

To further quantify the maintenance of critical ECM components after decellularization, total collagen, GAG, VEGF and bFGF were quantified (Figure 29). In addition, remaining DNA was analyzed, as an indicator for cell removal. The TX-100 group was omitted from these analyses as the histological analysis already revealed poor decellularization and DNA removal (Figure 28). All amounts were normalized to the dry weight after decellularization. Quantification of total DNA after DNase treatment in the SDC and SDS groups showed that DNA was efficiently removed from the tissue in all conditions (Figure 29A), even in the SDC 4 °C samples that showed residual DNA in the DAPI stain before DNase treatment.

The highest collagen/ dry weight ratios were measured after decellularization for both detergents at 4 °C, whereas the lowest ratios were measured in the 37 °C samples. Generally, higher collagen/ dry weight ratios were measured in SDS treated samples than in SDC treated samples when comparing the individual temperatures, although these differences are not significant. Therefore, the samples with poorer removal of cellular material retained more non-collagenous structural and cytoplasmic components (Figure 29A, D, E). This resulted in a lower relative amount of collagen per total mass, even if the absolute amount might be similar.

In contrast to collagens, GAG maintenance in decellularized tissues was not influenced by the temperature, hence there was no correlation between decellularization efficacy and GAG levels (Figure 29C). Strikingly, there was a significantly lower ratio of GAG in SDC-decellularized samples than in SDS-decellularized samples, indicating a profound loss of GAGs during decellularization with SDC, or a superior maintenance of GAGs in SDS-decellularized matrix.

SDC-decellularized samples contained more VEGF and bFGF than SDS-decellularized samples (Figure 29D, E), although both these cytokines have a strong binding affinity to GAG chains in proteoglycans. Therefore, the data suggest that SDC treatment removed more GAG from the ECM but dissociated less GAG-bound cytokines compared to SDS.

Next to the composition, the stiffness is an important property of the ECM. The elastic modulus of native glomeruli and SDC- and SDS-decellularized glomeruli was determined using atomic force microscopy. The native glomeruli and the SDC-decellularized glomeruli showed a comparable *E* modulus of approximately 0,5 kPa. Whereas SDS-decellularized glomeruli were stiffer, having an *E* modulus of 2 kPa. For the comparison it has to be considered, that the samples of native kidney tissue contain cells and had to be frozen for

sample preparation, therefore the E modulus of the native ECM alone could not be measured (Figure 29F).

In summary, DNA was removed efficiently after DNase treatment. Decellularization with SDS at 4 °C yielded the highest collagen/dry weight ratio and second highest GAG/dry weight ratio, whereas preservation of VEGF and bFGF was superior in SDC at 4 °C.

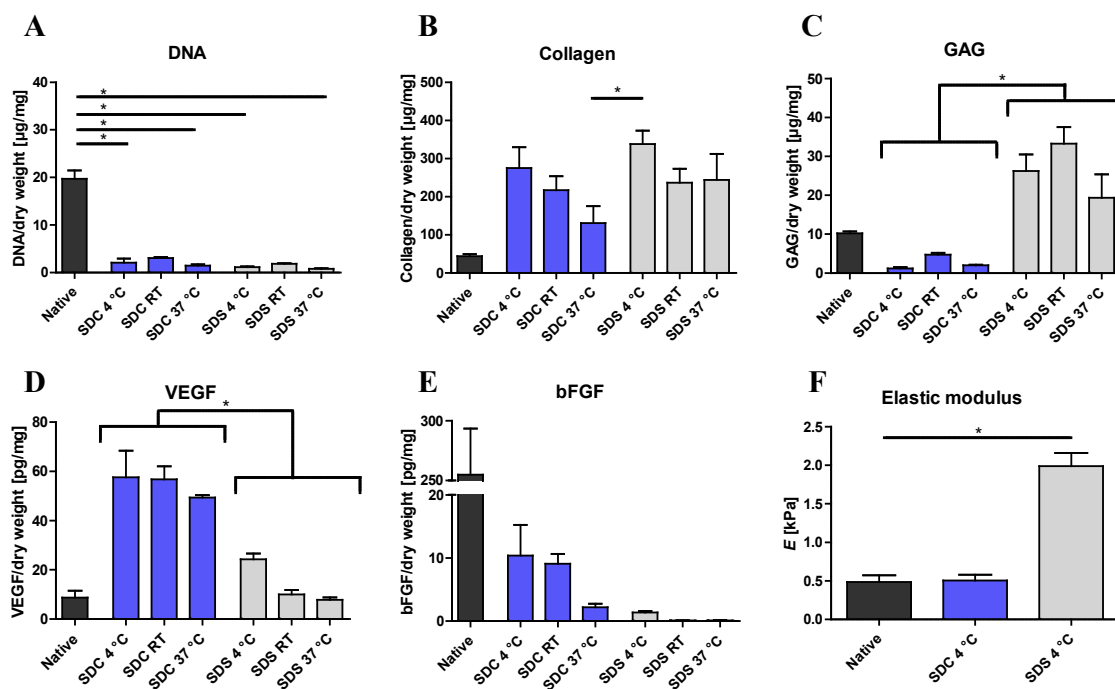


Figure 29: Composition analysis of immersion-decellularized matrices. Quantitative analysis of (A) DNA, (B) total collagen, (C) GAG, (D) VEGF and (E) bFGF content after decellularization by immersion of porcine kidney fragments using the indicated conditions. The specific amounts are given as the ratio of the target substance (in µg or pg) to the dry weight of the sample after decellularization (mg). (F) Atomic force microscopy was used to determine the elastic modulus E of native and decellularized kidney matrix. Values are expressed as mean \pm SEM, * indicates a significant difference in means, $p < 0.05$.

4.2.2 Biocompatibility testing of immersion-decellularized kidney tissue by recellularization with intermediate mesoderm cells

Human iPSC-derived intermediate mesoderm cells (IMCs) were used to examine the biocompatibility of the most promising immersion-decellularized ECM scaffolds. Therefore, cell attachment and viability were analyzed. IMCs give rise to all renal cell types⁸⁹, and are therefore a realistic cell source for kidney recellularization.

The hiPSC-derived IMCs were differentiated in 5,5 days from a constitutive GFP-expressing hiPSC line. GFP expressing hiPSCs were chosen for easier visualization of the cells on the scaffold. The differentiated cell population contained 62.5% LHX1 and 69% PAX2 positive cells, indicative of efficient IMC generation (Figure 30).

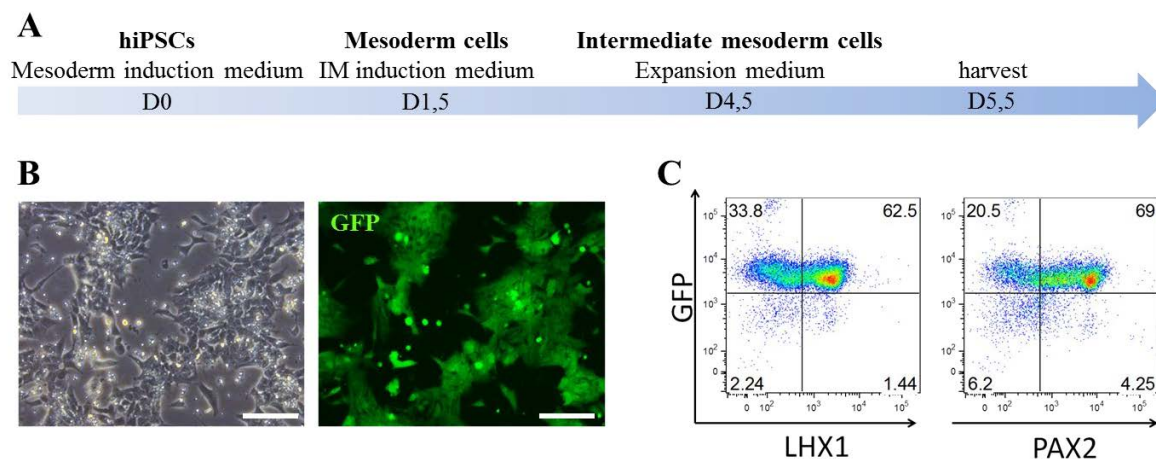


Figure 30: Differentiation scheme of hiPSC-derived intermediate mesoderm cells. (A) Intermediate mesoderm cells were differentiated from the constitutive GFP-expressing hiPSC line WISCi004-B (GFP⁺) in a 5,5-day protocol. (B) Brightfield and fluorescence images show the morphology and GFP-expression of IMCs. Scale bar: 100 μ m (C) Expression of intermediate mesoderm markers LHX1 and PAX2 was shown by flow cytometry in 62% and 69% of the differentiated cells, respectively.

IMCs were seeded on renal ECM, mounted as 50 μ m sections on POMA-coated glass coverslips. The ECM was prepared by immersion-decellularization with SDC or SDS at 4 $^{\circ}$ C, as these conditions gave the best results in the analysis of histology and composition. As controls, TX-100-ECM, glass coverslips and tissue culture treated polystyrene (TCPS) were used.

The coverslips were scanned 30 and 76 h post seeding using the Operetta high content screener. Representative pictures are shown in Figure 31A. Attached cells were morphologically enlarged and integrated into the scaffold, whereas non-attached cells appeared small and round. Higher proportions of IMCs attached on the decellularized renal ECM structures than on the glass or TCPS surfaces. Interestingly, more cells attached on SDC- compared to SDS- or TX-100-treated ECM. These observed trends were quantified with the Harmony High-content imaging software on the entire coverslip scan. The applied image analysis sequence is depicted in Figure S1. The total cell number was set to 100% at each time point. The quantification confirmed the higher attachment of cells over time on renal ECM compared to glass or TCPS and the significantly higher attachment on SDC- than

on SDS-decellularized ECM. The number of attached cells as a fraction of all cells increased over time, hence the percentage of attached IMCs was highest at 76 h, indicating a survival advantage of cells attached to ECM (Figure 31B). Additionally, the metabolic activity measured in the resazurin assay confirmed the observation of the attachment data.

In summary, IMCs attached less effective and were less vital on TX-100-ECM, SDS-ECM, glass or TCPS than on SDC-ECM.

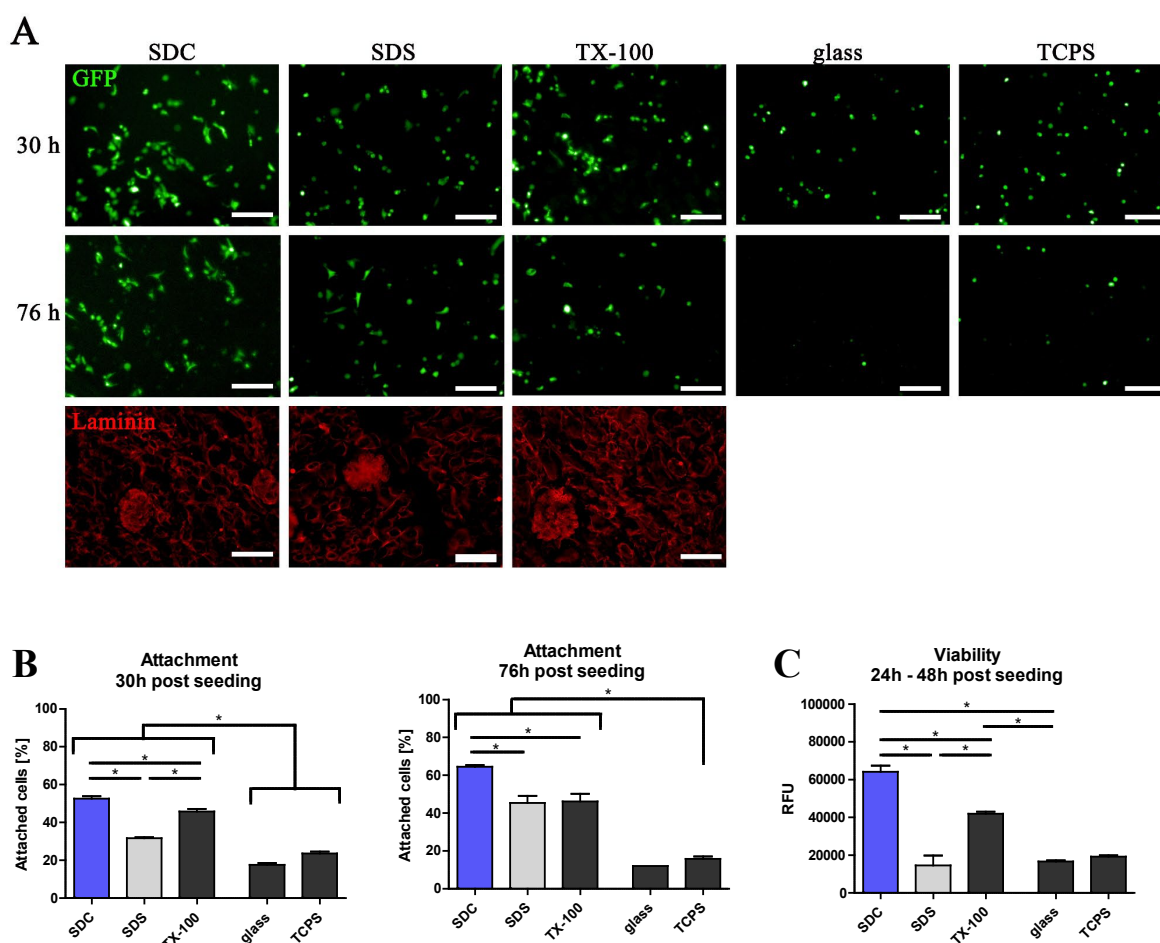


Figure 31: Analysis of IMC viability and attachment on immersion-decellularized kidney sections. 3×10^5 iPSC-derived IMCs cm^{-2} were seeded on 50 μm thick SDS-, SDC- and TX-100-decellularized kidney sections, glass cover slips or tissue culture polystyrene (TCPS). (A) GFP-positive cells were imaged at 30 and 76 h post seeding. The cells attached best on SDC-ECM, indicated by a spread-out morphology; whereas cells attached worse on SDS and TX-100-ECM, indicated by a small, round cell morphology. Laminin staining of decellularized cover slips, performed at the end of the experiment, confirmed persistent maintenance of ECM structures. Scale bar: 100 μm . (B) Attached and non-attached GFP-positive cells were counted at 30 and 76 h post seeding and the total cell number was set to 100% at each time point. Quantification of attached cells was performed using the Operetta high content screener. (C) Cumulative cell viability was determined using the metabolic resazurin assay from 24 to 48 h post seeding. Values are given as relative fluorescence units (RFU). * indicates a significant difference in means, $p < 0.05$.

4.2.3 A scoring system facilitates the comparison of immersion-decellularization strategies

Selecting the most suitable decellularization approach from histology, quantification and recellularization data is difficult, since for that purpose qualitative and quantitative results have to be compared and condensed. Moreover, the comparison of the results of this study to other decellularization studies is even more difficult.

Therefore, a scoring system was developed that allows an unbiased comparison of all examined parameters and the calculation of a total score that can easily be compared. The scoring system translates all quantitative results into values from 1 (worst result) to 4 (best result). Moreover, the qualitative data, e.g. histological data, are translated into semi-quantitative values by defining scores from 1 to 4. To minimize subjective errors, clearly defined and whenever possible quantitative criteria are used to score preservation of characteristic renal ECM structures and cell removal. The values of the best results were derived from native tissue data. Overall, the three top level categories histology, ECM composition and cell performance were defined that can contain one or more subcategories of related analysis results. Subtotal scores were calculated for each subcategory by calculating the mean of the individual scores. These subtotal scores allowed the application of a weight function when calculating a total score and thus permit the adjustment of the overall influence of individual categories. Higher weight was applied to all categories containing quantitative data and to cell performance.

This scoring system was applied to compare the immersion-decellularization data after DNase treatment. The ECM decellularized with 1% SDS at 4 °C achieved the highest scores for histological and compositional maintenance, with scores of 3,67 and 3,19, respectively. Whereas ECM decellularized with 1% SDC at 4 °C achieved the highest score for cell viability and attachment, with a score of 3,33. Moreover, 1% SDC at 4 °C achieved the best total score of 3,23, due to the higher weight for cell performance. Surprisingly, the cell performance, considering IMC attachment and viability, did not correlate with collagen and GAG ratios, which were lower in the SDC scaffold compared to the SDS scaffold. Nor did it correlate with the remaining cytoplasmic material. Instead it did correlate with the cytokine content.

Table 26: Scoring table of immersion-decellularized porcine kidneys

Condition/ Parameter		SDC			SDS			TX-100			weight
		4 °C	RT	37 °C	4 °C	RT	37 °C	4 °C	RT	37 °C	
Histology											
General appearance	Remaining cytoplasmic material	3	2	2	4	4	2	1	1	1	
	Absence of nuclear structures	4	4	4	4	4	4	2	2	1	
	Shrinking	3	4	4	3	3	3	4	4	4	
	<i>subtotal</i>	3,33	3,33	3,33	3,67	3,67	3,00	2,33	2,33	2,00	1
Detailed analysis of specific structures	Tubules	3	2	3	3	2	4	4	3	4	
	Glomeruli	3	2	2	4	2	4	4	2	3	
	Vessels	4	4	4	4	3	4	4	4	4	
	<i>subtotal</i>	3,33	2,67	3,00	3,67	2,33	4,00	4,00	3,00	3,67	1
Histology-Score		3,33	3,00	3,17	3,67	3,00	3,50	3,17	2,67	2,83	1
Composition											
Matrix proteins (histology based)	Laminin	2	2	2	2	2	2	2	2	3	
	CollagenIV	4	4	4	4	4	4	4	4	4	
	Fibronectin	4	4	4	4	4	4	4	4	4	
	<i>subtotal</i>	3,33	3,33	3,33	3,33	3,33	3,33	3,33	3,33	3,67	1
Quantification of absolute composition	DNA content	4	4	4	4	4	4				
	<i>subtotal</i>	4,00	4,00	4,00	4,00	4,00	4,00				2
	Collagen content	3	3	2	4	3	4				
	Glycosaminoglycan content	1	1	1	4	4	3				
	<i>subtotal</i>	2,00	2,00	1,50	4,00	3,50	3,50				2
	basic Fibroblast Growth Factor (bFGF)	1	1	1	1	1	1				
	Vascular Endothelial Growth Factor (VEGF)	4	4	4	2	1	1				
<i>subtotal</i>	2,50	2,50	2,50	1,50	1,00	1,00				2	
Composition-Score		2,90	2,90	2,76	3,19	2,90	2,90				1
Cell performance											
Attachment and viability	Cell attachment 30h	3			2			2			
	Cell attachment 76h	3			2			2			
	Cell viability	4			1			3			
Cell performance-Score		3,33			1,67			2,33			2
Total Score		3,23			2,55						

Scores (1-4 points, highest score is best):	1	2	3	4	max value
Remaining cytoplasmic material	cytoplasm intact	cytoplasm only marginally reduced	cytoplasm mainly removed, only fragments	no cytoplasm remaining	
Absence of nuclear structures (Masson's Trichrome + DAPI)	nuclei intact	few nuclei, high amount of released DNA	no nuclei, but DNA detected	no nuclei, no DNA detected	
Shrinking	strong	medium	low	none	
Tubules, Glomeruli, Vessels	not visible/detectable	disrupted and/or collapsed architecture	moderate disruption of architecture	architecture intact	
Matrix proteins	absent	strongly reduced	slightly reduced	fully preserved	
DNA content (µg/mg)	20,0	15,0	10,0	5,0	20,0
Collagen content (µg/mg)	97,8	195,5	293,3	391,0	391,0
Glycosaminoglycan content (µg/mg)	8,3	16,7	25,0	33,3	33,3
bFGF (pg/mg)	63,7	127,4	191,1	254,8	254,8
VEGF (pg/mg)	14,4	28,9	43,3	57,7	57,7
Cell attachment (%)	25,0	50,0	75,0	100,0	100,0
Cell viability (RFU)	16027,5	32055,0	48082,5	64110,0	64110,0

4.3 Decellularization of kidneys by perfusion

Perfusion-decellularization allows the decellularization of whole organs. These scaffolds provide a true 3D environment to reseeded cells. Moreover, they provide the organ-specific architecture, ECM and mechanical stimuli, such as shear stress and stiffness. Perfusion-decellularized rat kidneys were therefore chosen as a scaffold to generate the human 3D kidney model.

The optimal decellularization parameters that were identified by the factor screening in the immersion and agitation setting were now transferred to the perfusion setting. Perfusion-decellularization was thus performed with 1% SDC, the decellularization agent that gave the best results in immersion-decellularization of kidney tissue cubes, and a combination of 1% SDS and 1% TX-100, a protocol that was published before for perfusion-decellularization of rat kidneys by Song et al.¹²³. Both protocols were tested at 4 °C and RT. Perfusion-decellularization was performed in the perfusion bioreactor developed in this thesis, see 4.1. Cell removal and composition of the scaffold were investigated after decellularization, analogous to the analysis of the immersion-decellularization. The scaffold's biocompatibility was investigated by reendothelialization of the vascular compartment with human umbilical vein endothelial cells.

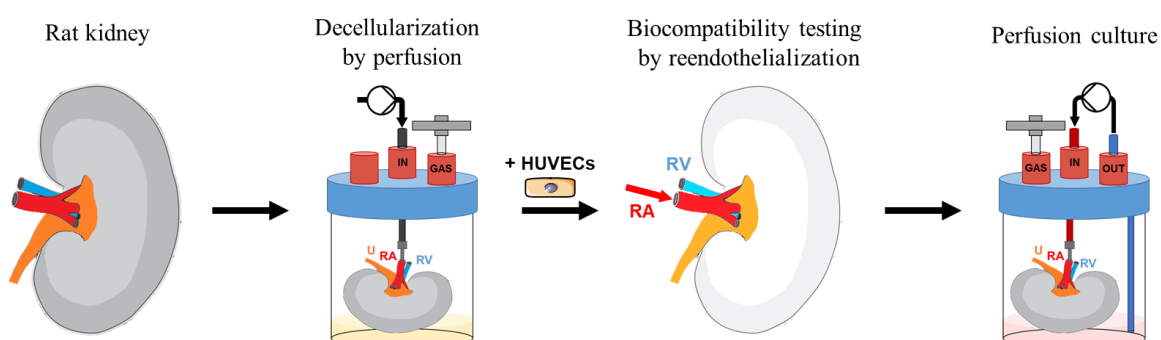


Figure 32: The experimental process of kidney decellularization by perfusion and biocompatibility testing of the scaffold by reendothelialization. Rat kidneys were cannulated and placed into the perfusion bioreactor. The kidneys were decellularized by perfusion with SDC or SDS/TX-100 at either 4°C or RT. Human umbilical vein endothelial cells (HUVECs) were seeded into the vascular compartment of the scaffold via the renal artery (RA) to investigate its biocompatibility. The reseeded kidneys were cultured under perfusion conditions with pH, pressure and temperature control.

4.3.1 Analysis of histology and composition after decellularization by perfusion

The color of the kidneys lightened during decellularization, indicating the cell removal in the tissue. The SDC-decellularized rat kidneys appeared macroscopically yellow, whereas the SDS/TX-100-decellularized kidneys lost their color completely and appeared white and translucent. No macroscopic pictures for the 4 °C samples are available (Figure 25).

HE staining of the native rat kidney revealed cell lined glomerular, tubular and vascular structures and a high density of round, intact nuclei.

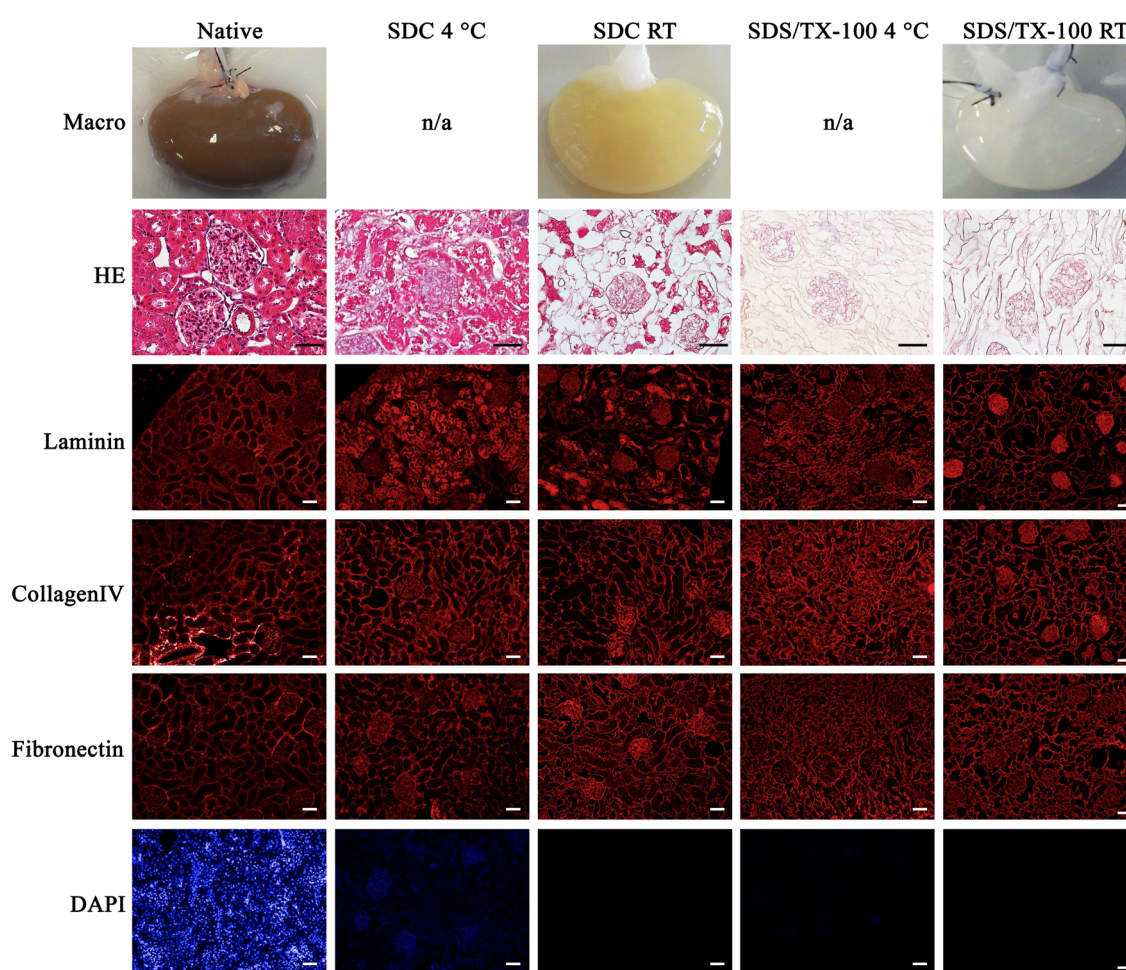


Figure 33: Macroscopic and histological analysis of native and perfusion-decellularized rat kidneys at 4 °C and RT. Native rat kidneys appeared brown. HE staining showed vessels, tubules and glomeruli filled with epithelial and endothelial cells with intact nuclei, confirmed by DAPI staining. The ECM molecules laminin, collagen I and IV and fibronectin were detected in the BM that line the tubules and glomerular capillaries. SDC-decellularized kidneys appeared yellow. HE and DAPI showed remaining cellular material, especially at 4 °C. The architecture was intact. SDS/TX-100-decellularized kidneys appeared white. HE and DAPI did not detect cellular residues. Tubules were collapsed. All decellularized samples stained positive for the ECM molecules. Scale bar: 50 µm.

Surprisingly and in contrast to the immersion data, the perfusion-decellularization with SDC at 4 °C showed very poor cell removal. The scaffold remained filled with cellular debris, although the cells and nuclei were not intact anymore, as shown by HE staining. DAPI staining detected residual dsDNA in the cell debris.

Cell debris was also still present in the SDC RT scaffold, although not as abundant as in the 4 °C sample. DAPI staining did not detect any residual dsDNA. The architecture was not negatively affected; all tubular, glomerular and vessel structures were intact.

In contrast, the decellularization with SDS/TX-100 at 4°C and RT removed all cellular debris completely, therefore, no DAPI signal was detectable. However, the SDS/TX-100-treated scaffolds showed an impairment of the architecture, as many tubules were collapsed.

The immunofluorescence staining of the ECM proteins laminin, collagen I, collagen IV and fibronectin showed that these ECM proteins were well preserved in all decellularization conditions with the exception of laminin in the SDC samples. In these samples the laminin staining was instead detected in the cellular debris. This is either an unspecific staining or an indication of a massive loss of laminin.

The composition of the decellularized kidney was further characterized by quantification of DNA, total collagens and total glycosaminoglycans.

Quantification of DNA in the decellularized scaffolds revealed a significantly higher DNA content in SDC 4 °C than in any other condition. Similarly, SDS/TX-100 4 °C showed slightly elevated DNA levels in comparison to the RT samples. Since SDC RT contained more cellular debris but less DNA/dry weight than SDS/TX-100 4 °C, the DNA content correlated not only with the degree of decellularization but also with the temperature. So, more cellular debris might have been flushed out, but the DNA did not degrade and stuck to the ECM instead. A DNase digest after the SDC 4 °C treatment, like it was also performed on all immersion samples, reduced the amount of DNA/dry weight significantly.

Comparable to the immersion data, a higher degree of decellularization led to an enrichment of collagen and hence to a higher collagen/ dry weight ratio. Therefore, both SDS/TX-100 conditions showed a higher collagen/ dry weight ratio than the SDC-treated samples.

The GAG/dry weight ratio results from perfusion-decellularization are contrary to the immersion data. In perfusion-decellularization, the SDC 4 °C sample did not contain the lowest but the highest GAG/dry weight ratio. All other samples had a similar GAG/dry weight ratio to the native sample, even the SDS samples that showed an elevated

GAG/dry weight ratio in immersion-decellularization. Therefore, the GAGs were not enriched like the collagens by the removal of cellular material but reduced as perfusion-decellularization progressed.

In summary, SDS/TX-100 at RT showed the best results in removing the cellular material and DNA. SDC was not able to remove the cellular material successfully in perfusion conditions, contrary to the immersion-decellularization results.

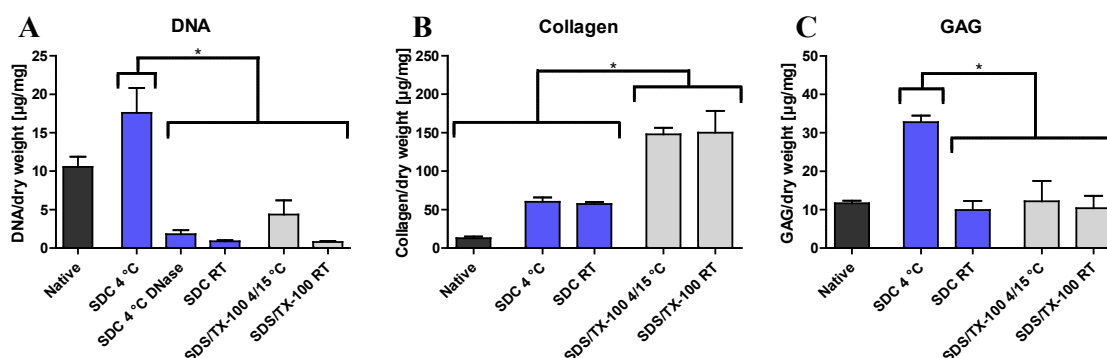


Figure 34: Composition analysis of perfusion-decellularized matrices. Quantitative analysis of DNA (A), total collagen (B) and GAG (C) content after decellularization by perfusion of whole rat kidneys using the indicated conditions. The specific amounts are given as the ratio of the target substance (in µg or pg) to the dry weight of the sample (mg). Values are expressed as mean ± SEM, * indicates a significant difference in means, $p < 0.05$.

4.3.2 Biocompatibility testing of perfusion-decellularized kidneys by reendothelialization with human umbilical vein endothelial cells

Human umbilical vein endothelial cells (HUVECs) were used to examine the qualification of SDC RT and SDS/TX-100 RT perfusion-decellularized rat kidney scaffolds for recellularization. HUVECs are primary endothelial cells that are therefore a suitable cell source for reendothelialization of the vascular tree. Additionally, they are easily expandable and robust.

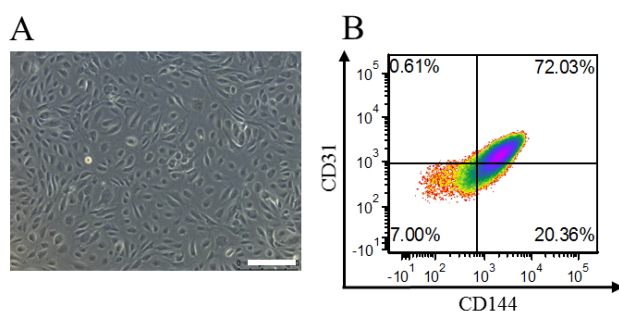


Figure 35: Characterization of human umbilical vein endothelial cells. (A) Human umbilical vein endothelial cells (HUVECs) exhibited the typical morphology with large nuclei. Scale bar: 200 µm. (B) Expression of the endothelial markers CD31 and CD144 was shown by flow cytometry.

HUVECs were expanded until passage 7. These cells showed a uniform morphology and 72% were double positive for the endothelial cell markers CD31 and CD144 (Figure 35).

5×10^7 HUVECs were injected into the renal artery of an SDC RT-decellularized rat kidney which was then placed inside the recellularization perfusion bioreactor (Figure 36A). After a static overnight (O/N) attachment phase the perfusion was started (day 0) and continued for 3 days. Culture medium samples were drawn regularly from the perfusion bioreactor during the course of the experiment. Glucose consumption and lactate production rates were highest at the first measurement after cell seeding. These rates decreased constantly during the culture period, indicating a constant decrease of cellular activity. Additionally, the lactate dehydrogenase (LDH) release, a marker for cell death, increased to 2,5 U/d after the static overnight attachment phase, then rose to 4,1 U/d after the first 7 h of perfusion and decreased thereafter. This indicated a massive cell loss in the first phase of the recellularization, corroborating the glucose and lactate measurements (Figure 36E). The kidney appeared brownish after the culture (Figure 36D). Histology showed that the cells were located in the vascular compartment, but many cells clogged the vessels rather than lining them. Moreover, many cell nuclei were fragmented and a DAPI signal could be observed throughout the scaffold, which indicates free dsDNA that was released by dying cells (Figure 36B,C).

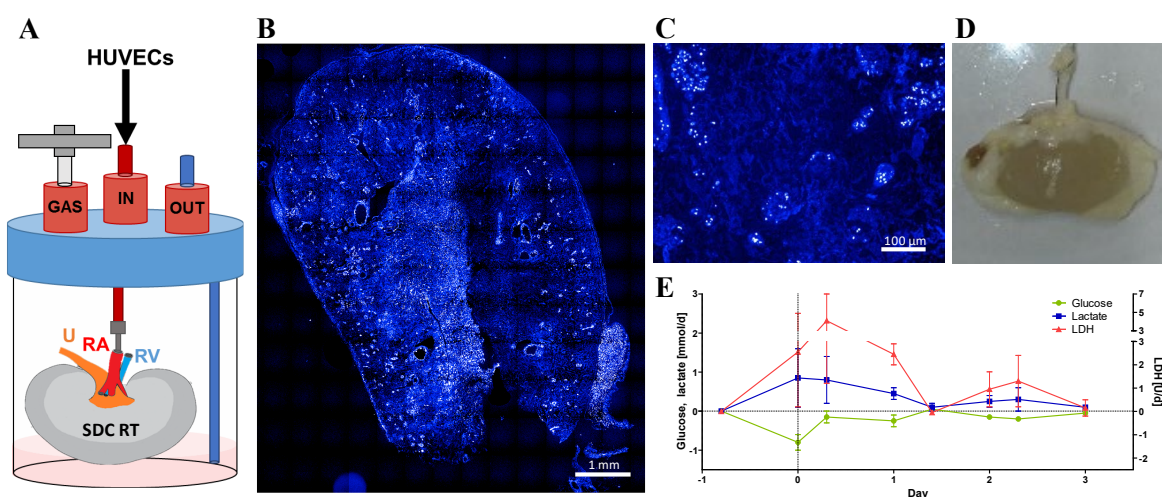


Figure 36: Reendothelialization of perfusion-decellularized kidneys by SDC at RT. (A) HUVECs were injected into the renal artery (RA) of the SDC-decellularized rat kidney. Perfusion culture was started after an overnight attachment period and then continued for 3 days. (B,C) DAPI stained cross-section after 3 days of perfusion culture. Bright DAPI staining in the scaffold and the presence of fragmented nuclei indicated cell death. Viable cells were present, but they did not line the vessels. (D) Picture of the fixed kidney after perfusion culture. Brown discoloration indicated cellular material inside the kidney. (E) Glucose, lactate and LDH consumption/production during the culture period. LDH values, a marker for cell death, increased rapidly after perfusion start, and dropped after the first day of culture.

The SDS/TX-100 RT-decellularized scaffold was also tested by recellularization with HUVECs via the artery (Figure 37A). Histology showed a successful reendothelialization of the vascular compartment. Many intact cell nuclei, detected by DAPI staining, lined the vessels. Many more nuclei were detected than in the SDC scaffold. The resazurin assay proofed high cell viability; the purple resazurin was metabolized to pink resorufin, staining the kidney bright pink after the assay (Figure 37D). Moreover, the lower LDH release than in the SDC reendothelialization, it only reached 2,0 U/d, confirmed the superior cell viability in the SDS/TX-100-decellularized kidney scaffold (Figure 37E).

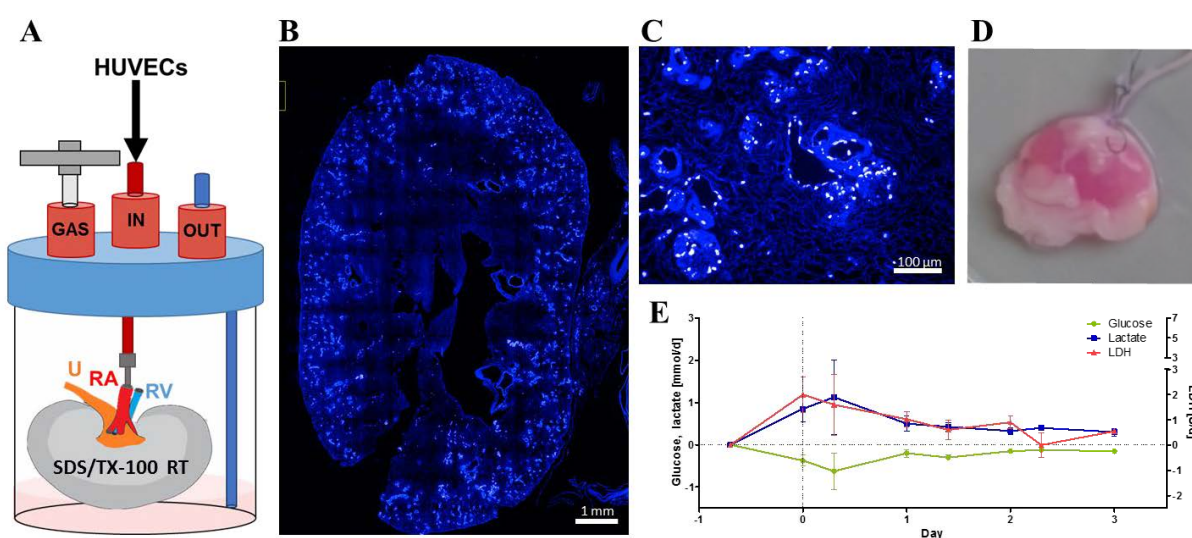


Figure 37: Reendothelialization of perfusion-decellularized kidneys by SDS/TX-100 at RT. (A) HUVECs were injected into the renal artery (RA) of the SDS/TX-100-decellularized rat kidney. Perfusion culture was started after an overnight attachment period and then continued for 3 days. (B,C) DAPI stained cross-section after 3 days of perfusion culture. High numbers of HUVECs were spread over the whole tissue, lining specifically bigger blood vessels and glomerular capillaries. (D) Viable cells reduced resazurin to the pink resorufin, throughout the whole recellularized kidney. (E) Glucose, lactate and LDH consumption/production during the culture period. Cells consumed glucose and produced lactate during the whole culture, although with decreasing levels. LDH values, a marker for cell death, were highest after perfusion start, but did only reach values of 2,0 U/d.

The cell number, metabolic activity and LDH release of the reseeded cells were quantified to further facilitate the decision for the best scaffold. Counting the intact nuclei on DAPI stained sections and normalization to 1 mm² revealed that SDS/TX-100 scaffolds hold 70% more intact nuclei than SDC scaffolds. Moreover, the metabolic resazurin assay shows a 17 times higher metabolic activity in the SDS/TX-100 scaffold. The higher cumulative LDH release in SDC scaffolds corroborates these data. Interestingly, this striking difference could not be seen in the cumulative glucose consumption nor in the lactate production (Figure 38).

Taken together, only the SDS/TX-100 RT scaffold was successfully reendothelialized by HUVECS. It supported higher cell attachment and survival.

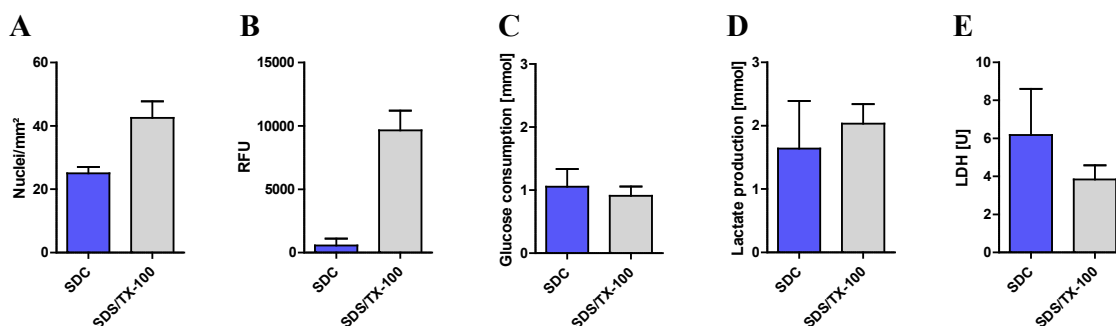


Figure 38: Comparative biocompatibility testing of perfusion-decellularized kidneys. Cell number and metabolic activity were quantified to compare the biocompatibility of SDC- and SDS/TX-100-decellularized rat kidneys. (A) More HUVEC nuclei were counted on DAPI stained sections of SDS/TX-100-decellularized than on SDC-decellularized kidneys. (B) Resazurin assay results, given in relative fluorescence units (RFU), quantify the metabolic activity of the reseeded cells. Cells reduced considerably less resazurin in SDC- than cells in SDS/TX-100-decellularized kidneys. No significant differences in (C) cumulative glucose consumption or (D) cumulative lactate production over 3 culture days. (E) HUVECs in SDC-decellularized kidneys had a higher cumulative LDH release, a maker for cell death.

4.3.3 Applying the scoring system for the comparison of perfusion-decellularization methods

4.3.3.1 Intra-study comparison

By applying the scoring system to the perfusion-decellularization data, the differences between the protocols were easily uncovered and summarized.

The SDC-decellularized samples achieved higher histology scores than the SDS/TX-100 samples, although they contained more cellular debris, because they preserved the architecture better. The SDC RT sample achieved the highest histology score with 3,83. However, the highest composition score was achieved by the SDS/TX-100 samples with 3,60, whereas the SDC samples, especially the 4 °C sample, got lower composition scores due to remaining DNA. Moreover, the SDS/TX-100 RT sample achieved with 4,00 a much better cell performance score than the SDC RT sample. Contrary to the superior cell performance of the SDC immersion samples.

In total, SDS/TX-100 RT achieved with 3,73 a clearly higher total score than SDC with a total score of 2,74. The decellularization with SDS/TX-100 at RT and was therefore chosen for the generation of the scaffold for the human kidney model.

Table 27: Scoring table of perfusion-decellularized rat kidneys

Condition/ Parameter		SDC		SDS/TX-100		weight
		4 °C	RT	4 °C	RT	
Histology						
General appearance	Remaining cytoplasmic material	2	3	4	4	
	Absence of nuclear structures	3	4	3	4	
	Shrinking	4	4	2	3	
	subtotal	3,00	3,67	3,00	3,67	1
Detailed analysis of specific structures	Tubules	4	4	2	3	
	Glomeruli	4	4	2	3	
	Vessels	4	4	3	3	
	subtotal	4,00	4,00	2,33	3,00	1
Histology-Score		3,50	3,83	2,67	3,33	1
Composition						
Matrix proteins (histology based)	Laminin	3	3	4	4	
	Collagen IV	4	4	4	4	
	Fibronectin	4	4	4	4	
	subtotal	3,67	3,67	4,00	4,00	1
Quantification of absolute composition	DNA content	1	4	4	4	
	subtotal	1,00	4,00	4,00	4,00	2
	Collagen content	2	2	4	4	
	Glycosaminoglycan content	4	2	2	2	
subtotal	3,00	2,00	3,00	3,00	2	
Composition-Score		2,33	3,13	3,60	3,60	1
Cell performance						
Attachment and viability	Cell count 76h		3		4	
	Cell viability 76h		1		4	
Cell performance-Score			2,00		4,00	2
Total Score			2,74		3,73	

Scores (1-4 points, highest score is best):	1	2	3	4	max value
Remaining cytoplasmic material	cytoplasm intact	cytoplasm only marginally reduced	cytoplasm mainly removed, only fragments	no cytoplasm remaining	
Absence of nuclear structures (Masson's Trichrome + DAPI)	nuclei intact	few nuclei, high amount of released DNA	no nuclei, but DNA detected	no nuclei, no DNA detected	
Shrinking	strong	medium	low	none	
Tubules, Glomeruli, Vessels	not visible/detectable	disrupted and/or collapsed architecture	moderate disruption of architecture	architecture intact	
Matrix proteins	absent	strongly reduced	slightly reduced	fully preserved	
DNA content (µg/mg)	17,6	13,2	8,8	4,4	17,6
Collagen content (µg/mg)	37,0	74,0	111,0	147,9	147,9
Glycosaminoglycan content (µg/mg)	8,2	16,4	24,6	32,8	32,8
Cell count (nuclei/image)	3,8	7,6	11,4	15,2	15,2
Cell viability (RFU)	2409,5	4819,0	7228,5	9638,1	9638,1

4.3.3.2 Inter-study comparison

To compare the intra-study results to these of other published studies, three studies on kidney decellularization were scored (Table 28). The published data were directly transferred into the scoring table to avoid bias by third party assessment of these data.

In the study by He et al.¹⁴⁸ SDS perfusion was applied to decellularize whole rat kidneys. The effect of different SDS concentrations (1%, 0,5%, 0,25%, 0,125% w/v) and incubation times

(4 h and 8 h) was examined. The scoring system easily visualized the strong impact of incubation time as well as concentration on the ECM composition. The optimal condition in this set of experiments, with a total score of 3,33, turned out to be the mildest condition utilizing 0,125% w/v SDS for 4 h. This treatment was sufficient to remove all cellular material while best preserving total collagen, GAG and cytokines. Only quantitative data were used for scoring as the authors described no differences in the histology and the published image data could not be scored.

Table 28: Scoring table of perfusion-decellularized rat and porcine kidneys

Condition/ Parameter	He et al.						Caralt et al.			Poornejad et al.					weight
	SDS 4h				SDS 8h		1% TX-100	1% TX-100 / 0.1% SDS	0,02% Trypsin-EGTA / TX-100	0,1 N NaOH	1% PAA	3% TX-100	1% SDS	0,05% Trypsin-EDTA	
	0,125%	0,25%	0,50%	1,00%	0,125%	0,25%									
Histology-Score							3,67	3,83	3,83	2,08	2,75	2,63	2,67	1,25	1
Composition-Score	3,33	2,67	2,50	2,67	2,00	2,00	1,83	2,70	2,90	2,30	2,71	2,38	2,24	1,90	1
Cell performance-Score										4,00	4,00	3,00	1,00	1,00	2
Total Score	3,33	2,67	2,50	2,67	2,00	2,00	1,83	3,18	3,37	3,07	2,71	2,71	2,38	2,24	1,90

Caralt et al.¹⁴⁴ compared the effect of TX-100 alone or in combination with SDS or trypsin/EGTA on whole rat kidney decellularization. In Caralt's study TX-100 alone did not yield in a complete cell removal. The histology score of 3,67 was therefore lower than the scores for SDS/TX-100 and trypsin-EGTA/TX-100 of 3,83. This is in line with the results of this thesis, which yielded lower histology scores for TX-100 than SDC or SDS. Interestingly, the combination of TX-100 with trypsin/EGTA resulted in a good removal of cellular material but also degraded nearly completely the examined cytokines. Thus, the combination of TX-100 with SDS was the optimal condition in these set of experiments, with a total score of 3,37.

Poornejad et al.¹⁴⁹ compared next to TX-100, SDS and Trypsin-EDTA also the less commonly used decellularization reagents sodium hydroxide (NaOH) and peracetic acid (PAA). In contrast to the other two studies, the cell performance of the different decellularized ECMs was examined. Decellularization with trypsin-EDTA resulted in the lowest scores for histology and composition, analogous to the results by Caralt et al. The other examined decellularization reagents yielded in rather similar histology and composition scores, with PAA and NaOH performing slightly better compared to TX-100 and SDS. Only the cell performance assessment fully revealed the differences between these scaffolds and, comparable to this study, the cell performance results could not be concluded

from the results of the other examined parameters. Interestingly, also in Poornejad's study TX-100 derived ECM showed a better cell performance than SDS despite the incomplete removal of cellular material. Altogether PAA achieved the best total score of 3,37 in Poornejad's study.

These comparisons confirmed that SDS seems to be the optimal detergent for decellularization of kidneys by perfusion.

4.4 Recellularization of perfusion-decellularized kidneys

The scaffolds generated by perfusion-decellularization of whole rat kidneys with SDS/TX-100 were now recellularized to generate the human *in vitro* 3D kidney model.

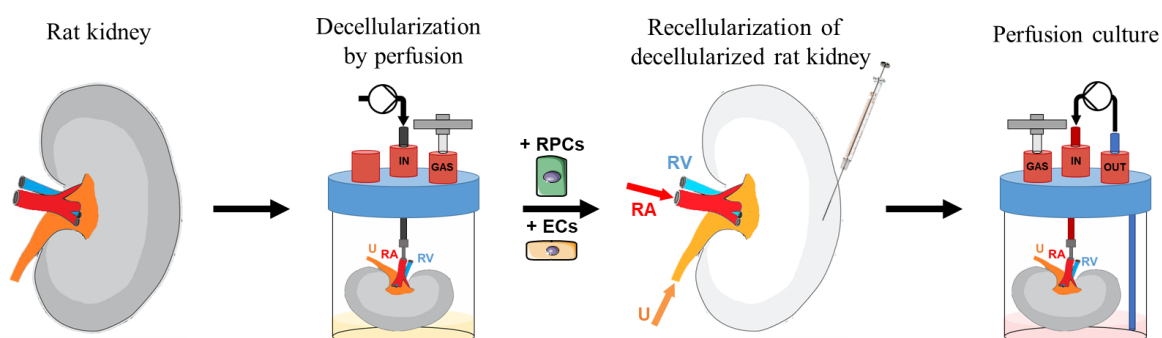


Figure 39: Generation of the kidney model by de- and recellularization of rat kidneys. Rat kidneys were decellularized by perfusion with SDS/TX-100 at RT. The scaffold was reendothelialized with hiPSC-derived endothelial cells (ECs) via the RA. The kidney parenchyma was planned to be recellularized with hiPSC-derived renal progenitor cells (RPCs). Three different seeding routes, such as seeding via the renal artery (RA), via the ureter (U), or by injections into the cortex with a syringe, were assessed. The recellularized kidneys were cultured under perfusion conditions with pH, pressure and temperature control.

Therefore, hiPSC-derived endothelial cells (ECs) were seeded into the vascular compartment of the decellularized kidney via the renal artery (RA). The recellularization of the decellularized renal parenchyma with hiPSC-derived renal progenitor cells (RPCs) was assessed by seeding the cells via the renal artery, the ureter (U) or via injection into the cortex with a syringe. The recellularized kidneys were cultured in the perfusion bioreactor with pH, pressure and temperature control.

4.4.1 Reendothelialization with hiPSC-derived endothelial cells

The EC differentiation protocol was adapted from Patsch et al.¹⁰⁹. In five days the hiPSCs differentiated into a confluent layer of 50,68% CD144 positive endothelial cells. The CD144 positive cells were magnetically sorted and expanded for six more days. During this time the cells matured to CD31/CD144 double positive ECs (Figure 40).

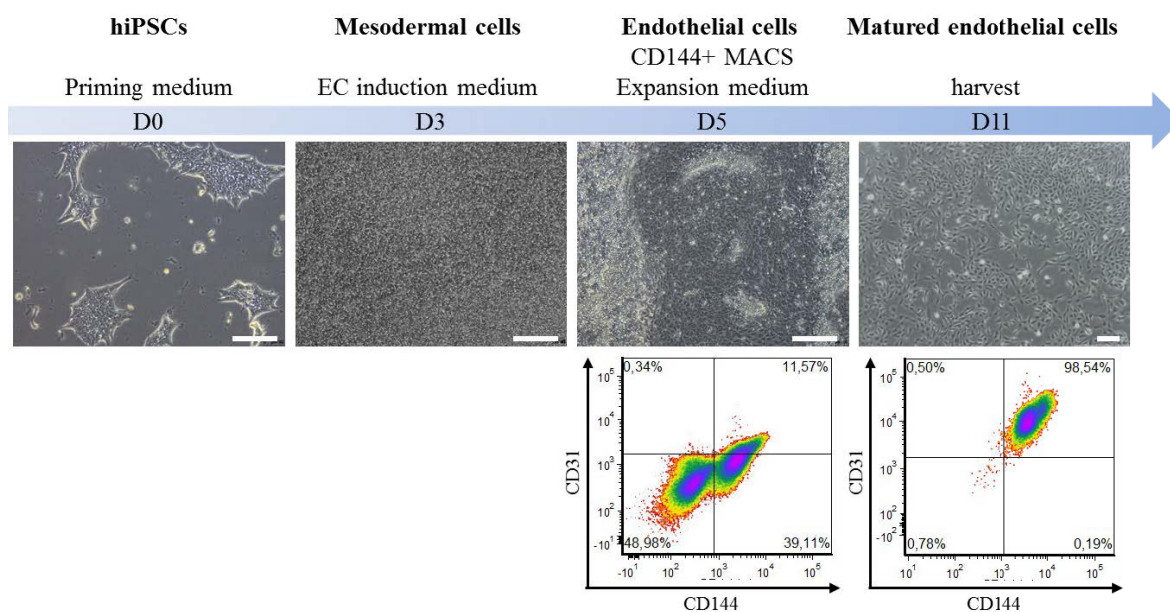


Figure 40: Differentiation scheme of hiPSC-derived endothelial cells. Endothelial cells were differentiated from hiPSCs in a 5-day protocol. At day 5, 50,68% of the cells were CD144+, as shown by flow cytometry. The CD144+ cells were magnetically sorted and reseeded into expansion medium. After 6 days of expansion, on day 11, 98,54% of the cells matured into CD31/CD144 double positive endothelial cells. Brightfield images show the morphological changes during the differentiation process. Scale bar: 200 μ m.

Special focus was laid on the expansion phase of the ECs, since millions of cells are needed to recellularize a whole rat kidney. The criteria for a successful expansion are cell proliferation, measured in population doublings (PDL), and EC marker stability, measured in the proportion of CD144/CD31 double positive cells. Furthermore, the cost of the expansion medium was considered. Patsch et al. proposed the expansion in StemPro-34 medium on fibronectin coating. StemPro-34 medium costs about 500€/l. Although the EC maturation and phenotype stability were excellent, this condition was not suitable for the expansion, since the cells did not proliferate. Additionally, gelatin coating was included as a comparison, since it is much less costly than fibronectin. The marker stability and PDL are comparable to fibronectin coating. EC-SFM medium¹⁴² also stabilized the phenotype over the whole tested period of 36 days and supported 11 PDL on fibronectin and costs only about

300 €/l. Notably, the PDL curve flattened over time, indicating a decreasing proliferation rate over time. EGM-FCS-SB medium¹⁴¹ stabilized the phenotype for 26 days. Thereafter, the percentage of double positive ECs dropped from 93% to 77%. However, the cell proliferation is higher than with any other tested medium; 16 PDL on fibronectin and 12 PDL on gelatin over the course of 36 days. Therefore, 26 days on gelatin will be sufficient to produce the number of cells needed for reendothelialization. Moreover, EGM-FCS-SB medium is with about 200 €/l by far the cheapest medium and was therefore chosen for the expansion of the hiPSC-derived ECs for the human kidney model.

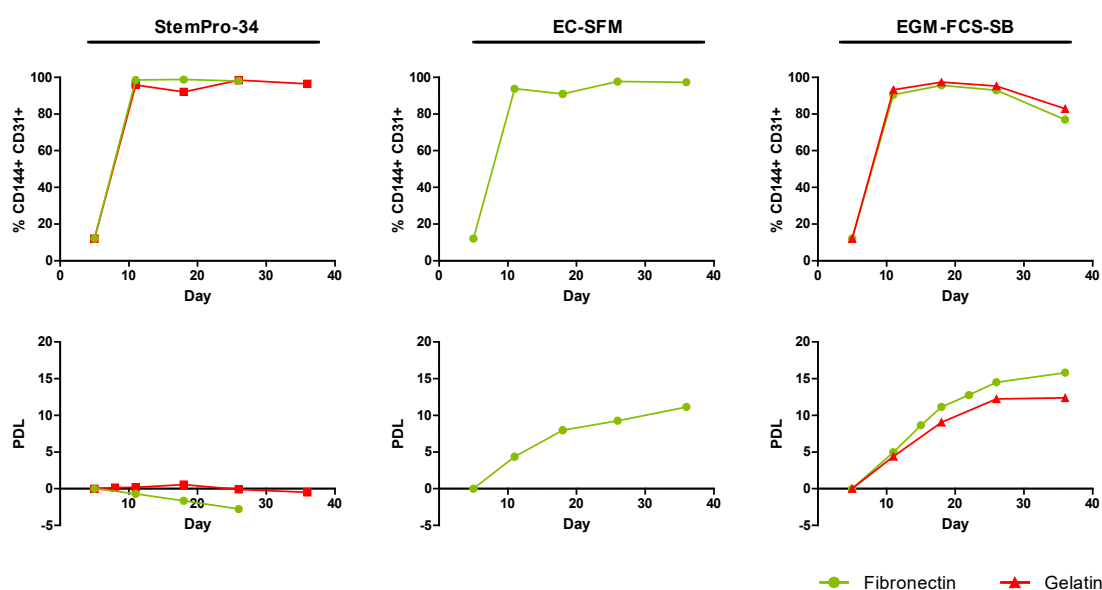


Figure 41: Optimization of hiPSC-ECs expansion conditions. At day 5 of hiPSC-EC differentiation, the ECs were sorted for CD144 and seeded into three different expansion media with fibronectin or gelatin coating. The expansion rate, given as population doubling (PDL), and the endothelial phenotype stability, given as the percentage of CD144 and CD31 double positive cells, were analyzed to identify the optimal expansion medium. The phenotype was stable for 26 days in all conditions. The expansion was highest in EGM-FCS-SB medium on fibronectin coating.

To reendothelialize the rat kidney scaffold, 5×10^7 hiPSC-derived ECs were injected into the renal artery, analogous to the reendothelialization with HUVECs. The perfusion culture was commenced after an overnight attachment phase and continued for six days.

As already observed in the HUVEC reendothelialization, LDH release was highest shortly after seeding and decreased thereafter. Hence, cells died during seeding but survived thereafter. Glucose and lactate measurement were fluctuating around 0 mmol/d. These measurements are impaired by the high medium volume to cell ratio. The perfusion with resazurin detected a high cell viability in the scaffold, especially in the interlobar and arcuate

arteries. These data were corroborated by the histological analysis. The vessels were densely populated with ECs lining the vessel walls (Figure 42).

In comparison to the HUVEC experiment, however, slightly less cell nuclei and metabolic activity were detected. Therefore, it appears that hiPSC-derived ECs are not as robust as HUVECs. Nevertheless, a good reendothelialization result was achieved with hiPSC-derived ECs.

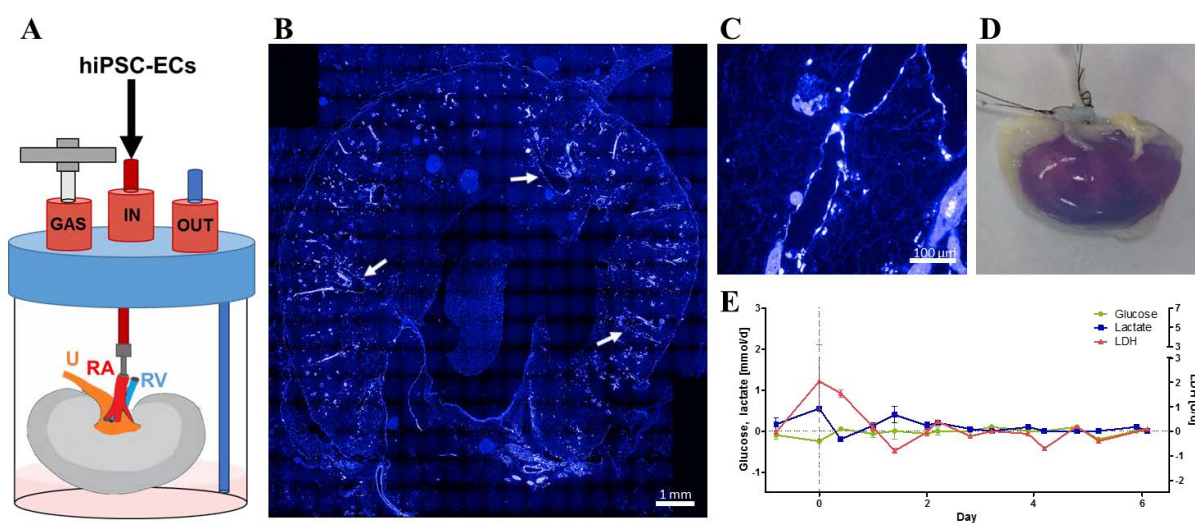


Figure 42: Arterial seeding of hiPSC-ECs. (A) hiPSC-ECs were injected through the IN port of the perfusion bioreactor into the renal artery of the decellularized rat kidney. Perfusion culture started after O/N static culture. (B) DAPI stained cross-section after 6 days of perfusion culture. ECs were spread over the whole tissue, lining specifically the bigger blood vessels (white arrows), as shown in more detail in (C). (D) The resazurin-assay detected viable cells in the vascular tree. (E) LDH release was highest shortly after perfusion culture start. Glucose, lactate metabolism was hardly detectable, due to the high medium volume.

CD31 staining on sections of a native human kidney, a HUVEC recellularized kidney and an hiPSC-EC recellularized kidney revealed the exact localization and morphology of the endothelial cells. In the native human kidney, CD31 positive ECs were detected lining the segmental, interlobar, arcuate and interlobular arteries and veins, the afferent and efferent arterioles and the delicate glomerular and peritubular capillaries. The recellularized rat kidneys showed similar staining patterns, which suggests an effective reendothelialization. The cells did not migrate out of the vascular compartment. They lined the vessels walls, only some cell plugs were found inside the vessels. Merely the microstructure in the glomerular capillaries was not as well formed as in the native kidney.

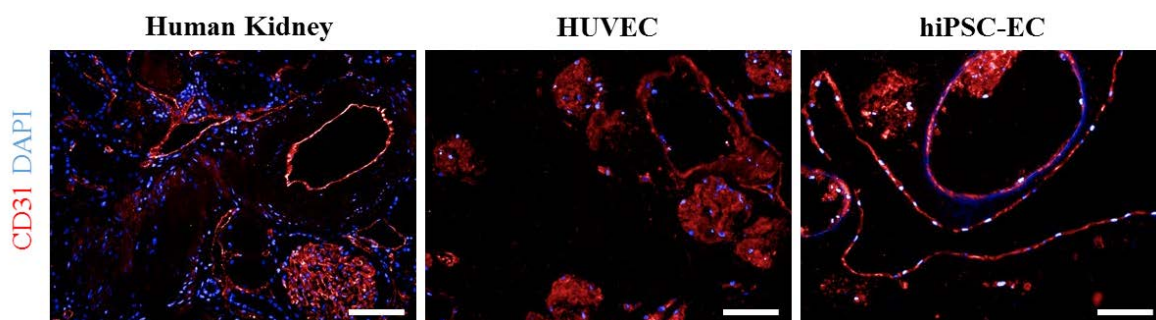


Figure 43: CD31⁺ endothelial cells lined the blood vessels and the glomerular capillaries in the recellularized kidneys. The delicate structure of the human kidney glomerulus was not achieved in the recellularized kidneys. No differences between HUVEC and hiPSC-EC recellularizations were prominent. Scale bar: 100 μ m.

4.4.2 Recellularization of the kidney parenchyma with hiPSC-derived renal progenitor cells

The kidney parenchyma was planned to be recellularized with hiPSC-derived RPCs. It was hypothesized that the preserved architectural, mechanical and biochemical features of the decellularized kidney scaffold promote site-specific maturation of the RPCs and the generation of a functional 3D kidney model.

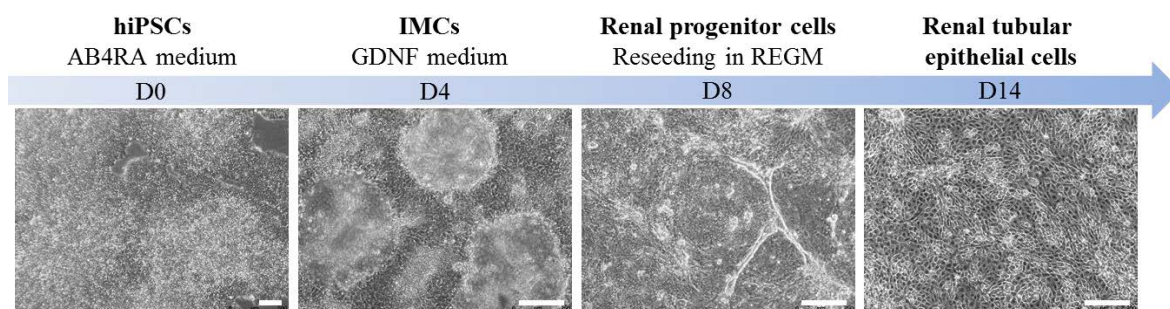


Figure 44: Differentiation scheme of hiPSC-derived RPCs. Renal progenitor cells were differentiated from over confluent hiPSCs. At day 3, hollow domes emerged from the confluent cell monolayer. At day 4, IMCs were formed. The domes collapsed after the change to GDNF containing medium. At day 8, hiPSC-derived RPCs could be harvested. To generate renal tubular epithelial cells, RPCs were cultured for 6 more days in REGM. Brightfield images show the cell morphology during the differentiation process. Scale bar: 200 μ m.

RPCs were differentiated from hiPSC using a protocol developed in our lab by Hariharan et al.¹¹⁷. The protocol differentiates hiPSCs after four days into dome forming intermediate mesoderm cells and after eight days into RPCs, as shown in Figure 44. The hiPSC-derived RPCs can differentiate into various mature renal cell types, for example into renal tubular epithelial cells (RTECs) when cultured for six more days in REGM.

The most efficient way to seed the cells into the decellularized parenchyma was investigated next.

4.4.2.1 Arterial seeding

The arterial seeding was successfully applied for the endothelial cells. Therefore, arterial seeding was also tested for RPCs, although in contrast to the endothelial cells, the RPCs should not settle in the vascular tree but should populate the renal tubules and glomerular structures.

When 3×10^7 RPCs were seeded into the renal artery with the same seeding protocol that was used for the endothelial cells, rarely any cells survived the five days of perfusion culture. The DAPI staining showed cell debris located in the vascular compartment. No cells were detected in the tubular structures. Also, the metabolic activity measured by the resazurin assay or the glucose and lactate metabolism was only minimal (Figure 45). Therefore, the RPCs seem to be much more fragile and sensitive than HUVECs which survived the same recellularization procedure without difficulty. Additionally, the RPCs did not migrate out of the vascular tree, analogous to the endothelial cells before. A simple arterial seeding is hence not sufficient for parenchymal recellularization.

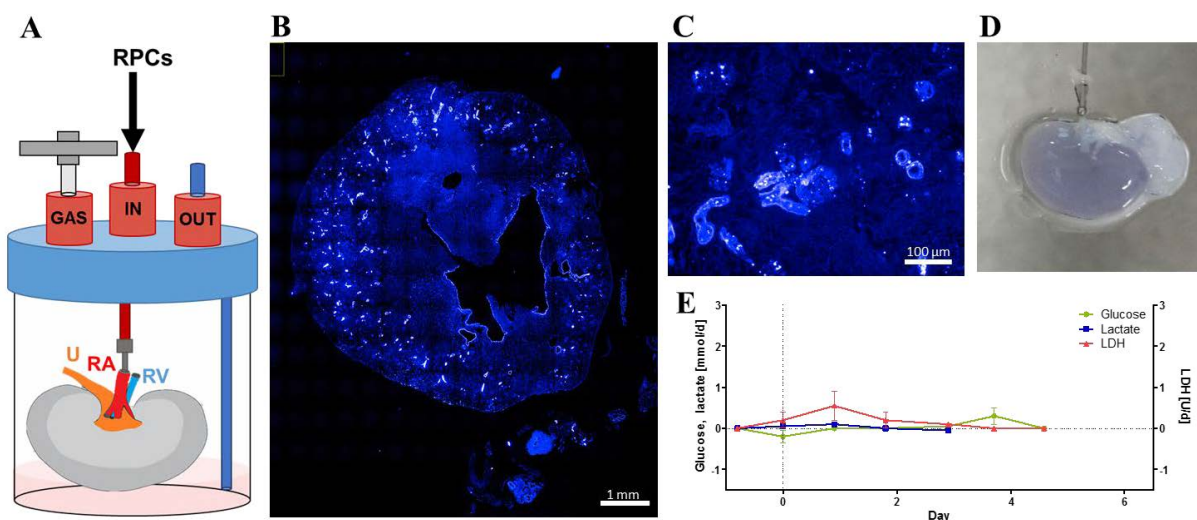


Figure 45: Arterial seeding of RPCs. (A) RPCs were injected through the IN port of the perfusion bioreactor into the renal artery of the decellularized rat kidney. Perfusion culture started after O/N static culture. (B,C) DAPI stained cross-section after 5 days of perfusion culture. Fragmented nuclei indicated cell death of the majority of cells. Cells were located in the vascular compartment, no migration into the tubular compartment was observed. (D) No color change from purple to pink in the resazurin-assay indicated low cell survival. (E) Low glucose consumption and lactate production corroborated the low cell viability.

Since no cells migrated into the tubular compartment with the standard arterial seeding, high pressure seeding was applied next, as described by Caralt et al.¹⁴⁴. The RPCs were injected into the renal artery. Medium perfusion was started immediately afterwards with 25 ml/min for 15 min, without an overnight attachment phase. Histology revealed cavities in the scaffold that were most likely ripped into the scaffold during this high-pressure seeding phase. These holes were surrounded by many living cells. Also, other areas of the scaffold showed successful recellularization, mainly parts of the renal cortex but also some tubules in the medulla. However, in total only a small fraction of the scaffold was repopulated. Resazurin perfusion stains the denser populated side of the kidney pink, corroborating the histology data. The glucose, lactate and LDH values were very low and peak shortly after perfusion culture start. This is again due to the very low total number of cells that attached in the scaffold (Figure 46). Thus, high pressure seeding slightly improved the efficiency of the arterial seeding, at the expense of the scaffold's integrity. However, the efficiencies described by Caralt et al.¹⁴⁴ were not reproducible.

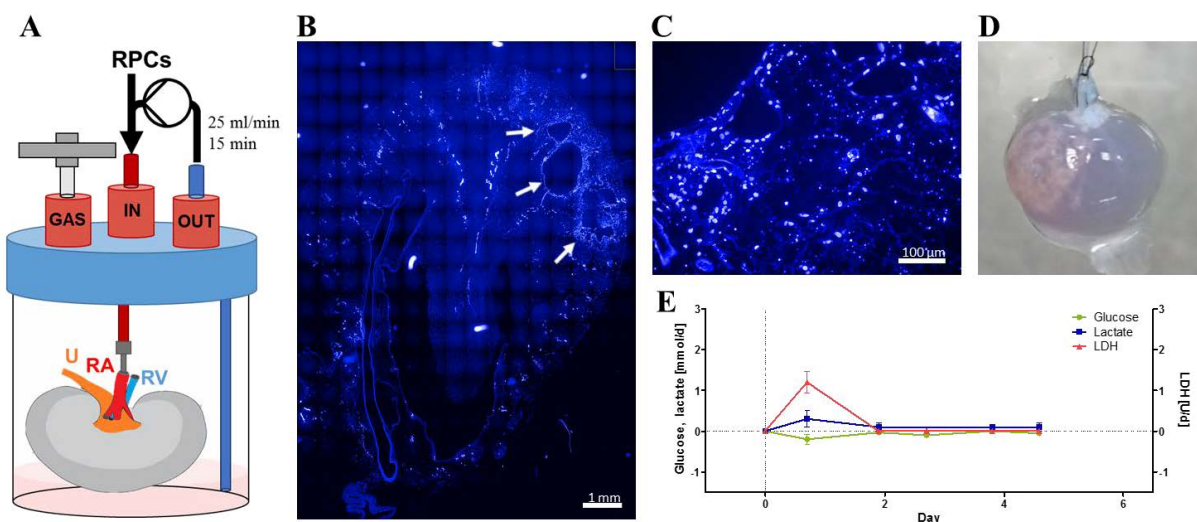


Figure 46: High-pressure arterial seeding of RPCs. (A) RPCs were injected through the IN port of the perfusion bioreactor into the renal artery of the decellularized rat kidney. Immediately followed by a high-pressure perfusion for 15 min to push the cells from the vascular compartment into the tubular compartment. (B,C) DAPI stained cross-sections after 5 days of perfusion culture. Cavities in the cortex indicate scaffold ruptures due to the high-pressure perfusion. Cells reached the tubules around the cavities (white arrows). (D) Color change from purple to pink in the resazurin-assay in the areas where the cavities and cells are detected in (B) indicated successful cell seeding and survival. (E) LDH release peaked shortly after perfusion start, indicating cell death. Too less cells populate the scaffold thereafter to generate measurable glucose and lactate values.

Next, another approach was analyzed that could improve the tubular repopulation in an arterial seeding. This approach included a short trypsin digest to weaken the vascular basal membrane. Hypothetically, the RPCs could migrate easier into the tubular compartment through a weakened basal membrane. However, arterially injected trypsin probably diffuses out of the decellularized vascular tree into the parenchyma. Therefore, this technique most likely sacrifices functional and structural proteins in the tubular basement membranes that were carefully preserved during decellularization. Trypsin was injected into the artery, incubated for 1 h and washed out carefully before cell seeding.

Histology showed that RPCs were able to reach the tubular compartment in the cortex but mostly died as mainly cell debris is detectable. The structure of the bigger arteries, e.g. the interlobar and arcuate arteries, were well preserved. Therefore, the RPCs must have passed the vascular basal membrane at smaller vessels with less pronounced vessel walls, e.g. the interlobular vessels, arterioles or capillaries. Whether the cells migrated actively and subsequently died or died first and were only passively washed into the tubular structures remains unclear. Metabolic measurements confirmed the low cell viability in the scaffold (Figure 47). Consequently, trypsin pretreatment of the scaffold did not improve arterial seeding.

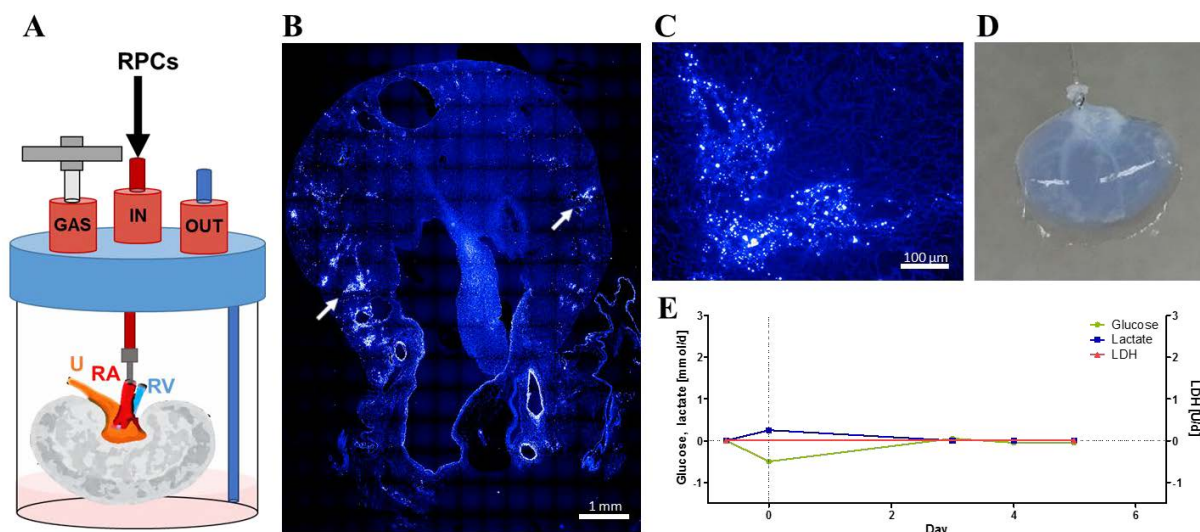


Figure 47: Arterial seeding of RPCs into partly trypsin-digested scaffolds. (A) Decellularized kidneys were partly digested with trypsin for 1 h to facilitate cell migration from the vascular tree into the tubular compartment. RPCs were injected into the renal artery of the decellularized rat kidney. (B,C) DAPI stained cross-sections after 5 days of perfusion culture show primarily degraded nuclei (white arrows). (D,E) No metabolic activity was detected.

4.4.2.2 Ureter seeding

The ureter is the direct seeding port into the tubular compartment. For seeding RPCs through the ureter, it was cannulated with a beveled catheter. To allow the undisturbed drainage of the decellularization agents and cell debris during the decellularization, the ureter was cannulated after decellularization.

3×10^7 RPCs were injected in 1ml REGM via the ureter cannula. A dilation of the renal pelvis and compression of the renal papilla due to the ureter seeding was revealed by histological analysis. The dilated pelvis was lined with cells, but the cells rarely advanced into the renal ducts and tubules of the parenchyma. Thus, the resazurin perfusion showed metabolic activity only in the center of the kidney. Glucose consumption and lactate production were low but detectable, confirming the low cell count (Figure 48). A simple infusion of RPCs through the ureter did not recellularize the parenchyma.

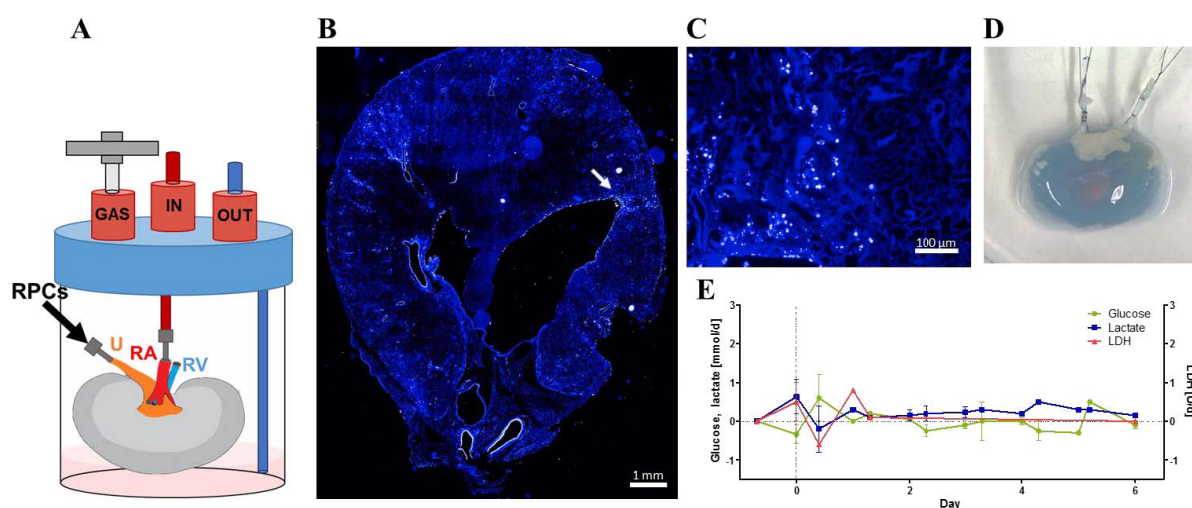


Figure 48: Ureter seeding of RPCs without vacuum. (A) RPCs were injected into the cannulated ureter of the decellularized rat kidney. Perfusion culture started after O/N static culture. (B,C) DAPI stained cross-sections after 6 days of perfusion culture revealed a dilated renal pelvis with cells lining the cavity. Only the minority of cells reached the tubules of the medulla or cortex (white arrow). (D) Therefore, the resazurin-assay only showed metabolically active cells in the center of the scaffold and (E) only low levels of glucose and lactate metabolism were detected.

To enhance the transfer of the seeded cells from the pelvis into the tubular structures a seeding protocol published by Song et al.¹²³ was tested. After cell injection into the ureter, 100 mbar vacuum were applied to the bioreactor to pull the RPCs into the ducts and tubules. The analysis revealed a slightly improved seeding success in comparison to the ureter seeding without vacuum. Again, histological analysis showed an enlarged, cell lined pelvis

and only some areas where cells advanced into the cortex. However, the cells did not line the tubules in a closed epithelial layer, they were rather scattered through the scaffold or clumped together. The pelvis was even more enlarged than in the simple ureter seeding approach. The resazurin perfusion showed more metabolically active cells than in the ureter seeding without vacuum. The pink stain, which indicates viable cells, was again mainly located in the center of the kidney, although cortex areas were stained too. LDH release, a marker for cell death, was detected in the first two days of the perfusion culture. Low glucose and lactate metabolism were detected over the full culture period and corroborates the low cell number detected in the DAPI stain (Figure 49). Therefore, the ureter seeding was improved by the vacuum application, but the scaffold was still not sufficiently recellularized for further analysis of the cell maturation. Hence, the results by Song et al. could not be reproduced.

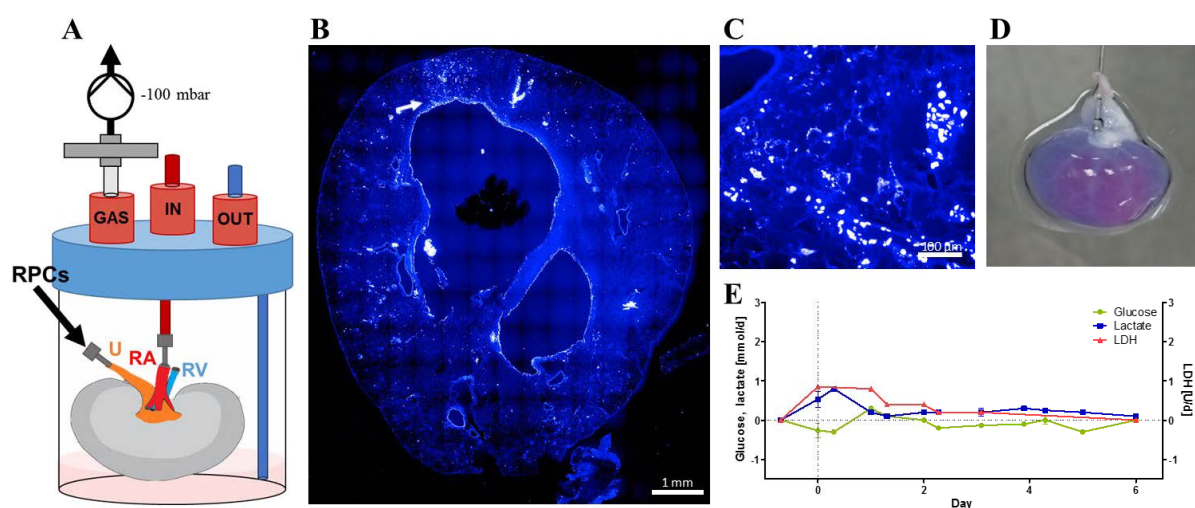


Figure 49: Ureter seeding of RPCs with vacuum. (A) RPCs were injected into the cannulated ureter of the decellularized rat kidney, followed by applying 100 mbar vacuum to the bioreactor to facilitate the cell passage from the pelvis into the tubules. Perfusion culture started after O/N static culture. (B,C) DAPI stained cross-sections after 6 days of perfusion culture revealed an enlarged renal pelvis with cells lining the cavity. In some parts the cells reached the tubules of the medulla or cortex (white arrow). (D) Therefore, the resazurin-assay shows metabolically active cells in the center and on one side of the scaffold. (E) Due to the low number of cells only low levels of glucose and lactate metabolism were detected.

4.4.2.3 Syringe seeding

Another option to recellularize the kidney parenchyma is to inject the cells directly with a syringe into the cortex. When 100 μ l cell suspension were injected in one shot, the scaffold ripped as shown in Figure 50B. These holes were lined with cells that did not advance into the surrounding tubular structures. When 5 μ l cell suspension were injected per shot, the

scaffold rupture was much smaller, but again, cells did not migrate away from the injection site. Zones where cells were flushed from the site of the injection into the surrounding tubules and glomeruli were rarely found (Figure 50C). Resazurin perfusion showed low metabolic activity in the kidney. LDH release, glucose consumption and lactate production were low during the whole culture period.

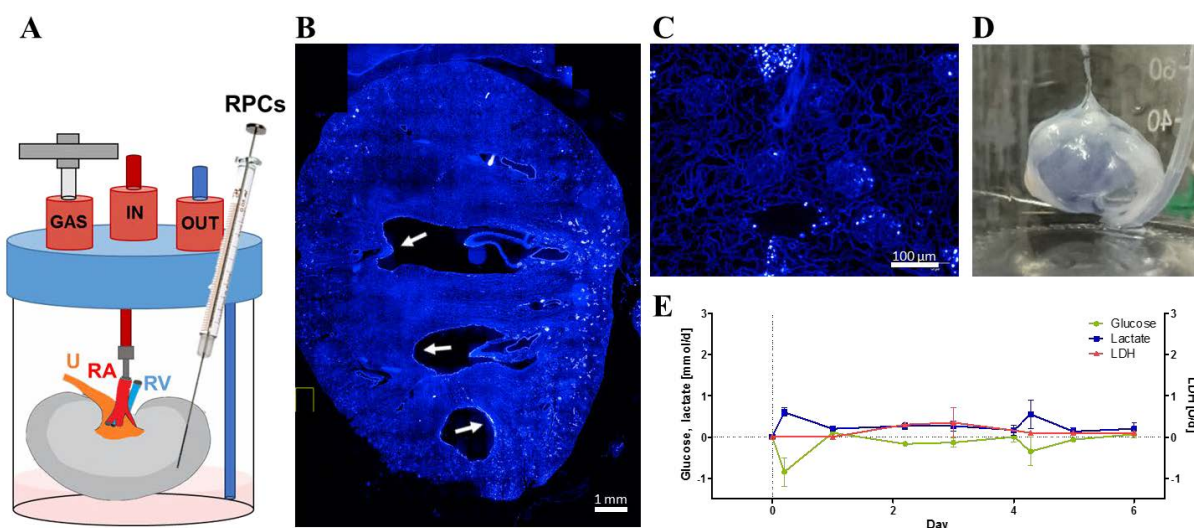


Figure 50: Injection of RPCs into the cortex of perfusion-decellularized kidneys with a syringe. (A) RPCs were injected into the cortex of decellularized rat kidney with a 27-gauge needle. Perfusion culture started after O/N static culture. (B,C) DAPI stained cross-sections after 6 days of perfusion culture revealed cell lined cavities. The majority of the cortex and medullary regions were cell free. Cells in the cavities did not migrate away from the site of the injection (white arrows). (D) Due to the low cell number, rarely any metabolic activity was detected with the resazurin-assay. (E) Also, only low levels of glucose and lactate metabolism were detected.

4.4.2.4 Seeding strategy comparison

A clear comparison of the RPC seeding efficiencies was achieved by counting the nuclei on DAPI stained cross-sections and normalizing the cell count to one mm². The highest counts were achieved with high-pressure arterial seeding and syringe seeding, followed by low-pressure arterial and vacuum-assisted ureter seeding strategies. The lowest counts were achieved with the artery with trypsin and ureter without vacuum approaches. However, all approaches reached merely between 4 and 26 nuclei/mm² and are therefore in the range of 1% of the native kidney cell density of 2364 nuclei/mm² (Figure 51A). This observation is corroborated by the quantification results of the resazurin assay (Figure 51B). Additionally, RPCs that were seeded successfully into the scaffold did not form tubular structures but were

rather scattered across the scaffold (Figure 45-Figure 50). Therefore, no further analysis of the maturation of the RPCs was possible.

In conclusion, none of the recellularization approaches did reach a cell density or cell arrangement required to generate a human kidney model.

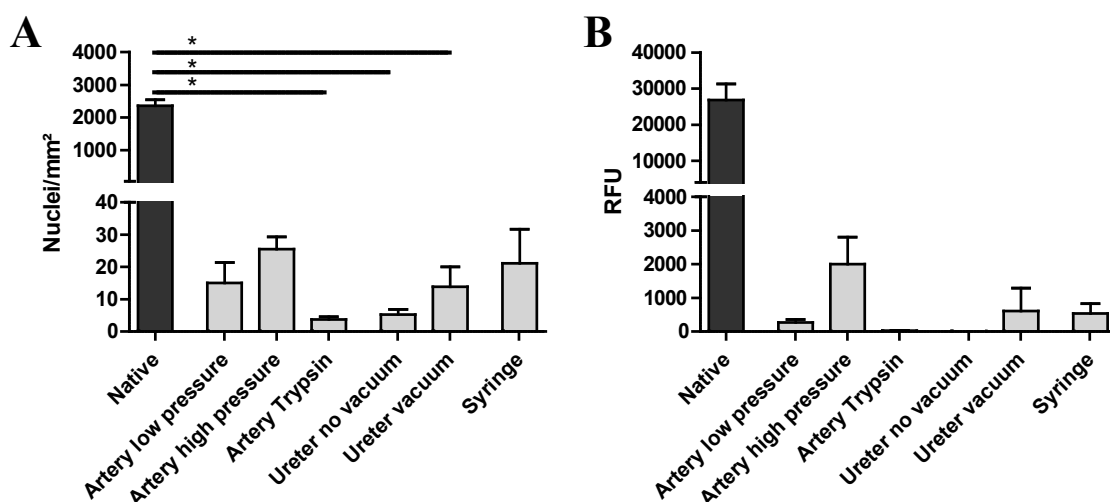


Figure 51: Quantitative analysis and comparison of seeding strategies. (A) RPCs were counted on DAPI stained sections of recellularized kidneys. Counted nuclei were normalized to the area of the analyzed images, to compensate for differing section sizes. (B) Resazurin assay quantification results given in relative fluorescence units (RFU). Viable cells reduced resazurin to the highly fluorescent resorufin. Best seeding results were achieved by seeding RPCs into the renal artery with high pressure. However, none of the seeding approaches reached cell densities or metabolic activities comparable to native organs. * indicates a significant difference in means, $p < 0.05$.

4.5 The effect of stiffness and ECM composition on renal progenitor cell maturation

The segment-specific architecture and ECM composition of the nephron create specific microenvironments for every cell type of the kidney. The decellularized kidney scaffold provides these site-specific architectural, mechanical and biochemical stimuli to the reseeded cells. In consideration of the theoretical impact of these factors on the phenotype and differentiation of cells, as described in 1.2.2, it was hypothesized that these microenvironments would promote full, site-specific maturation of the reseeded hiPSC-derived RPCs. Cells inside the kidney scaffold are exposed to a combination of all

these stimuli. To investigate the singular effect of any of these stimuli on RPC maturation, a parallel approach to the recellularization was established.

The effect of stiffness and ECM composition on RPC maturation was investigated on polydimethylsiloxane (PDMS), an easily moldable silicone with tunable elastomeric properties that can be coated with numerous ECM proteins.

First, the PDMS was optimized for RPC culture. Next, the effect of stiffness and ECM coating on RPC maturation was investigated.

4.5.1 Optimization of PDMS gels for cell culture

The elastic modulus of PDMS can be tuned by adjusting the ratio of the base and the curing agent. Three different PDMS mixtures were produced with elastic modules of 4 kPa, 189 kPa and 2230 kPa (Figure 52A).

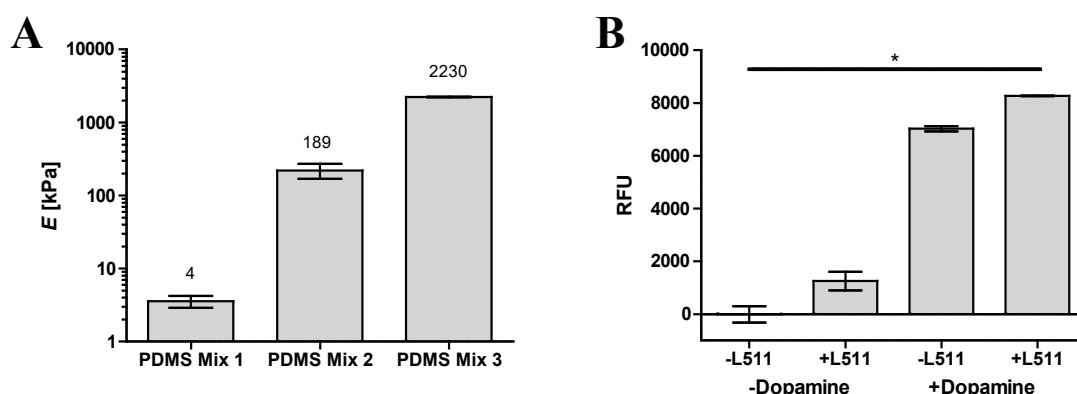


Figure 52: PDMS gel properties. (A) PDMS gels were produced from different Sylgard mixtures resulting in different stiffness, quantified by the E modulus. (B) PDMS is highly hydrophobic, therefore RPCs seeded on PDMS mix 1 cannot attach. Hence no metabolic activity in the resazurin assay was detectable. L511 coating alone could not improve the attachment sufficiently. Only dopamine pretreatment and L511 coating improved the attachment significantly.

PDMS is highly hydrophobic, without any pretreatment no RPCs can attach, resulting in no measurable metabolic activity in the resazurin assay. When PDMS was coated with laminin 511 the attachment and survival was only slightly higher. Earlier experiments with plasma treated PDMS did not yield in a reliable long-term cell attachment (data not shown). Therefore, the polydopamine coating was established as an alternative to the plasma pretreatment. The cell attachment improved drastically when PDMS was pretreated with

dopamine at pH 8,5. The polydopamine surface can be coated with ECM proteins. L511 coating on the polydopamine pretreated PDMS improved the cell attachment significantly (Figure 52B).

ECM coated, polydopamine pretreated PDMS was used for all further experiments.

4.5.2 Investigation of renal progenitor cell maturation

RPC maturation was investigated by differentiating RPCs into RTECs, as described in section 4.4.2. The effect of the stiffness of the culture surface on RPC differentiation was investigated by culturing the cells on PDMS with an *E* modulus of approximately 4 kPa, 200 kPa or 2 MPa. The effect of the ECM composition on RPC maturation was investigated by coating these PDMS culture surfaces with L511, L521, ColIV and mixtures of these three renal ECM components. As a control the standard RTEC differentiation on L521 coated TCPS was conducted. RPC maturation was assessed by morphological analysis and quantification of renal marker expression by qPCR.

Clearly stiffness and ECM coating both affected the cell morphology (Figure 53). Cells in all conditions exhibited an epithelial-like cell morphology comparable to the L521 TCPS control (Figure 44). Cells on 4 kPa PDMS showed brighter cell-cell connections in phase contrast than cells on 2 MPa. Cells on 2 MPa PDMS appeared bigger and with higher contrast. Also, cells in most conditions showed signs of deterioration, indicated by cytoplasmic vacuolation. Less cells survived on ColIV coated 4 kPa gels. The combination of L511, L521 and ColIV induced a similar morphology on 4 kPa gels and on 2 MPa gels.

Effects of stiffness and ECM-coating were also detected in the marker expression of RTECs (Figure 54). Aquaporin 1 (*AQP1*), a water channel protein on proximal tubular epithelial cells, was highly upregulated during RTEC differentiation. Interestingly, the *AQP1* expression was increasing with PDMS stiffness. Moreover, the coating had a clear impact on the *AQP1* expression. Both laminins supported a high expression, whereas ColIV coated cell culture surfaces yielded in a significantly lower *AQP1* expression. The highest expression was achieved on the stiffest PDMS coated with a mixture of L511, L521 and ColIV. The *AQP1* expression correlates with the cell morphology. Cells with higher *AQP1* expression displayed darker cell-cell connections in phase-contrast.

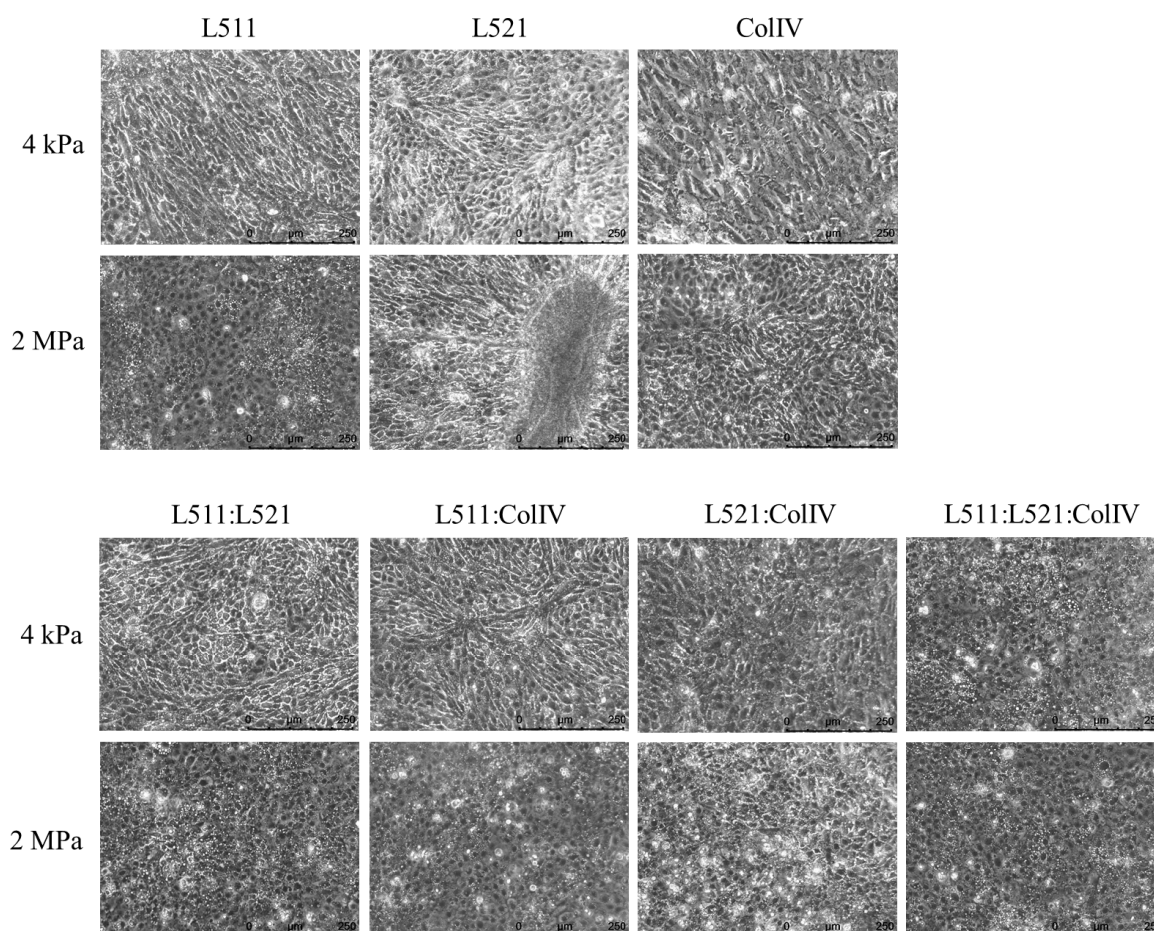


Figure 53: Renal tubular epithelial cell morphology on ECM-coated PDMS of 4 kPa and 2 MPa stiffness. Cells in all conditions exhibit an epithelial morphology. On 4 kPa PDMS cell-cell connections appear brighter in phase contrast than on 2 MPa.

The alpha subunit of the Na^+/K^+ -ATPase (*ATP1A1*), found in most renal tubular cells was highly expressed in RPCs as the ΔCt to the housekeeping genes is -10. The expression slightly decreased during differentiation. Neither stiffness nor coating of the PDMS had major impact on the expression. *ATP1A1* expression is therefore not a good marker for RPC maturation, since it is already highly expressed on the progenitor cell population.

Similarly, only low effects of stiffness and ECM on the expression pattern of the sodium-chloride symporter (*SLC12A3*), a marker on renal distal tubular cells, were detected. Notably, contrary to the *AQP1* expression, the podocyte markers podocalyxin (*PODXL*) and synaptopodin (*SYNPO*) were significantly higher expressed on 4 kPa PDMS than on stiffer PDMS gels. The ECM composition did not induce major *PODXL* expression differences. In contrast, *SYNPO* expression was decreased on ColIV coating. Wilms tumor protein (*WT1*), a transcription factor found in the glomerulus, was highest expressed in cells cultured on 200 kPa PDMS.

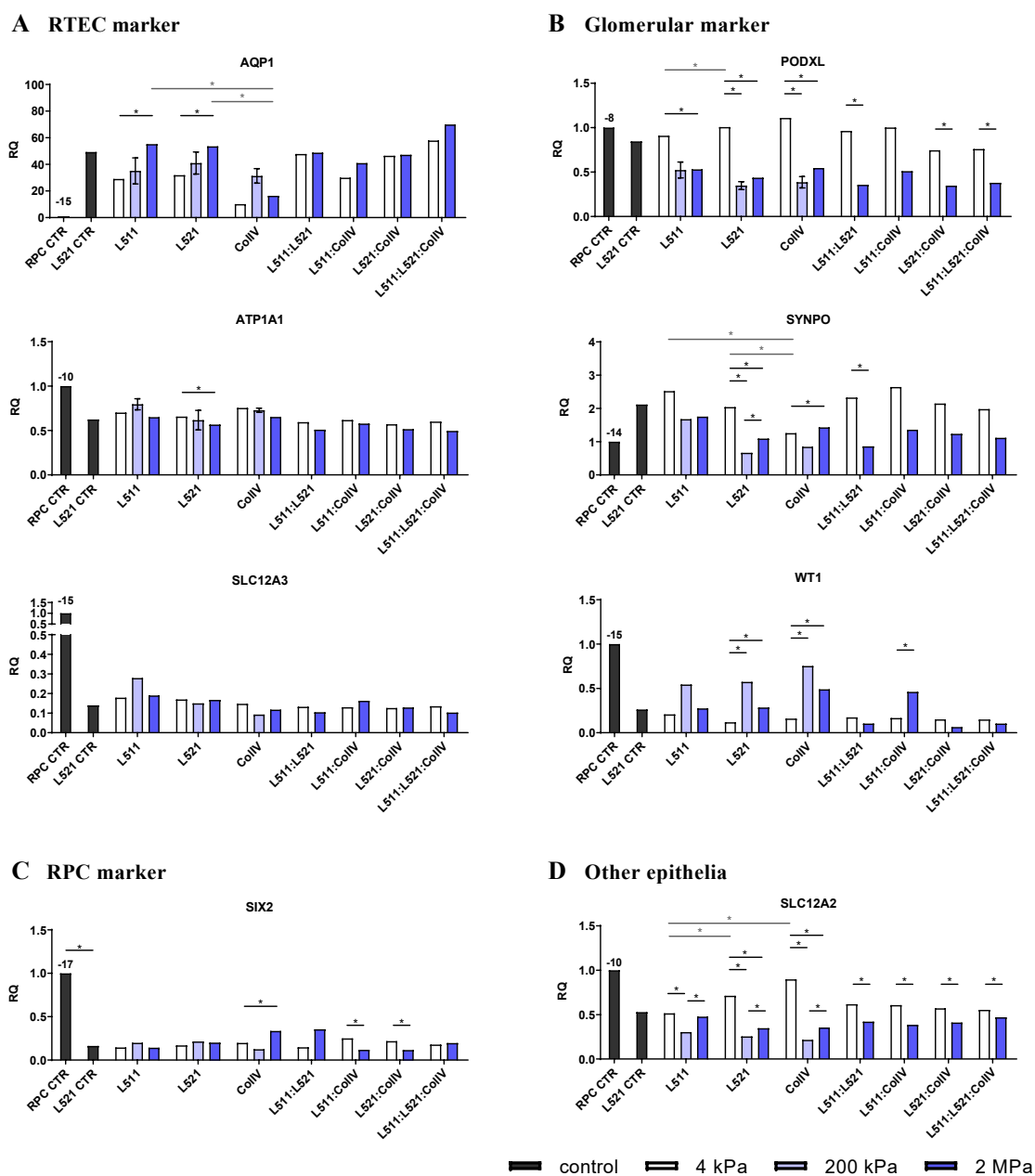


Figure 54: RPC and RTEC gene expression on ECM-coated PDMS of 4 kPa, 200 kPa and 2 MPa stiffness. (A) The RTEC marker AQP1 is highest expressed on stiff, laminin coated PDMS, (B) whereas the glomerular markers are highest expressed on soft PDMS. Stiffness provokes greater differences in marker expression than the ECM coating. Expression values are given as relative quantification (RQ) to the RPC control (RPC CTR). The numbers on top of the RPC CTR bars indicate the ΔC_t to the housekeeping genes. * indicates a significant difference in means between stiffnesses (black) or coatings (grey), $p < 0.05$.

The Na-K-Cl cotransporter 1 (*SLC12A2*) is not found in the kidney but throughout the body's exocrine epithelia. Its expression was influenced similar to the podocyte markers. Highest expression rates were detected in the lowest stiffness. Interestingly the expression on ColIV coated 4 kPa PDMS was significantly higher than on laminin.

SIX2 expression, a transcription factor active in renal development, decreases during RTEC differentiation, indicating a maturation of the renal progenitor cells.

5 Discussion

The aim of this thesis was to develop a human kidney model by decellularization of whole rat kidneys and recellularization of these ECM scaffolds with hiPSC-derived endothelial and renal progenitor cells.

A controllable perfusion bioreactor was developed that facilitates de- and recellularization of rat kidneys. A control software was programmed in LabView that allows constant control and monitoring of the bioreactor. Perfusion bioreactors as advanced as the one developed in this thesis are not commercially available and have not been used in any other published kidney de- and recellularization study.

A decellularization protocol was identified that balances effective cell removal and preservation of the ECM. The decellularized kidney is more than a simple scaffold that provides architecture and stability to the cells. It also provides important biochemical and mechanical stimuli.

As a next step, the decellularized vascular tree of the ECM scaffold was successfully reendothelialized. The recellularization of the parenchyma with RPCs, however, was very ineffective. Despite extensive testing, no recellularization strategy could be identified that repopulated the scaffold with the number and arrangement of cells that would be necessary to generate a human kidney model.

In parallel, a PDMS assay was established, to unravel how the biochemical and mechanical stimuli provided by the decellularized kidney affect RPC maturation. It was found that both substrate stiffness and ECM composition influence the maturation of renal progenitor cells into renal tubular epithelial cells and podocytes.

5.1 The perfusion bioreactor enables kidney de- and recellularization

The vascular tree of the kidney is naturally designed to ensure optimal supply of nutrients and oxygen to the entire organ as well as to provide perfusion through the nephron. The possibility to use that distribution system is a clear advantage of the de- and recellularization technique over any other kidney tissue engineering approaches to date. For example, the biggest hurdle for the organoid technology is currently the integration of a vascular network to improve nutrient and oxygen supply as well as to include shear forces into the model¹⁵⁰. By using whole kidneys, however, decellularization agents or cell culture medium can simply be perfused by a peristaltic pump via the cannulated renal artery through the vascular tree of the scaffold.

For this purpose, a perfusion bioreactor is required. Simple kidney perfusion bioreactors exist since the late 1970s, for *ex vivo* isolated perfused organ studies and are commercially available since then^{151,152}. Recently, this technique has been adapted for kidneys prior to transplantation. Hypothermic machine perfusion improved the graft survival significantly over simple cold storage^{153–155}. However, these commercially available bioreactors are designed for short term kidney survival, not for long term culture. They neither offer proper control over cell culture conditions nor facilitate cell seeding. Over the last years, numerous studies on whole organ recellularization have been published, most utilized a simple perfusion pump placed in a standard cell culture incubator^{148,156–159}. Others set up perfusion bioreactors that monitored the pressure and facilitated cell seeding^{123,160–162}. Only the minority of these studies used advanced perfusion bioreactors that automatically control pressure and pH and include a control software^{163,164}. However, none of these advanced perfusion bioreactors were applied in kidney de- and recellularization to date. In addition, these advanced bioreactors are not commercially available as they are all custom build.

Therefore, a perfusion bioreactor was developed that enables de- and recellularization of whole rat kidneys. It was designed to meet all requirements for long term organ culture. Accordingly, the developed perfusion bioreactor ensures sterility, temperature control, pH control, pressure control, non-invasive monitoring of cell viability and pO₂ and most importantly perfusion with cell culture medium, to provide nutrition and oxygen and to deplete excreted products.

The perfusion also provides mechanical stimuli to the reseeded cells that are necessary for maturation and functionality. In microfluidic chip experiments it was shown that physiological shear stress improves the phenotype of proximal tubular cells as it leads to enhanced polarization, glucose reabsorption and primary cilia formation^{165,166}. In contrast, slightly elevated shear stress resulted in dramatic damage to podocytes *in vitro*¹⁶⁷. *In vivo*, high blood pressure is a leading cause for kidney failure⁵. Moreover, high perfusion pressure might easily disrupt the decellularized scaffold. On the other hand, when the pressure in the renal artery drops below 60 mmHg, the renal perfusion decreases and the tissue is at risk of necrosis¹⁶⁸. The tight regulation of flow and pressure in the perfusion bioreactor is therefore an important aspect.

A control software programmed in LabVIEW enables the manual and automatic control of all crucial process variables. LabVIEW is a well-established programming language for process control applications. The code was structured as a queued state machine, a flexible and powerful producer consumer architecture that is one of the most frequently used design patterns in LabVIEW¹⁶⁹.

In the perfusion bioreactor, pressure control was realized by adjusting the pump speed. In a step response experiment the process was identified as a first-order system (PT_1 element) with a mean time constant of 4 s. The pressure reacts to the pump speed change without any dead time, but the new steady state is only reached with a delay. This delay can be explained by the time the pump needs to accelerate or a slight dilation of the kidney.

To guarantee optimal process control, the choice of the controller type and tuning parameters is of utmost importance and is in most cases a compromise between slow but stable and dynamic but instable controller behavior. It also needs to be kept in mind that the decellularized kidney scaffolds are natural products, hence, each kidney differs in its arterial branching morphology and other morphologic characteristics¹⁷⁰. Thus, every tested kidney responded differently in the step response. The controller was tuned in a way that it worked for all kidneys likewise. In the reference-variable response and the disturbance response it was shown that the PI controller tuned after the KUHN rules¹⁴⁷ handles the pressure control satisfactory.

On this basis a pulsatile flow profile could be implemented to mimic the fluctuating blood pressure in the human body¹⁷¹.

The pH in cell culture medium is regulated via a bicarbonate buffer and CO₂ gassing. In static cell culture the medium is normally gassed with 5 % CO₂ to adjust the pH to 7.4, the same pH as blood¹. In order to react to pH disturbances such as the secretion of acidic metabolites, it is necessary to dynamically adjust the CO₂ concentration in the bioreactor. Additionally, pH control enables modelling of alkalosis or acidosis and investigations on how these affect renal tubular epithelial cells (RTECs), which are responsible for the acid-base homeostasis¹⁷². Therefore, the pH control was implemented in the perfusion bioreactor. The pH control was realized by adjusting the CO₂ concentration in the oxygenator. The step response characterized the process as a second-order system (PT₂ element). It is defined by a delayed reaction composed of the process dead time that varies between 9 and 15 min and the process time constant that adds another 9 min. The dead time is caused by the time the CO₂ needs to diffuse through the silicone tubing into the medium in the oxygenator, plus the time the medium needs to travel from the bioreactor through the oxygenator to the sensor, which can vary according to the pump speed and the tube length. The ratio of the process time constant and the process dead time is a measure for the controllability of the system. It defines the pH control in the perfusion bioreactor as hardly controllable.

Despite this hurdle, a PI controller was tuned that sufficiently controls the pH for smaller disturbances that appear during normal metabolic activity. For strong sudden disturbances, the control settling time lies between one and two hours. Therefore, it is advisable to pre-gas the medium with CO₂ before medium changes to avoid drastic pH drops.

The same setup that is used for CO₂ control, including the gas mixing device and the oxygenator, provides the basis for the control of oxygen levels in the culture medium. Moreover, a pO₂ sensor is integrated into the perfusion circuit. In future, the control software can easily be expanded to enable oxygen control and to facilitate thus the investigation of hypoxia on the kidney model.

Electrical or mechanical stimulation, such as stretching, are beneficial for lung¹⁷³ or heart^{163,174} recellularization cultures. However, the kidney is naturally not exposed to these stimuli and it was therefore not necessary to implement these stimuli into the perfusion bioreactor for the kidney.

5.2 Kidney decellularization

Decellularization is the removal of cellular material from a cell culture, tissue or whole organ by a series of physical and chemical treatments. Applications of decellularized ECM scaffolds range from *in vitro* applications in basic research that address questions of cell-matrix interactions, disease or tissue development and regeneration, up to clinical applications of the scaffolds as such or after recellularization^{27,127}. An optimal ECM quality is of utmost importance for all these applications, the aim was therefore to identify a decellularization protocol for kidney tissue that maximizes cell removal and minimizes ECM loss and damage.

Several strategies for decellularization of kidney tissue cubes by immersion and agitation^{149,175} and decellularization of whole kidneys by perfusion^{123,144,156,157,162} have been published in the last years. However, all these protocols use SDS, which is known to disrupt protein structures and to dissolve some ECM components^{127,129}. Moreover, most of these manuscripts lack the comparison between multiple decellularization conditions. Furthermore, in studies that did compare multiple conditions, it is mostly impossible to identify the isolated effect of a specific protocol step on the scaffold quality. Systematic, controlled studies that compare multiple decellularization protocols in their cell removal efficacy and their effect on the ECM scaffold composition and biocompatibility are missing. Therefore, a comprehensive comparison was carried out in this thesis, to identify the optimal protocol for kidney decellularization.

5.2.1 The decellularization scoring system standardizes the evaluation of decellularization results

A standardized, unbiased evaluation of the ECM scaffolds and the definition of critical parameters for scaffold quality become increasingly important as the field moves towards clinical application. Results from histology, composition and biocompatibility analysis of decellularized ECM scaffolds represent qualitative and quantitative data and often underlie subjective success criteria.

The scoring system developed in this study is the first attempt to standardize the quality assessment of decellularized ECM scaffolds. It condenses qualitative and quantitative results into normalized scores. Therefore, it provides the opportunity to carry out intra- and

inter-study comparisons of decellularization strategies and ECM scaffold quality. Designed as an easily scalable system it can be expanded by additional parameters and categories. Depending on the application, scoring weights can also be modified. Analysis of tissue-specific parameters in the three primary categories histology, composition and biocompatibility is mandatory to derive a reliable quality score. For example, the biocompatibility scores for cell attachment and viability were not directly predictable from the scores of the other parameters. When a clinical application of the ECM scaffolds is considered, the scoring system can be easily extended with a category for clinically relevant data, such as immune compatibility. In this study, the system was applied to decellularization of kidney tissue; however, it is equally suitable for other tissues. Furthermore, the scoring system supports the identification of critical parameters by summarizing and visualizing study outcomes. A template of the scoring table was provided to the international research community as an interactive Excel sheet in Fischer et al. 2017¹⁷⁶.

5.2.2 The effect of the detergent on kidney decellularization by immersion

Immersion and agitation technologies for decellularization of tissues are useful to screen and compare decellularization protocols. This method was applied to porcine kidney tissue to compare the isolated effects of the detergents SDC, SDS and TX-100. Theoretically, mild, non-ionic detergents, such as TX-100, are the most desirable detergents to preserve the ECM during decellularization. However, especially for decellularization of dense organs like kidneys, non-ionic detergents might not be strong enough to remove the cells. Mild, ionic detergents, such as SDC, might provide a solution but have not been investigated thoroughly^{126,127}.

Cell lysis was provoked in 0,125 cm³ porcine kidney cubes by freezing and thawing and subsequent osmotic shock by diH₂O treatment. The samples were then immersed in 1% SDC, 1% SDS or 1% TX-100 for 7 to 10 days under constant agitation to solubilize and remove cellular debris. Lastly, the samples were extensively washed to remove any residual detergent and analyzed for cell removal and architectural integrity by histology.

Histological analysis revealed that TX-100 only removed a fraction of the cellular material; it is therefore not suitable as sole detergent for kidney decellularization. TX-100 is a non-ionic detergent. With an HLB of 13,5 its uncharged hydrophilic head group and

hydrophobic tail, TX-100 can break lipid–lipid and lipid–protein interactions. It dissolves cell membranes and membrane proteins by association with their hydrophobic parts, a micelle-like interaction that mimics the lipid environment of the protein and thereby even supports its continued activity. However, TX-100 cannot dissolve protein-protein interactions. It neither penetrates into proteins nor denatures them^{127,129}. Therefore, it is clear that TX-100 hardly penetrates through the porcine kidney cube, as it was confirmed in other studies^{144,156,177}. Surprisingly, three other studies on kidney immersion-decellularization reported successful decellularization with TX-100. In these studies, however, the immersed tissue pieces were smaller and the detergent was applied in higher concentration, or for up to two weeks^{149,175,178}. In general, TX-100 is only suitable, when applied during decellularization of thin tissues, such as heart valves¹⁷⁹.

Immersion with SDS at 4 °C resulted in completely decellularized tissue. SDS is a strong ionic detergent with an HLB of 40. It not only disrupts cell membranes forming mixed micelles, its monomers also bind cooperatively to proteins, which are thereby forced into drastic conformational changes and denaturation. Hence, SDS is effective in dissociating protein-protein interactions and solubilizing cytoplasmic compounds^{127,129}. SDS is widely used as a decellularization agent, due to its excellent cell clearing properties.

Also, the SDC 4 °C samples were predominantly cleared of cellular material. However, small zones with DAPI stained cellular debris were still observable. A DNase digest was added after the detergent treatment that reduced the total DNA amount drastically. Although SDC is categorized as an ionic detergent, it has an HLB of 16. Its hydrophilic properties and behavior are therefore much closer to TX-100 than to SDS. Comparable to TX-100, SDC does not induce protein denaturation. This complements its natural function as a bile acid in the gut, where it dissolves lipids to assist fat digestion^{129,180}. However, the ionic head group explains the better cell removal efficiency of SDC than TX-100.

The composition analysis of decellularized ECM scaffolds is challenging. ECM proteins are essentially insoluble in standard detergent based lysis buffers as they have a high molecular mass and are abundantly covalently cross-linked. Exactly this property is utilized in decellularization but hinders the proteomic analysis. Dot blot and western blot analyses (data not shown), did not result in robust quantifications. Mass spectrometry approaches face the same hurdles. Only very recently, a chemical digestion with hydroxylamine for insoluble extracellular matrix characterization was identified¹⁸¹. Hence, in this study the composition

was analyzed by immunofluorescent staining of ECM proteins, bulk collagen and GAG quantifications, as well as enzyme-linked immunosorbent assay (ELISA) for bFGF and VEGF.

Decellularization with SDS resulted in slightly higher collagen content per dry weight than with SDC, though the difference was not significant. This finding is probably due to a higher fraction of cellular remnants in the dry weight of SDC-decellularized scaffolds and not due to the removal of collagen by SDC, since SDC as a mild detergent cannot dissolve highly crosslinked collagen molecules. The normalization to dry weight after decellularization impedes the clear interpretation of the quantification results if the samples still contain a considerable amount of cellular debris. However, it is the gold standard in decellularization studies to date^{123,149,156}. In future, it would be advisable to normalize quantification results to wet weight of the tissue samples before decellularization instead, to facilitate the comparison of absolute quantification results.

Also, decellularization with SDS resulted in a higher GAG per dry weight ratio than SDC treatment. On the contrary, the cytokines bFGF and VEGF are much better preserved with SDC than with SDS. Both cytokines are mainly bound to the ECM by GAGs. Therefore, it seems that although SDC removes GAG chains from the scaffold, it does not strip the cytokines from the remaining chains. On the other hand, SDS might not deplete the GAG chains, but denature or remove the bound cytokines.

The data from recellularization with human iPSC-derived intermediate mesoderm cells¹¹³ suggest that the cytokines retain their biological activity after SDC treatment, since the SDC treated samples harbor the highest levels of growth factors and achieved the best results for cell attachment and viability. No negative effect of minor cellular remnants was observed in the recellularization experiment. Moreover, the recellularization data indicate that high GAG and total collagen contents do not sufficiently predict cell performance in decellularized ECM. A test for biocompatibility should therefore always be included in the evaluation of decellularization strategies.

SDS-decellularized scaffolds have an increased stiffness in comparison to SDC-decellularized scaffolds, quantified by measuring the *E* modulus, which again is an indication of alterations and denaturation in the SDS-treated ECM.

In conclusion, the initial hypothesis that SDS treatment produces ECM scaffolds of minor quality was confirmed for decellularization of porcine kidneys by immersion. SDC-decellularization leads to more native, biologically active porcine kidney scaffolds.

5.2.3 The effect of the temperature on kidney decellularization by immersion

Cell lysis during decellularization disrupts cellular compartments and releases endogenous proteases and nucleases¹²⁷. In earlier studies, Nakayama et al. observed better structural conservation at 4 °C than at 37 °C during decellularization of rhesus monkey kidneys by immersion in SDS¹⁷⁵. Moreover, Higami et al. described higher collagen levels at 4 °C in the decellularized carotid artery¹⁸². It was thus hypothesized that low temperature during decellularization improves the conservation of cytokines and other functional ECM components. To evaluate this hypothesis, decellularization was conducted at 4 °C, RT and 37 °C.

Decellularization with SDC or SDS at 4 °C resulted in much higher preservation of the tissue architecture and improved cell removal compared to RT or 37 °C. RT and 37 °C samples showed cellular residues especially in the core of the tissue cube, whereas the peripheral area was decellularized, but the ECM structures were collapsed. In accordance to that, decellularization approaches using TX-100 led to better results in cell removal at 4 °C than at RT or 37 °C.

In immersion-decellularization, the peripheral zones of the tissue cubes are naturally exposed the longest to the detergent. Therefore, ECM damage is highest in these areas. When the damage is too severe the structures collapse and block the tubes and vessels through which the detergent can penetrate through the cube, leaving the cores undecellularized. Two possible modes of action increase the damage at RT and 37 °C in comparison to 4 °C. Firstly, the Brownian molecule movement increases with temperature and enhances the action of the detergent¹⁸³. Secondly, the activity of human enzymes rises with increasing temperature, peaking at 37 °C¹⁸⁴, resulting in a higher activity of endogenous proteases. Proteases, such as MMPs¹⁸⁵⁻¹⁸⁸, digest the ECM, resulting in collapsed peripheral areas. This theory is supported by the finding, that the content of the proteins collagen, bFGF and VEGF decrease in the decellularized scaffolds with increasing temperature.

DNA levels decrease with increasing temperatures in SDC, but increase in SDS samples, when the tissue cubes are not treated with DNase. This effect cannot be solely explained by

higher detergent action at higher temperatures because the DNA levels do not correlate with the amount of remaining cellular material. Again, a higher enzyme activity, in this case of nucleases, is the most probable explanation for the decreasing DNA levels with increasing temperature. SDS treatment, however, might denature the nucleases. After DNase treatment, no differences in DNA levels are observable anymore. Ross et al. even utilized these endogenous nucleases by activating them during decellularization by perfusing rat kidneys with calcium chloride and magnesium sulfate¹⁶².

Summarizing, higher temperatures activate endogenous enzymes that are released during cell lysis. Nuclease activity supports the decellularization process, however, protease activity harms the ECM. Decellularization at 4 °C therefore results in better ECM and cytokine preservation, but in higher DNA levels. Since the preservation of ECM structure and composition is crucial for later applications of the scaffold, the decellularization by immersion should be carried out at 4 °C. Lower DNA levels can be achieved by adding a short DNase digestion step at 37 °C after detergent treatment. This prevents the necessity of performing the whole decellularization at 37 °C for several days.

5.2.4 Decellularization outcomes by perfusion differ to decellularization outcomes by immersion

Whole organ decellularization is the basis for whole organ tissue engineering. The vascular tree of the organ can be utilized to perfuse the decellularization solutions through the organ. Porcine kidneys are the ideal basis for kidney tissue engineering for transplantation, due to their similar size compared to human kidneys. Rat kidneys, however, are superior for the generation of human 3D kidney models, as they require less cells and reagents for recellularization.

The best condition identified for decellularization of porcine kidney tissue by immersion and agitation, 1% SDC at 4 °C, was therefore tested in whole organ perfusion-decellularization of rat kidneys. Additionally, an already published protocol for perfusion-decellularization of rat kidneys by Song et al.¹²³, based on perfusion at RT with 1% SDS and 1% TX-100, was applied as comparison. Both protocols were conducted at 4 °C and RT.

The experiments showed that SDC is not suitable for perfusion-decellularization of whole rat kidneys. Perfusion with SDC at 4 °C did not completely remove cells and DNA from the ECM. Increasing the temperature to RT led to better, albeit still incomplete decellularization, and to less remnant DNA. Hence, the observations of immersion-decellularization regarding the temperature were confirmed. Perfusion with SDS/TX-100 resulted in complete decellularization and architectural integrity at 4 °C and RT.

Biocompatibility was tested by injecting HUVECs into the renal artery of scaffolds that were decellularized at RT with SDC or SDS/TX-100. SDS/TX-100 RT scaffolds support higher cell viability than SDC scaffolds, as shown by histological and metabolic analysis. Remaining cell debris inside the SDC scaffold possibly hampered perfusion and therefore the nutrient supply. Moreover, the cell debris could be a reservoir of residual detergents that harmed the reseeded cells, or the cell debris itself had a negative effect on the cells^{189,190}. The SDS/TX-100 RT protocol was therefore chosen for all subsequent whole organ recellularization experiments.

The question arises, why the immersion-decellularization protocol cannot be transferred to perfusion-decellularization.

Firstly, cell lysis in perfusion-decellularization was not preceded by freezing, thawing and osmotic shock, as it was carried out with the immersion samples¹²⁷.

Secondly, immersion-decellularization was optimized with porcine kidneys, while rat kidneys were used for perfusion-decellularization. As pointed out in 1.3.2, the general architecture of mammalian kidneys is conserved, however, the tubules and glomeruli are smaller in rat than in pig. Rat renal tubules have a mean radius of 29 μm ^{121,122}. The spherical SDS micelles have a radius of only 1,5 nm¹⁹¹. Bile salts form even smaller, disc-shaped micelles^{129,192}. Hence, tubule size is not the direct problem. However, the fluidics for the transport of decellularization agents and cell debris changed, amplified by the different techniques the decellularization agents were delivered with^{193,194}.

Lastly, the detergents were applied for 168-240 h in immersion-decellularization, but only 16 h or 120 h for SDS or SDC in perfusion, respectively. Perfusing the detergents through the vascular tree has the advantage of their highly effective distribution. Therefore, the exposure to SDS can be drastically shortened in comparison to immersion-decellularization, which resulted in less damage to the scaffold. In the study by He et al. it was confirmed that shorter SDS incubation leads to improved kidney scaffold characteristics¹⁴⁸, as clearly

visualized by the scoring system. For SDC, however, the shorter incubation time limited the clearing of the tissue. To prolong the SDC treatment further is logistically not feasible, as perfusion-decellularization is a low-throughput system.

Conflicting results regarding the effects of SDS and SDC on decellularization have also been described in literature¹²⁶. SDC was successfully applied in the decellularization of heart valves^{195,196} or liver^{177,197,198}. For kidney perfusion-decellularization, however, Wang et al. concluded that SDS is the preferred detergent over SDC¹⁷⁷. Ross et al. decellularized rat kidneys with 4% SDC and 1-10% TX-100 and found that although a higher SDC concentration increases the cell removal efficiency, it still leads to inconsistent decellularization results¹⁶². In this thesis, further inter-study comparisons for kidney perfusion-decellularization data were conducted by applying the scoring system to data from He et al.¹⁴⁸ and Caralt et al.¹⁴⁴. These comparisons confirmed that SDS is necessary for perfusion-decellularization of kidneys. Moreover, it was shown that a low SDS concentration of 0,125% is favorable over higher concentrations.

In conclusion, the optimal conditions for kidney decellularization by immersion and agitation are not transferable to perfusion. As a result of the comparison conducted in this study, SDS appears to be the only detergent that effectively decellularizes organs with a high cell density, such as the kidney, in perfusion conditions. To reduce the inevitable damage to the ECM by SDS, the conditions of SDS exposure should be carefully chosen. Altogether, SDS applied at low concentration, for a relatively short period of time and at a low temperature is advisable.

SDC preserves a more native kidney ECM composition than SDS, but because SDC is less effective in clearing tissues from cellular material, it can only be applied for decellularization of thin tissue slices or tissues with low cell densities. Also, when a decellularization technique is applied that requires long exposure to the decellularization agents, milder detergents, such as SDC, should be preferred.

5.3 Generation of an *in vitro* kidney model by recellularization of decellularized kidneys

When decellularized kidney scaffolds are transplanted, they are not simply repopulated with resident cells *in vivo*. It was shown that cells only scarcely migrate into decellularized kidney scaffolds that were surgically implanted into a kidney^{178,199}. It is therefore necessary to recellularize these scaffolds with human cells *in vitro*. To generate a 3D human kidney model from decellularized whole rat kidneys, an adequate cell type and cell number has to be seeded and the cells have to integrate into the scaffold at the correct position.

5.3.1 Successful reendothelialization of the renal vascular tree

The kidney contains three main endothelial cell (EC) populations, each with distinct phenotypes and functions. ECs in medium and large vessels form a continuous layer. Especially in arteries the cells are elongated in the direction of the blood flow. Glomerular endothelial cells, part of the glomerular filtration barrier, are highly fenestrated and covered by a thick glycocalyx. The endothelial cells of the peritubular capillaries are also fenestrated and specialized in the reabsorption of solutes from the adjacent tubules^{200,201}. The incorporation of ECs is thus compulsory for a functional kidney model. Furthermore, transplantation without a fully repopulated vascular tree triggers blood coagulation even with anticoagulation treatment, shown in transplantation studies by Orlando et al. and Baptista et al.^{202,203}. Reendothelialization of the renal vascular tree is therefore an important step in recellularization.

Human umbilical vein endothelial cells (HUVECs) are primary ECs and a commonly used *in vitro* experimental system as they are easy to culture and highly proliferative^{204,205}. Therefore, HUVECs were seeded into the renal artery of the decellularized kidney and cultured under perfusion for three days. The perfusion bioreactor successfully supported their viability as the cells showed metabolic activity over the whole culture period. After three days, the seeded HUVECs lined the large vessels and capillaries, comparable to the vessels of native kidneys. However, the fine structure especially in the glomerular capillaries was not as delicate as in native kidneys. HUVECs, as a venous EC type, might not be the

best cell type to repopulate these capillaries. Wolburg et al. showed that although HUVECs were able to form fenestrations *in vitro* after VEGF stimulation, the magnitude of their response to that stimulation was much weaker than in ECs that were isolated from fenestrated capillaries²⁰⁶.

hiPSC-derived cell types often only reach a fetal phenotype in classical 2D cell culture¹⁰¹. Hence, hiPSC-derived ECs are more plastic than HUVECs and can potentially mature inside the decellularized scaffold.

Several protocols for EC differentiation from hiPSC have been published^{142,207,208}. The protocol by Patsch et al. was chosen in this thesis because it is fast, reliable and highly efficient¹⁰⁹. After mesoderm induction, the cells specify into ECs. 98% of the differentiated cells are double positive for CD31 and CD144, EC marker proteins that are part of the junctional mechanosensory complex²⁰⁹.

Special focus was laid on the mass expansion of hiPSC-derived ECs, since millions of cells are needed for recellularization. The highest proliferation rate, stable endothelial marker expression and cost-effectiveness was achieved in an expansion medium composed of a commercially available endothelial cell culture medium supplemented with 20% FCS and a transforming growth factor β (TGF β) inhibitor that has been shown to maintain the proliferation and vascular identity of ESC-derived ECs^{141,210}.

hiPSC-derived ECs were seeded via the renal artery into the decellularized kidney. They successfully reendothelialized the vascular tree, since in histology, ECs were found to line the large vessels, but also the capillaries. The results were comparable to the HUVEC experiments, although less cells were detected, and to studies by Song et al.¹²³ and Caralt et al.¹⁴⁴.

To date, no kidney recellularization study proved the development of endothelial fenestrations or the endothelial barrier function. However, an extensive reendothelialization study in lung hinted that kidney reendothelialization could be further improved by fibronectin coating of the decellularized vessels, combined arterial and venous seeding, co-seeding of ECs with mesenchymal cells and longer perfusion culture in FCS reduced medium¹⁴¹.

5.3.2 Inefficient recellularization of the renal parenchyma

hiPSC-derived renal progenitor cells were chosen for the recellularization of the decellularized kidney parenchyma as they are proliferative and can differentiate into a broad spectrum of highly specialized kidney cell types. It was hypothesized that the scaffold's architecture, mechanical properties, segment-specific ECM composition and the perfusion culture would induce site-specific maturation of the RPCs, leading to a native-like cell arrangement and to a functional tissue engineered kidney model.

Renal progenitor cells were differentiated from hiPSCs according to a protocol established in our lab¹¹⁷. hiPSCs exposed to Activin A, BMP4 and retinoic acid for four days differentiate into intermediate mesoderm cells. These develop further into renal progenitor cells after a four-day GDNF treatment. The differentiation is highly efficient as 70-80% of the cells express SIX2 at day 8. SIX2 is a transcription factor characteristic for the cap mesenchyme, which is the tissue the nephron develops from. The generated RPCs can be further directed into various renal cell types including mesangial, proximal tubular, distal tubular and collecting duct epithelial cells as well as into podocyte precursors^{117,211}. RPCs were injected into the decellularized kidney scaffold and cultured for 6 days under perfusion conditions.

RPCs injected into the renal artery did not migrate from the vascular compartment into the parenchyma as already observed in the reendothelialization experiments. Caralt et al. published an arterial high-pressure seeding approach. Their work was based on a highly proliferative, immortalized, human renal tubular epithelial cell line that achieved the highest cell density in recellularized rat kidneys published to date¹⁴⁴. Application of this method resulted in a higher RPC seeding efficiency but damaged the scaffold. A short trypsin digest of the vascular tree that was expected to facilitate cell migration from the vascular compartment into the parenchymal compartment, did not improve the seeding efficiency. The vascular compartment is separated from the parenchyma by the ECM of the vessels. Glomerular and peritubular capillaries are only covered by a thin basement membrane, but the bigger arteries and veins are surrounded by robust ECM layers²¹². Without an attractant, the cells will not take on the tremendous effort to migrate through these structures.

Similarly, cells seeded by injection into the parenchyma with a syringe did not migrate into the surrounding tubular structures. Moreover, the scaffold structure was disrupted by the punctures.

Injecting the cell suspension into the ureter dilated the renal pelvis and compressed the renal papilla, indicating that the cell suspension could neither penetrate into the collecting ducts, nor further up the nephron. Applying vacuum as published by Song et al.¹²³ only slightly improved the RPC seeding efficiency.

Coming from the ureter, the nephron is a liquid filled dead end, sealed by the glomerular basement membrane at the end. Although decellularized ECM is permeable for liquids²¹³, the injected suspension cannot drain fast enough and dilates the pelvis instead. Moreover, the tubules in the rat kidney have an average diameter of only 29 μm ¹²¹. Notably, a paper on bioprinting proximal tubules confirmed recently that seeding cells into channels below 200 μm in diameter is very challenging¹¹¹. Hence, the complex architecture of the kidney makes cell seeding into the scaffold highly inefficient.

Moreover, in contrast to the reendothelialization, all approaches to recellularize the parenchyma with RPCs resulted in a very low number of attached cells, low viability, low metabolic activity and detectable cellular debris, hinting at a high sensitivity of hiPSC-derived RPCs.

Sensitive cell types could be harmed by traces of residual decellularization agents, as it was shown that these exert a toxicological effect on reseeded cells^{189,190}. Although decellularized tissues have been extensively washed after detergent treatment, White et al. were able to detect residual fragments of TX-100, SDC and SDS in decellularized urinary bladder matrix²¹⁴. In the here applied SDS/TX-100 perfusion-decellularization protocol, SDS is efficiently removed from the scaffold by the TX-100 perfusion step^{129,177}. However, traces of TX-100 could have been still be present in the scaffold and harmed the RPCs.

Shear stress during seeding and perfusion culture is another potentially damaging factor. Endothelial cells are naturally exposed to high shear stress. Epithelial cells of the kidney are naturally exposed to much lower shear stress. It is therefore a wrong assumption to perfuse a not fully reendothelialized scaffold with the same shear stress or flow rate that it would withstand in the native form. Caralt et al. perfused recellularized rat kidneys with 4 ml/min and did not observe any shear stress induced damage to the seeded immortalized RTECs¹⁴⁴, although they applied the same flow rate as found in rat kidneys *in vivo*^{215,216}. In this study,

the cells were seeded into the scaffold with 2 ml/min and the recellularized rat kidney was perfused with approximately 0,5 ml/min. Thus, although shear stress was deliberately minimized in this thesis a damaging effect on the RPCs cannot be excluded, especially in the syringe seeding experiments.

Lastly, a deficient supply with nutrients or oxygen could have provoked cell death in RPCs. Arterially seeded HUVECs were located in the vascular tree and therefore had a direct supply of nutrients and oxygen. RPCs seeded into the parenchyma relied on diffusion of nutrients and oxygen through the scaffold.

In conclusion, none of the seeding strategies resulted in successful recellularization of the kidney scaffold. Two possible reasons are the complex architecture of the kidney, which is characterized by narrow tubules that end in dead ends, and the sensitivity of the hiPSC-derived RPCs. Neither the cell number, nor their position and arrangement were comparable to the conditions in the native organ. Even the most efficient seeding strategy only yielded in 1% of the cell density found in rat kidneys. Moreover, the cells did not arrange in epithelial structures, but were rather scattered throughout the scaffold. Since the function of the kidney is highly dependent on its structure, the recellularized scaffolds are not functional. Due to these poor results, the analysis of the site-specific cell maturation, was not possible.

Song et al. published in 2013 a promising paper on de- and recellularization of rat kidneys. The bioengineered kidney was produced by seeding primary rat neonatal kidney cells with vacuum support into the ureter of decellularized rat kidney. Song et al. stated to have engineered a matured functional kidney construct that excretes rudimentary urine. This raised the hope of rapid progress in whole organ kidney tissue engineering and fast clinical translation and laid the base for this thesis¹²³.

Since then, several kidney recellularization studies from other groups followed. Only one study has reported the repopulation with hiPSC-derived RPCs¹⁵⁹, all other studies have used inadequate cell types for kidney tissue engineering, such as pluripotent stem cells, immortalized cell lines or primary renal cells of animal origin. Notably, all these studies, including the above-mentioned work from Song et al.¹²³, were facing the same problems that were also observed in this study. In general, only fractions of the scaffold were repopulated in all studies, even when highly proliferative cell types, such as immortalized RTECs¹⁴⁴ or ESCs^{157,162,217}, were seeded. The cells were not uniformly distributed but confined to focal

areas. Moreover, the cells did rarely arrange in a native-like morphology. Cells were either scattered over the scaffold or cell masses clogged glomeruli and tubules. Recently, Remuzzi et al. compared several published recellularization strategies, similar to this study, by seeding mouse ESCs and confirmed the here described findings²¹³.

Since all the above-mentioned studies worked with different bioreactor setups, cell sources and seeding conditions, the architecture of the scaffold seems to be the common, fundamental problem of kidney recellularization.

Song et al. have not published a follow-up paper since 2013, instead their research focus was retrieved from kidney and transferred to lung and whole limb de- and recellularization^{106,218}. Furthermore, the Orlando group²¹⁹ and the Remuzzi group²²⁰, two well established research groups in the field of de- and recellularization, independently published two reviews recently. Both these reviews conclude that the recellularization of decellularized kidney scaffolds is still in its early stages and a seemingly impossible task.

It remains to be seen whether it will be possible to further develop the recellularization method in such a way that it enables the generation of a human kidney model.

5.4 Stiffness and composition of the cell culture surface influence renal progenitor cell maturation

Classically, hiPSC differentiation protocols rely on the variation of soluble factors in the cell culture medium. The influence of the ECM on cell differentiation is often disregarded, although its composition influences the chemical environment of the cells as well. Different ECM molecules bind to specific integrins, which trigger specific signaling pathways inside the cell. For example, cells seeded onto a laminin coated cell culture surface maintain an apical–basal polarity^{67,102}.

Moreover, changes in the mechanical environment influence the phenotype and differentiation of cells. Engler et al. demonstrated that the ECM elasticity, quantified as *E* modulus, directs the lineage specification of mesenchymal stromal cells. Matrices with an *E* modulus similar to brain tissue of 1 kPa were found to be neurogenic, whereas matrices with an *E* modulus of 100 kPa, were osteogenic²²¹.

The perfused decellularized kidney provides all these stimuli to the reseeded RPCs. To study the isolated effects of stiffness and ECM composition on RPC maturation a parallel approach to the recellularization was established.

hiPSC-derived RPCs were seeded onto PDMS gels with E moduli of 4 kPa, 200 kPa or 2 MPa. The gels were coated with L511, L521 and/or Col (α 1)₂ α 2 (IV), three typical components of the tubular and glomerular basement membranes in the kidney³¹. The cells were cultured for six days in renal epithelial cell growth medium, corresponding to the standard 2D protocol to differentiate RPCs into renal tubular epithelial cells¹¹⁷. The *SIX2* expression decreased significantly during these six days, corroborating the ongoing RPC maturation.

The E modulus of the culture surface showed a clear effect on the differentiation. The *AQP1* expression, a marker for RTECs, increased with the stiffness of the culture surface. Whereas the expression of the podocyte markers *PODXL* and *SYNPO* decreased.

Interestingly, collagen IV coating resulted in the lowest *AQP1* expression. Laminin coating proved to be of much higher efficiency for RTEC differentiation than collagen IV. Narayanan et al. observed a similar trend in their differentiation towards proximal tubular cells²²².

L511 is part of the BM in all renal tubules, whereas L521 is solely expressed in the glomerular basement membrane. Although the β 1 and β 2 chain are structurally homologous, the null mutation of the β 2 chain leads to severe proteinuria, which is the leading symptom of Pierson syndrome. This supported the idea that the β 1 and β 2 chain must be functionally distinct and may affect the maturation of glomerular cells⁵⁰. However, the variation of the laminin β chain did not affect the RPC maturation. No significantly different marker expression patterns, nor morphological differences were identified between the L511 and L521 coatings. This finding is supported by the fact, that the laminin α chain defines, which integrin binds to the laminin trimer, not the β chain²²³. Moreover, Suh et al. demonstrated that the L511 trimer can replace the function of L521 in the GBM. The β 1 and β 2 chains are hence not functionally distinct. *In vivo*, however, β 1 cannot compensate for the loss of β 2 since its expression is downregulated in podocytes. Therefore, the severe phenotype of the Pierson syndrome is provoked by a loss of laminin in the GBM in general. The GBM is

impaired, not the maturation of the cells of the glomerular filtration barrier. Suh et al.'s results corroborate our data and validate our model²²⁴.

The most beneficial condition to enhance renal progenitor cell differentiation into renal tubular epithelial cells is culturing the cells on a surface with an *E* modulus of 2 MPa that is coated with L511, L521 or any combination containing L521. The condition that induces preferably glomerular cells is culturing the cells on a surface with an *E* modulus 4 kPa that is coated with L511 or L521.

These findings prove that it is essential to provide the correct microenvironments to cells in order to generate a kidney model with mature renal cell types and will help to further improve differentiation protocols for RPC maturation.

6 Outlook

The numerous attempts presented in this thesis to recellularize decellularized rat kidneys did not lead to the generation of a human kidney model; however, firstly, the perfusion bioreactor that was developed in this thesis supports fully controlled perfusion culture and decellularization conditions, the decellularization techniques developed and tested in this thesis produce an ECM based scaffold of highest quality and these scaffolds were successfully reendothelialized. These technologies can be applied in many other research approaches.

And secondly, the insights gained in this study, on how difficult cell seeding into highly complex scaffolds is and on how to steer RPC maturation, will help to identify an alternative and ultimately successful kidney tissue engineering approach.

Alternative applications of the decellularized kidney ECM include the reseeded of sections of decellularized kidney tissue by immersion in a cell suspension. These can be applied as a simple, static model to investigate ECM directed cell differentiation, or the effect of diseased ECM on cells²²⁵.

The reendothelialization of decellularized kidneys can be applied to study the effects of ECM and perfusion on endothelial cells. Longer culture periods, pulsatile perfusion and co-seeding with smooth muscle cells and pericytes can be investigated in this system. The functionality of the endothelium should be verified by proving the impermeability to dextran and by visualizing the continuous and fenestrated endothelial cell morphologies with electron microscopy.

Furthermore, the decellularized ECM can be dissolved and used to form hydrogels or surface coatings. The composition of these hydrogels is much more diverse than mimicked in the PDMS assay in this study. Therefore, in future studies it is planned to coat the PDMS surfaces with the decellularized ECM to investigate its effect on RPC maturation. By separating glomeruli and tubules before decellularization it would be possible to generate nephron segment-specific hydrogels and to investigate whether the renal ECM promotes full, site-specific maturation of RPCs. Additionally, the PDMS assay was further developed into PDMS based geography chips to study the effect of surface curvature and geometry onto

RPCs. Concave and convex tubular and spherical structures of different sizes on these chips mimic the tubular and glomerular structures of the kidney. Preliminary results show that it is possible to steer the RPC maturation with the geometry of the culture surface.

In consideration of the experience gained in this thesis and the assessment of external studies on kidney de- and recellularization, alternative tissue engineering approaches for the generation of a human kidney model should also be considered.

3D bioprinting arranges cells, biocompatible materials and supporting components in complex 3D structures and could one day produce living, functional tissues. The dissolved, decellularized ECM can also be utilized as a bioink for 3D bioprinting. To date the resolution of bioprinters is not high enough to print a complex, vascularized kidney model, however, advances in this technology might facilitate this in the future²²⁶.

An alternative to bioprinting and probably the most promising non-scaffold-based kidney tissue engineering approach are strategies that rely on self-organization of cells.

Self-organization of cells *in vivo* is used in the blastocyst complementation method. This method could allow to grow human organs in pigs in the future. Currently, this technique is still in its early stages and human-animal chimeras face ethical concerns^{227,228}.

Self-organization of cells *in vitro* is used in the organoid technology. hiPSC-derived renal progenitors have been able to form tubular and glomerular structures inside organoids. However, as mentioned before, these structures are to date rather unorganized. The organoids lack organization since they are solely derived from a metanephric mesenchymal cell population. Recently it was shown that incorporating ureteric bud cells, which generate the collecting duct system and organize the kidney geometry, drastically improves these organoids^{229,230}. If research succeeds in engineering a vasculature in these organoids, for example by placing the organoids in the perfused, reendothelialized decellularized kidney, perfusion and cultivation in an advanced perfusion bioreactor, like the one developed in this thesis, could then mature these organoids into perfusable human kidney models or even into functional, fully grown human kidneys.

With the ongoing rapid improvements in renal hiPSC differentiation, tissue engineering techniques and bioreactor design, the successful generation of kidney models for preclinical testing and even of whole kidneys for transplantation might become reality within the next decades. The findings of this thesis are an important step towards achieving this goal.

7 References

1. Schmidt, R. F., Lang, F. & Heckmann, M. *Physiologie des Menschen*. (Springer Berlin Heidelberg, 2007). doi:10.1007/978-3-540-32910-7
2. Romagnani, P., Lasagni, L. & Remuzzi, G. Renal progenitors: an evolutionary conserved strategy for kidney regeneration. *Nat. Rev. Nephrol.* **9**, 137–46 (2013).
3. Bussolati, B. & Camussi, G. Therapeutic use of human renal progenitor cells for kidney regeneration. *Nat. Rev. Nephrol.* **11**, 695–706 (2015).
4. Little, M. H. & Kairath, P. Regenerative medicine in kidney disease. *Kidney Int.* **90**, 289–299 (2016).
5. European Renal Care Providers Association. European Renal Care Providers Association, Facts & Figures. Available at: <http://ercpa.eu/index.php/facts-figures/>. (Accessed: 29th December 2018)
6. Coresh, J. Update on the Burden of CKD. *J. Am. Soc. Nephrol.* **28**, 1020–1022 (2017).
7. Himmelfarb, J. & Ikizler, T. A. Hemodialysis. *N. Engl. J. Med.* **363**, 1833–1845 (2010).
8. DesRochers, T. M., Palma, E. & Kaplan, D. L. Tissue-engineered kidney disease models. *Adv. Drug Deliv. Rev.* **69–70**, 67–80 (2014).
9. Marx, U. *et al.* Biology-inspired microphysiological system approaches to solve the prediction dilemma of substance testing. *ALTEX* **33**, 272–321 (2016).
10. Al-Awqati, Q. & Oliver, J. A. Stem cells in the kidney. *Kidney Int.* **61**, 387–395 (2002).
11. Hoy, W. E. Nephron Number, Hypertension, Renal Disease, and Renal Failure. *J. Am. Soc. Nephrol.* **16**, 2557–2564 (2005).
12. Westphal, M. Development of a method for decellularization of porcine and human kidney for stem cell tissue engineering. (2012).
13. Kurtz, A. *et al.* CellFinder: Human Body Browser.
14. de Souza, D. B., Gregório, B. M., Benchimol, M. & Nascimento, F. A. de M. in *Modern Electron Microscopy in Physical and Life Sciences* **2**, 64 (InTech, 2016).
15. Dane, M. J. C. *et al.* A microscopic view on the renal endothelial glycocalyx. *Am. J. Physiol. Physiol.* **308**, F956–F966 (2015).
16. Pavenstadt, H., Kriz, W. & Kretzler, M. Cell Biology of the Glomerular Podocyte. *Physiol. Rev.* **83**, 253–307 (2003).
17. Saleem, M. A. One hundred ways to kill a podocyte. *Nephrol. Dial. Transplant.* **30**, 1266–1271 (2015).
18. Kriz, KW, Kaissling, B. in *Seldin and Giebisch's The Kidney* 595–691 (2013).
19. Doucet, A. Function and control of Na-K-ATPase in single nephron segments of the mammalian kidney. *Kidney Int.* **34**, 749–760 (1988).
20. Maunsbach, A. B. *et al.* Aquaporin-1 water channel expression in human kidney. *J. Am. Soc. Nephrol.* **8**, 1–14 (1997).
21. Tune, B. & Burg, M. Glucose transport by proximal renal tubules. *Am. J. Physiol. Content* **221**, 580–585 (1971).
22. Morgan, T. & Berliner, R. Permeability of the loop of Henle, vasa recta, and collecting duct to water, urea, and sodium. *Am. J. Physiol. Content* **215**, 108–115 (1968).
23. Reilly, R. F. & Ellison, D. H. Mammalian Distal Tubule: Physiology,

- Pathophysiology, and Molecular Anatomy. *Physiol. Rev.* **80**, 277–313 (2000).
24. Lawrence, E. A., Doherty, D. & Dhanda, R. Function of the nephron and the formation of urine. *Anaesth. Intensive Care Med.* **19**, 249–253 (2018).
 25. Zeisberg, M. & Kalluri, R. Physiology of the renal interstitium. *Clin. J. Am. Soc. Nephrol.* **10**, 1831–1840 (2015).
 26. Hynes, R. O. & Naba, A. Overview of the Matrisome--An Inventory of Extracellular Matrix Constituents and Functions. *Cold Spring Harb. Perspect. Biol.* **4**, a004903–a004903 (2012).
 27. Hussey, G. S., Dziki, J. L. & Badylak, S. F. Extracellular matrix-based materials for regenerative medicine. *Nat. Rev. Mater.* **3**, 159–173 (2018).
 28. Hynes, R. O. The Extracellular Matrix: Not Just Pretty Fibrils. *Science (80-.).* **326**, 1216–1219 (2009).
 29. Schenk, S. *et al.* Binding to EGF receptor of a laminin-5 EGF-like fragment liberated during MMP-dependent mammary gland involution. *J. Cell Biol.* **161**, 197–209 (2003).
 30. Sebinger, D. D. R., Ofenbauer, A., Gruber, P., Malik, S. & Werner, C. ECM modulated early kidney development in embryonic organ culture. *Biomaterials* **34**, 6670–6682 (2013).
 31. Miner, J. H. Renal basement membrane components. *Kidney Int.* **56**, 2016–24 (1999).
 32. Smith, L. R., Cho, S. & Discher, D. E. Stem Cell Differentiation is Regulated by Extracellular Matrix Mechanics. *Physiology* **33**, 16–25 (2018).
 33. Bateman, J. F., Boot-Handford, R. P. & Lamandé, S. R. Genetic diseases of connective tissues: Cellular and extracellular effects of ECM mutations. *Nat. Rev. Genet.* **10**, 173–183 (2009).
 34. Smyth, N. *et al.* Absence of Basement Membranes after Targeting the LAMC1 Gene Results in Embryonic Lethality Due to Failure of Endoderm Differentiation. *J. Cell Biol.* **144**, 151–160 (1999).
 35. Bonnans, C., Chou, J. & Werb, Z. Remodelling the extracellular matrix in development and disease. *Nat. Rev. Mol. Cell Biol.* **15**, 786–801 (2014).
 36. LeBleu, V. S. *et al.* Origin and function of myofibroblasts in kidney fibrosis. *Nat. Med.* **19**, 1047–1053 (2013).
 37. Genovese, F., Manresa, A. A., Leeming, D. J., Karsdal, M. A. & Boor, P. The extracellular matrix in the kidney: A source of novel non-invasive biomarkers of kidney fibrosis? *Fibrogenes. Tissue Repair* **7**, 1–14 (2014).
 38. Nelson, C. M. & Bissell, M. J. Of Extracellular Matrix, Scaffolds, and Signaling: Tissue Architecture Regulates Development, Homeostasis, and Cancer. *Annu. Rev. Cell Dev. Biol.* **22**, 287–309 (2006).
 39. Bissell, M. J. & Hines, W. C. Why don't we get more cancer? A proposed role of the microenvironment in restraining cancer progression. *Nat. Med.* **17**, 320–329 (2011).
 40. Hohenester, E. & Yurchenco, P. D. Laminins in basement membrane assembly. *Cell Adh. Migr.* **7**, 56–63 (2013).
 41. Halfter, W. *et al.* New concepts in basement membrane biology. *FEBS J.* **282**, 4466–4479 (2015).
 42. Alberts, B. *et al.* *Molecular biology of the cell. Biochemistry and Molecular Biology Education* (2008). doi:10.1002/bmb.20192
 43. Aumailley, M. *et al.* A simplified laminin nomenclature. *Matrix Biol.* **24**, 326–332 (2005).
 44. Miner, J. H. & Yurchenco, P. D. Laminin Functions in Tissue Morphogenesis. *Annu. Rev. Cell Dev. Biol.* **20**, 255–284 (2004).

45. Miner, J. H. Organogenesis of the kidney glomerulus. *Organogenesis* **7**, 75–82 (2011).
46. Lelongt, B. & Ronco, P. Role of extracellular matrix in kidney development and repair. *Pediatr. Nephrol.* **18**, 731–742 (2003).
47. Abrahamson, D. R., St. John, P. L., Stroganova, L., Zelenchuk, A. & Steenhard, B. M. Laminin and Type IV Collagen Isoform Substitutions Occur in Temporally and Spatially Distinct Patterns in Developing Kidney Glomerular Basement Membranes. *J. Histochem. Cytochem.* **61**, 706–718 (2013).
48. Lennon, R. *et al.* Global Analysis Reveals the Complexity of the Human Glomerular Extracellular Matrix. *J. Am. Soc. Nephrol.* 1–13 (2014). doi:10.1681/ASN.2013030233
49. Miner, J. H. The glomerular basement membrane. *Exp. Cell Res.* **318**, 973–978 (2012).
50. Noakes, P. G. *et al.* The renal glomerulus of mice lacking α 5-laminin/laminin β 2: nephrosis despite molecular compensation by laminin β 1. *Nat. Genet.* **10**, 400–406 (1995).
51. Añazco, C., López-jiménez, A. J., Rafi, M. & Vega-montoto, L. Lysyl Oxidase Like-2 Crosslinks Collagen IV of Glomerular Basement Membrane. *J. Biol. Chem.* 1–24 (2016). doi:10.1074/jbc.M116.738856
52. Kühn, K. Basement Membrane (Type IV) Collagen. *Matrix Biol.* **14**, 439–445 (1995).
53. Pöschl, E. *et al.* Collagen IV is essential for basement membrane stability but dispensable for initiation of its assembly during early development. *Development* **131**, 1619–28 (2004).
54. Hudson, B. G., Tryggvason, K., Sundaramoorthy, M. & Neilson, E. G. Alport's Syndrome, Goodpasture's Syndrome, and Type IV Collagen. *N. Engl. J. Med.* **348**, 2543–2556 (2003).
55. Kalluri, R., Shield, C. F., Todd, P., Hudson, B. G. & Neilson, E. G. Isoform switching of type IV collagen is developmentally arrested in X-linked Alport syndrome leading to increased susceptibility of renal basement membranes to endoproteolysis. *J. Clin. Invest.* **99**, 2470–2478 (1997).
56. Yoshioka, K. *et al.* Distribution of type I collagen in human kidney diseases in comparison with type III collagen. *J. Pathol.* **162**, 141–8 (1990).
57. Exposito, J. Y., Valcourt, U., Cluzel, C. & Lethias, C. The fibrillar collagen family. *Int. J. Mol. Sci.* **11**, 407–426 (2010).
58. Murshed, M. *et al.* The absence of nidogen 1 does not affect murine basement membrane formation. *Mol. Cell. Biol.* **20**, 7007–7012 (2000).
59. Willem, M. *et al.* Specific ablation of the nidogen-binding site in the laminin γ 1 chain interferes with kidney and lung development. *Development* **129**, 2711–2722 (2002).
60. Sarrazin, S., Lamanna, W. C. & Esko, J. D. Heparan Sulfate Proteoglycans. *Cold Spring Harb. Perspect. Biol.* **3**, a004952–a004952 (2011).
61. Berg, J. M., Tymoczko, J. L. & Stryer, L. *Biochemistry*. (Freeman: New York, 2007).
62. Perrimon, N. & Bernfield, M. Specificities of heparan sulphate proteoglycans in developmental processes. *Nature* **404**, 725–728 (2000).
63. Iozzo, R. V. Basement membrane proteoglycans: From cellar to ceiling. *Nat. Rev. Mol. Cell Biol.* **6**, 646–656 (2005).
64. Bezakova, G. & Ruegg, M. A. New insights into the roles of agrin. *Nat. Rev. Mol. Cell Biol.* **4**, 295–309 (2003).
65. Bissell, M. J. & Barcellos-Hoff, M. H. The Influence of Extracellular Matrix on Gene

- Expression: Is Structure the Message? *J. Cell Sci.* **1987**, 327–343 (1987).
66. Vining, K. H. & Mooney, D. J. Mechanical forces direct stem cell behaviour in development and regeneration. *Nat. Rev. Mol. Cell Biol.* **18**, 728–742 (2017).
 67. Discher, D. E., Mooney, D. J. & Zandstra, P. W. Growth Factors, Matrices, and Forces Combine and Control Stem Cells. *Science (80-.)*. **324**, 1673–1677 (2009).
 68. Satir, P., Pedersen, L. B. & Christensen, S. T. The primary cilium at a glance. *J. Cell Sci.* **123**, 499–503 (2010).
 69. Liu, X. *et al.* Polycystin-2 is an essential ion channel subunit in the primary cilium of the renal collecting duct epithelium. *Elife* **7**, (2018).
 70. Wilmer, M. J. *et al.* Kidney-on-a-Chip Technology for Drug-Induced Nephrotoxicity Screening. *Trends Biotechnol.* **34**, 156–170 (2016).
 71. Barczyk, M., Carracedo, S. & Gullberg, D. Integrins. *Cell Tissue Res.* **339**, 269–280 (2010).
 72. Sun, Z., Costell, M. & Fässler, R. Integrin activation by talin, kindlin and mechanical forces. *Nat. Cell Biol.* **21**, 25–31 (2019).
 73. Iskratsch, T., Wolfenson, H. & Sheetz, M. P. Appreciating force and shape — the rise of mechanotransduction in cell biology. *Nat. Rev. Mol. Cell Biol.* **15**, 825–833 (2014).
 74. Pelham, R. J. & Wang, Y. -. Cell locomotion and focal adhesions are regulated by substrate flexibility. *Proc. Natl. Acad. Sci.* **94**, 13661–13665 (1997).
 75. Humphrey, J. D., Dufresne, E. R. & Schwartz, M. A. Mechanotransduction and extracellular matrix homeostasis. *Nat. Rev. Mol. Cell Biol.* **15**, 802–812 (2014).
 76. Harburger, D. S. & Calderwood, D. A. Integrin signalling at a glance. *J. Cell Sci.* **122**, 159–163 (2009).
 77. Jaalouk, D. E. & Lammerding, J. Mechanotransduction gone awry. *Nat. Rev. Mol. Cell Biol.* **10**, 63–73 (2009).
 78. Kirby, T. J. & Lammerding, J. Emerging views of the nucleus as a cellular mechanosensor. *Nat. Cell Biol.* **20**, 373–381 (2018).
 79. Fedorchak, G. R., Kaminski, A. & Lammerding, J. Cellular mechanosensing: Getting to the nucleus of it all. *Prog. Biophys. Mol. Biol.* **115**, 76–92 (2014).
 80. Werner, M. *et al.* Surface Curvature Differentially Regulates Stem Cell Migration and Differentiation via Altered Attachment Morphology and Nuclear Deformation. *Adv. Sci.* **201600347**, 1600347 (2016).
 81. Swift, J. *et al.* Nuclear Lamin-A Scales with Tissue Stiffness and Enhances Matrix-Directed Differentiation. *Science (80-.)*. **341**, 1240104–1240104 (2013).
 82. Rho, J. Y., Ashman, R. B. & Turner, C. H. Young’s modulus of trabecular and cortical bone material: ultrasonic and microtensile measurements. *J. Biomech.* **26**, 111–9 (1993).
 83. Ding, Y. *et al.* Biophysical properties of normal and diseased renal glomeruli. *Am. J. Physiol. Physiol.* **300**, C397–C405 (2010).
 84. Gilbert, T. W. *Developmental Biology*. (Palgrave Macmillan, 2003).
 85. Taguchi, A. *et al.* Redefining the In Vivo Origin of Metanephric Nephron Progenitors Enables Generation of Complex Kidney Structures from Pluripotent Stem Cells. *Cell Stem Cell* (2013). doi:10.1016/j.stem.2013.11.010
 86. Short, K. M. & Smyth, I. M. The contribution of branching morphogenesis to kidney development and disease. *Nat. Rev. Nephrol.* **12**, 754–767 (2016).
 87. Little, M. H., Combes, A. N. & Takasato, M. Understanding kidney morphogenesis to guide renal tissue regeneration. *Nat. Rev. Nephrol.* **12**, 624–35 (2016).
 88. Little, M. H. Improving our resolution of kidney morphogenesis across time and space. *Curr. Opin. Genet. Dev.* **32**, 135–143 (2015).

89. Takasato, M. & Little, M. H. The origin of the mammalian kidney: implications for recreating the kidney in vitro. *Development* **142**, 1937–1947 (2015).
90. Griffith, L. G. & Naughton, G. Tissue engineering--current challenges and expanding opportunities. *Science* **295**, 1009–14 (2002).
91. Khademhosseini, A. & Langer, R. A decade of progress in tissue engineering. *Nat. Protoc.* **11**, 1775–1781 (2016).
92. Atala, A., Bauer, S. B., Soker, S., Yoo, J. J. & Retik, A. B. Tissue-engineered autologous bladders for patients needing cystoplasty. *Lancet* **367**, 1241–1246 (2006).
93. Badylak, S. F., Taylor, D. & Uygun, K. Whole-Organ Tissue Engineering: Decellularization and Recellularization of Three-Dimensional Matrix Scaffolds. *Annu. Rev. Biomed. Eng.* **13**, 27–53 (2011).
94. Cummings, B. S., Lasker, J. M. & Lash, L. H. Expression of glutathione-dependent enzymes and cytochrome P450s in freshly isolated and primary cultures of proximal tubular cells from human kidney. *J. Pharmacol. Exp. Ther.* **293**, 677–85 (2000).
95. Freedman, B. S. Modeling kidney disease with iPS cells. *Biomark. Insights* **2015**, 153–169 (2015).
96. Takahashi, K. & Yamanaka, S. Induction of Pluripotent Stem Cells from Mouse Embryonic and Adult Fibroblast Cultures by Defined Factors. *Cell* **126**, 663–676 (2006).
97. Takahashi, K. *et al.* Induction of pluripotent stem cells from adult human fibroblasts by defined factors. *Cell* **131**, 861–872 (2007).
98. Thomson, J. A. *et al.* Embryonic stem cell lines derived from human blastocysts. *Science (80-.)*. **282**, 1145–1147 (1998).
99. Dai, Y., Chen, W., Huang, J., Yu, X. & Lin, X. Generation of induced pluripotent stem cells from renal tubular cells of a patient with Alport syndrome. *Int. J. Nephrol. Renovasc. Dis.* 101 (2015). doi:10.2147/IJNRD.S85733
100. Freedman, B. S. *et al.* Modelling kidney disease with CRISPR-mutant kidney organoids derived from human pluripotent epiblast spheroids. *Nat. Commun.* **6**, 8715 (2015).
101. Tabar, V. & Studer, L. Pluripotent stem cells in regenerative medicine: challenges and recent progress. *Nat. Rev. Genet.* **15**, 82–92 (2014).
102. Dingal, P. C. D. P. & Discher, D. E. Combining insoluble and soluble factors to steer stem cell fate. *Nat. Publ. Gr.* **13**, 532–537 (2014).
103. Wang, B. *et al.* Functional Maturation of Induced Pluripotent Stem Cell Hepatocytes in Extracellular Matrix-A Comparative Analysis of Bioartificial Liver Microenvironments. *Stem Cells Transl. Med.* **5**, 1257–1267 (2016).
104. Yang, X., Pabon, L. & Murry, C. E. Engineering adolescence: maturation of human pluripotent stem cell-derived cardiomyocytes. *Circ. Res.* **114**, 511–23 (2014).
105. Zhang, Z.-N. *et al.* Layered hydrogels accelerate iPSC-derived neuronal maturation and reveal migration defects caused by MeCP2 dysfunction. *Proc. Natl. Acad. Sci.* **113**, 3185–3190 (2016).
106. Gilpin, S. E. *et al.* Enhanced Lung Epithelial Specification of Human Induced Pluripotent Stem Cells on Decellularized Lung Matrix. *Ann. Thorac. Surg.* **98**, 1721–1729 (2014).
107. Lancaster, M. A. *et al.* Cerebral organoids model human brain development and microcephaly. *Nature* **501**, 373–379 (2013).
108. Wu, H. *et al.* Comparative Analysis and Refinement of Human PSC-Derived Kidney Organoid Differentiation with Single-Cell Transcriptomics. *Cell Stem Cell* 1–13 (2018). doi:10.1016/j.stem.2018.10.010

109. Patsch, C. *et al.* Generation of vascular endothelial and smooth muscle cells from human pluripotent stem cells. *Nat. Cell Biol.* **17**, 994–1003 (2015).
110. Bhatia, S. N. & Ingber, D. E. Microfluidic organs-on-chips. *Nat. Biotechnol.* **32**, 760–772 (2014).
111. Lin, N. Y. C. *et al.* Renal reabsorption in 3D vascularized proximal tubule models. *Proc. Natl. Acad. Sci.* **116**, 5399–5404 (2019).
112. Clevers, H. Modeling Development and Disease with Organoids. *Cell* **165**, 1586–1597 (2016).
113. Lam, A. Q. *et al.* Rapid and Efficient Differentiation of Human Pluripotent Stem Cells into Intermediate Mesoderm That Forms Tubules Expressing Kidney Proximal Tubular Markers. *J. Am. Soc. Nephrol.* **25**, 1211–1225 (2014).
114. Takasato, M. *et al.* Directing human embryonic stem cell differentiation towards a renal lineage generates a self-organizing kidney. *Nat. Cell Biol.* **advance on**, (2013).
115. Morizane, R. *et al.* Nephron organoids derived from human pluripotent stem cells model kidney development and injury. *Nat. Biotechnol.* 1–10 (2015). doi:10.1038/nbt.3392
116. Xia, Y. *et al.* Directed differentiation of human pluripotent cells to ureteric bud kidney progenitor-like cells. *Nat. Cell Biol.* **15**, 1–6 (2013).
117. Hariharan, K. *et al.* Parallel generation of easily selectable multiple nephronal cell types from human pluripotent stem cells. *Cell. Mol. Life Sci.* **76**, 179–192 (2018).
118. Homan, K. A. *et al.* Bioprinting of 3D Convulated Renal Proximal Tubules on Perfusable Chips. *Sci. Rep.* **6**, 34845 (2016).
119. Özbek, S., Balasubramanian, P. G., Chiquet-Ehrismann, R., Tucker, R. P. & Adams, J. C. The Evolution of Extracellular Matrix. *Mol. Biol. Cell* **21**, 4300–4305 (2010).
120. Mecham, R. P. *The Extracellular Matrix: an Overview.* (Springer Berlin Heidelberg, 2011). doi:10.1007/978-3-642-16555-9
121. Haschek, W. M., Rousseaux, C. G., Wallig, M. A., Bolon, B. & Ochoa, R. *Haschek and Rousseaux's Handbook of Toxicologic Pathology.* (Academic Press, 2013).
122. Giraud, S. *et al.* Contribution of Large Pig for Renal Ischemia-Reperfusion and Transplantation Studies: The Preclinical Model. *J. Biomed. Biotechnol.* **2011**, 1–14 (2011).
123. Song, J. J. *et al.* Regeneration and experimental orthotopic transplantation of a bioengineered kidney. *Nat. Med.* **19**, 646–51 (2013).
124. Hughes, C. S., Postovit, L. M. & Lajoie, G. A. Matrigel: a complex protein mixture required for optimal growth of cell culture. *Proteomics* **10**, 1886–1890 (2010).
125. Ott, H. C. *et al.* Perfusion-decellularized matrix: using nature's platform to engineer a bioartificial heart. *Nat. Med.* **14**, 213–221 (2008).
126. Crapo, P. M., Gilbert, T. W. & Badylak, S. F. An overview of tissue and whole organ decellularization processes. *Biomaterials* **32**, 3233–43 (2011).
127. Gilbert, T. W., Sellaro, T. L. & Badylak, S. F. Decellularization of tissues and organs. *Biomaterials* **27**, 3675–3683 (2006).
128. Griffin, W. Classification of Surface Active Agents. *J. Cosmet. Sci.* **1**, 311–326 (1949).
129. Helenius, A. & Simons, K. Solubilization of membranes by detergents. *Biochim. Biophys. Acta, Biomembr.* **415**, 29–79 (1975).
130. Galili, U. The α -gal epitope (Gal α 1-3Gal β 1-4GlcNAc-R) in xenotransplantation. *Biochimie* **83**, 557–563 (2001).
131. Gilbert, T. W. Strategies for tissue and organ decellularization. *J. Cell. Biochem.* **113**, 2217–2222 (2012).

132. Badylak, S. F. Decellularized Allogeneic and Xenogeneic Tissue as a Bioscaffold for Regenerative Medicine: Factors that Influence the Host Response. *Ann. Biomed. Eng.* (2014). doi:10.1007/s10439-013-0963-7
133. Keane, T. J., Londono, R., Turner, N. J. & Badylak, S. F. Consequences of ineffective decellularization of biologic scaffolds on the host response. *Biomaterials* **33**, 1771–1781 (2012).
134. Vracko, R. Basal lamina scaffold-anatomy and significance for maintenance of orderly tissue structure. *Am. J. Pathol.* **77**, 314–46 (1974).
135. Del Monte, U. Does the cell number 10⁹ still really fit one gram of tumor tissue? *Cell Cycle* **8**, 505–506 (2009).
136. Scarritt, M. E., Pashos, N. C. & Bunnell, B. a. A review of cellularization strategies for tissue engineering of whole organs. *Front. Bioeng. Biotechnol.* **3**, 43 (2015).
137. Bijonowski, B. M., Miller, W. M. & Wertheim, J. A. Bioreactor design for perfusion-based , highly vascularized organ regeneration. *Curr. Opin. Chem. Eng.* **2**, 31–39 (2013).
138. Rossbach, B. *et al.* Generation of a human induced pluripotent stem cell line from urinary cells of a healthy donor using integration free Sendai virus technology. *Stem Cell Res.* **21**, 167–170 (2017).
139. Hossini, A. M. *et al.* PI3K/AKT Signaling Pathway Is Essential for Survival of Induced Pluripotent Stem Cells. *PLoS One* **11**, e0154770 (2016).
140. Yu, J. *et al.* Induced Pluripotent Stem Cell Lines Derived from Human Somatic Cells. *Science (80-.)*. **318**, 1917–1920 (2007).
141. Ren, X. *et al.* Engineering pulmonary vasculature in decellularized rat and human lungs. *Nat. Biotechnol.* **c**, 1–13 (2015).
142. Orlova, V. V *et al.* Generation, expansion and functional analysis of endothelial cells and pericytes derived from human pluripotent stem cells. *Nat. Protoc.* **9**, 1514–31 (2014).
143. Di Lorenzo, F., Hellwig, J., Von Klitzing, R. & Seiffert, S. Macroscopic and Microscopic Elasticity of Heterogeneous Polymer Gels. *ACS Macro Lett.* **4**, 698–703 (2015).
144. Caralt, M. *et al.* Optimization and Critical Evaluation of Decellularization Strategies to Develop Renal Extracellular Matrix Scaffolds as Biological Templates for Organ Engineering and Transplantation. *Am. J. Transplant* 64–75 (2015). doi:10.1111/ajt.12999
145. Uzarski, J. S., Divito, M. D., Wertheim, J. A. & Miller, W. M. Essential design considerations for the resazurin reduction assay to noninvasively quantify cell expansion within perfused extracellular matrix scaffolds. *Biomaterials* **129**, 163–175 (2017).
146. Skogestad, S. Probably the best simple PID tuning rules in the world. *J. Process Control* **xx**, 1–27 (2001).
147. Lunze, J. *Regelungstechnik 1. Regelungstechnik 1* (Springer Berlin Heidelberg, 2008). doi:10.1007/978-3-540-68909-6
148. He, M., Callanan, A., Lagaras, K., Steele, J. A. M. & Stevens, M. M. Optimization of SDS exposure on preservation of ECM characteristics in whole organ decellularization of rat kidneys. *J. Biomed. Mater. Res. Part B Appl. Biomater.* 1–9 (2016). doi:10.1002/jbm.b.33668
149. Poornejad, N. *et al.* The impact of decellularization agents on renal tissue extracellular matrix. *J. Biomater. Appl.* **31**, 521–533 (2016).
150. Takebe, T. *et al.* Vascularized and complex organ buds from diverse tissues via

- mesenchymal cell-driven condensation. *Cell Stem Cell* **16**, 556–565 (2015).
151. Taft, D. R. The Isolated Perfused Rat Kidney Model: A Useful Tool for Drug Discovery and Development. 97–111 (2004).
 152. Bekersky, I. *Use of the isolated perfused kidney as a tool in drug disposition studies. Drug Metabolism Reviews* **14**, (1983).
 153. Wszola, M. *et al.* One-year results of a prospective, randomized trial comparing two machine perfusion devices used for kidney preservation. *Transpl. Int.* **26**, 1088–1096 (2013).
 154. De Deken, J., Kocabayoglu, P. & Moers, C. Hypothermic machine perfusion in kidney transplantation. *Curr. Opin. Organ Transplant.* **21**, 294–300 (2016).
 155. Moers, C., Pirenne, J., Paul, A. & Ploeg, R. J. Machine Perfusion or Cold Storage in Deceased-Donor Kidney Transplantation. *N. Engl. J. Med.* **366**, 770–771 (2012).
 156. Sullivan, D. C. *et al.* Decellularization methods of porcine kidneys for whole organ engineering using a high-throughput system. *Biomaterials* **33**, 7756–7764 (2012).
 157. Bonandrini, B. *et al.* Recellularization of Well-Preserved Acellular Kidney Scaffold Using Embryonic Stem Cells. *Tissue Eng. Part A* **20**, 1486–1498 (2014).
 158. Peloso, A. *et al.* Creation and implantation of acellular rat renal ECM-based scaffolds. *Organogenesis* **11**, 58–74 (2015).
 159. Du, C., Narayanan, K. & Leong, M. Functional Kidney Bioengineering with Pluripotent Stem-Cell-Derived Renal Progenitor Cells and Decellularized Kidney Scaffolds. *Advanced* (2016). doi:10.1002/adhm.201600120
 160. Uzarski, J. S. *et al.* Dual-Purpose Bioreactors to Monitor Noninvasive Physical and Biochemical Markers of Kidney and Liver Scaffold Recellularization. *Tissue Eng. Part C Methods* **21**, 1032–1043 (2015).
 161. Charest, J. M. *et al.* Design and validation of a clinical-scale bioreactor for long-term isolated lung culture. *Biomaterials* **52**, 79–87 (2015).
 162. Ross, E. a *et al.* Embryonic stem cells proliferate and differentiate when seeded into kidney scaffolds. *J. Am. Soc. Nephrol.* **20**, 2338–47 (2009).
 163. Hülsmann, J. *et al.* A novel customizable modular bioreactor system for whole-heart cultivation under controlled 3D biomechanical stimulation. *J. Artif. Organs* **16**, 294–304 (2013).
 164. Schuerlein, S. *et al.* A versatile modular bioreactor platform for Tissue Engineering. *Biotechnol. J.* **12**, (2017).
 165. Jang, K.-J. *et al.* Human kidney proximal tubule-on-a-chip for drug transport and nephrotoxicity assessment. *Integr. Biol.* **5**, 1119 (2013).
 166. Essig, M., Terzi, F., Burtin, M. & Friedlander, G. Mechanical strains induced by tubular flow affect the phenotype of proximal tubular cells. *Am. J. Physiol. Physiol.* **281**, F751–F762 (2001).
 167. Friedrich, C., Endlich, N., Kriz, W. & Endlich, K. Podocytes are sensitive to fluid shear stress in vitro. *Am. J. Physiol. Physiol.* **291**, F856–F865 (2006).
 168. Czogalla, J., Schweda, F. & Loffing, J. The Mouse Isolated Perfused Kidney Technique. *J. Vis. Exp.* (2016). doi:10.3791/54712
 169. National Instruments. LabVIEW Core 2 Participant Guide. (2014).
 170. Yoldas, A. & Dayan, M. O. Morphological characteristics of renal artery and kidney in rats. *Sci. World J.* **2014**, 1–8 (2014).
 171. Najjari, M. R. & Plesniak, M. W. PID controller design to generate pulsatile flow rate for in vitro experimental studies of physiological flows. *Biomed. Eng. Lett.* (2017). doi:10.1007/s13534-017-0049-9
 172. Curthoys, N. P. & Moe, O. W. Proximal tubule function and response to acidosis.

- Clin. J. Am. Soc. Nephrol.* **9**, 1627–1638 (2014).
173. Price, A. P., England, K. A., Matson, A. M., Blazar, B. R. & Panoskaltsis-Mortari, A. Development of a Decellularized Lung Bioreactor System for Bioengineering the Lung: The Matrix Reloaded. *Tissue Eng. Part A* **16**, 2581–2591 (2010).
 174. Guyette, J. P. *et al.* Bioengineering Human Myocardium on Native Extracellular Matrix. *Circ. Res.* **118**, 56–72 (2016).
 175. Nakayama, K. H., Batchelder, C. A., Lee, C. I. & Tarantal, A. F. Decellularized rhesus monkey kidney as a three-dimensional scaffold for renal tissue engineering. *Tissue Eng. Part A* **16**, 2207–16 (2010).
 176. Fischer, I. *et al.* Comparative characterization of decellularized renal scaffolds for tissue engineering. *Biomed. Mater.* **12**, 045005 (2017).
 177. Wang, Y. *et al.* Method for perfusion decellularization of porcine whole liver and kidney for use as a scaffold for clinical-scale bioengineering engrafts. *Xenotransplantation* (2014). doi:10.1111/xen.12141
 178. Choi, S. H. *et al.* Development of a porcine renal extracellular matrix scaffold as a platform for kidney regeneration. *J. Biomed. Mater. Res. Part A* **103**, 1391–1403 (2015).
 179. Grauss, R. W. *et al.* Histological evaluation of decellularised porcine aortic valves: matrix changes due to different decellularisation methods. *Eur. J. cardio-thoracic Surg.* **27**, 566–71 (2005).
 180. Carey, M. C. Micelle Formation by Bile Salts. *Arch. Intern. Med.* **130**, 506 (1972).
 181. Barrett, A. S. *et al.* Hydroxylamine Chemical Digestion for Insoluble Extracellular Matrix Characterization. *J. Proteome Res.* **16**, 4177–4184 (2017).
 182. Higami, T. *et al.* Effect of treatment temperature on collagen structures of the decellularized carotid artery using high hydrostatic pressure. *J. Artif. Organs* **14**, 223–231 (2011).
 183. Einstein, A. *Investigations on the Theory of the Brownian Movement.* (Courier Corporation, 1956).
 184. Nelson, D. L. & Cox, M. *Lehninger Principles of Biochemistry: International Edition.* (WH Freeman, 2017).
 185. Shimoda, M. in 35–66 (2019). doi:10.1016/bs.acc.2018.10.006
 186. Shapiro, S. D. Matrix metalloproteinase degradation of extracellular matrix: Biological consequences. *Curr. Opin. Cell Biol.* **10**, 602–608 (1998).
 187. Sato, H. *et al.* A matrix metalloproteinase expressed on the surface of invasive tumour cells. *Nature* **370**, 61–65 (1994).
 188. Malesmud, C. J. Matrix metalloproteinases (MMPs) in health and disease: an overview. *Front. Biosci.* **11**, 1696–701 (2006).
 189. Cebotari, S. *et al.* Detergent decellularization of heart valves for tissue engineering: toxicological effects of residual detergents on human endothelial cells. *Artif. Organs* **34**, 206–10 (2010).
 190. Morris, A. H., Chang, J. & Kyriakides, T. R. Inadequate Processing of Decellularized Dermal Matrix Reduces Cell Viability In Vitro and Increases Apoptosis and Acute Inflammation In Vivo. *Biores. Open Access* **5**, 177–187 (2016).
 191. Duplâtre, G., Ferreira Marques, M. F. & da Graça Miguel, M. Size of Sodium Dodecyl Sulfate Micelles in Aqueous Solutions as Studied by Positron Annihilation Lifetime Spectroscopy. *J. Phys. Chem.* **100**, 16608–16612 (1996).
 192. Borgström, B. The dimensions of the bile salt micelle. Measurements by gel filtration. *Biochim. Biophys. Acta - Lipids Lipid Metab.* **106**, 171–183 (1965).
 193. Walker, G. M., Zeringue, H. C. & Beebe, D. J. Microenvironment design

- considerations for cellular scale studies. *Lab Chip* **4**, 91–97 (2004).
194. Thureau, K. Renal hemodynamics. *Am. J. Med.* **36**, 698–719 (1964).
195. Tudorache, I. *et al.* Tissue engineering of heart valves: biomechanical and morphological properties of decellularized heart valves. *J. Heart Valve Dis.* **16**, 567–73; discussion 574 (2007).
196. Zhou, J. *et al.* Impact of heart valve decellularization on 3-D ultrastructure, immunogenicity and thrombogenicity. *Biomaterials* **31**, 2549–54 (2010).
197. Hiller, T. *et al.* Study of Viral Vectors in a Three-dimensional Liver Model Repopulated with the Human Hepatocellular Carcinoma Cell Line HepG2. *J. Vis. Exp.* 1–6 (2016). doi:10.3791/54633
198. Wang, Y. *et al.* Lineage restriction of human hepatic stem cells to mature fates is made efficient by tissue-specific biomatrix scaffolds. *Hepatology* **53**, 293–305 (2011).
199. Yu, Y. L. *et al.* Decellularized kidney scaffold-mediated renal regeneration. *Biomaterials* **35**, 6822–6828 (2014).
200. Aird, W. C. Endothelial Cell Heterogeneity. *Cold Spring Harb. Perspect. Med.* **2**, a006429–a006429 (2012).
201. Frimat, M. *et al.* Endothelium structure and function in kidney health and disease. *Nat. Rev. Nephrol.* **15**, 87–108 (2019).
202. Orlando, G. *et al.* Production and implantation of renal extracellular matrix scaffolds from porcine kidneys as a platform for renal bioengineering investigations. *Ann. Surg.* **256**, 363–70 (2012).
203. Baptista, P. M. *et al.* The use of whole organ decellularization for the generation of a vascularized liver organoid. *Hepatology* **53**, 604–17 (2011).
204. Jaffe, E. A., Nachman, R. L., Becker, C. G. & Minick, C. R. Culture of human endothelial cells derived from umbilical veins. Identification by morphologic and immunologic criteria. *J. Clin. Invest.* **52**, 2745–2756 (1973).
205. Jiménez, N., Krouwer, V. J. D. & Post, J. A. A new, rapid and reproducible method to obtain high quality endothelium in vitro. *Cytotechnology* **65**, 1–14 (2013).
206. Wolburg, K. *et al.* Vascular Endothelial Growth Factor Induces Endothelial Fenestrations In Vitro. *J. Cell Biol.* **140**, 947–959 (2002).
207. Wu, Y.-T. *et al.* Defining minimum essential factors to derive highly pure human endothelial cells from iPS/ES cells in an animal substance-free system. *Sci. Rep.* **5**, 9718 (2015).
208. Daigh, C., Fuhrken, P. & Salvagiotto, G. Methods and compositions for the differentiation of stem cells. *US Patent 8,557,580* **2**, 694–700 (2013).
209. Gulino-Debrac, D. Mechanotransduction at the basis of endothelial barrier function. *Tissue Barriers* **1**, e24180 (2013).
210. James, D. *et al.* Expansion and maintenance of human embryonic stem cell-derived endothelial cells by TGF β inhibition is Id1 dependent. *Nat. Biotechnol.* **28**, 161–166 (2010).
211. Hariharan, K. In vitro nephrogenesis from human pluripotent stem cells. (Humboldt-Universität zu Berlin, Lebenswissenschaftliche Fakultät, 2016). doi:http://dx.doi.org/10.18452/19194
212. Mader, S. S. *Understanding Human Anatomy & Physiology.* **79**, (2004).
213. Remuzzi, A. *et al.* Experimental Evaluation of Kidney Regeneration by Organ Scaffold Recellularization. *Sci. Rep.* **7**, 43502 (2017).
214. White, L. J. *et al.* The impact of detergents on the tissue decellularization process: a ToF-SIMS study. *Acta Biomater.* (2016). doi:10.1016/j.actbio.2016.12.033

215. Romero, C. A. *et al.* Non-invasive Measurement of Renal Blood Flow by Magnetic Resonance Imaging (MRI) in Rats. *Am. J. Physiol. - Ren. Physiol.* **ajprenal.00332.2017** (2017). doi:10.1152/ajprenal.00332.2017
216. Hsu, C. H., Kurtz, T. W. & Waldinger, T. P. Cardiac output and renal blood flow in glycerol induced acute renal failure in the rat. *Circ. Res.* **40**, 178–182 (1977).
217. Batchelder, C. a, Martinez, M. L. & Tarantal, A. F. Natural Scaffolds for Renal Differentiation of Human Embryonic Stem Cells for Kidney Tissue Engineering. *PLoS One* **10**, e0143849 (2015).
218. Jank, B. J. *et al.* Engineered composite tissue as a bioartificial limb graft. *Biomaterials* **61**, 246–256 (2015).
219. Petrosyan, A. *et al.* Decellularized Renal Matrix and Regenerative Medicine of the Kidney: A Different Point of View. *Tissue Eng. Part B Rev.* **22**, 183–192 (2016).
220. Figliuzzi, M., Bonandrini, B. & Remuzzi, A. Decellularized kidney matrix as functional material for whole organ tissue engineering. *J. Appl. Biomater. Funct. Mater.* **15**, 0–0 (2017).
221. Engler, A. J., Sen, S., Sweeney, H. L. & Discher, D. E. Matrix Elasticity Directs Stem Cell Lineage Specification. *Cell* **126**, 677–689 (2006).
222. Narayanan, K. *et al.* Human embryonic stem cells differentiate into functional renal proximal tubular-like cells. *Kidney Int.* **83**, 593–603 (2013).
223. Yamada, M. & Sekiguchi, K. *Molecular Basis of Laminin-Integrin Interactions. Current Topics in Membranes* **76**, (Elsevier Ltd, 2015).
224. Suh, J. H., Jarad, G., VanDeVoorde, R. G. & Miner, J. H. Forced expression of laminin 1 in podocytes prevents nephrotic syndrome in mice lacking laminin 2, a model for Pierson syndrome. *Proc. Natl. Acad. Sci.* **108**, 15348–15353 (2011).
225. Ullah, I. *et al.* VEGF – Supplemented extracellular matrix is sufficient to induce endothelial differentiation of human iPSC. *Biomaterials* **216**, (2019).
226. Murphy, S. V. & Atala, A. 3D bioprinting of tissues and organs. *Nat. Biotechnol.* **32**, 773–785 (2014).
227. Wu, J. *et al.* Interspecies Chimerism with Mammalian Pluripotent Stem Cells. *Cell* **168**, 473–486.e15 (2017).
228. Freedman, B. S. Hopes and Difficulties for Blastocyst Complementation. *Nephron* **138**, 42–47 (2018).
229. Morizane, R. & Bonventre, J. V. Kidney Organoids: A Translational Journey. *Trends Mol. Med.* **23**, 246–263 (2017).
230. Taguchi, A. & Nishinakamura, R. Higher-Order Kidney Organogenesis from Pluripotent Stem Cells. *Cell Stem Cell* 1–17 (2017). doi:10.1016/j.stem.2017.10.011

Kidney icons in Figure 1, 8-11, 13, 25, 32, 36, 37, 39, 42 ,45-50 were modified from Cellfinder, licensed under CC BY 3.0 (<https://creativecommons.org/licenses/by/3.0/>).

Cell icons in Figure 6, 9, 25, 32, 39 were modified from Servier Medical Art, licensed under CC BY 3.0 (<https://creativecommons.org/licenses/by/3.0/>).

8 Appendix

8.1 Supplemental information

Analysis Sequence "Count attached GFP+ cells"	
Input Image	Stack Processing : Individual Planes Flatfield Correction : None
Find Cells	Channel : Alexa 488 ROI : None Method : Mean Kernel Size : 30 µm Splitting Coefficient : 0.1 Common Threshold : 0.3 Output Population : Cells
Calculate Intensity Properties	Channel : Alexa 488 Population : Cells Region : Cell Method : Standard Mean Output Properties : Intensity Call Alexa 488
Calculate Morphology Properties	Method : STAR Channel : Alexa 488 Region : Cell Threshold Compactness Axial Radial Profile Profile Width : 4 px Slope Minima Curvature : 1.0 Texture SER Scale : 1 px Normalization by : Kernel Output Properties : Cell Morphology
Calculate Morphology Properties (2)	Method : Standard Area Output Properties : Cell Area
Select Population (2)	Method : Filter by Property Call Area Area [µm²] : < 2500 Intensity Call Alexa 488 Mean : > 500 Boolean Operations : F1 and F2 Output Population : Cells Selected
Select Population	Method : Linear Classifier Number of Classes : 3 Class 0 : Non-Adherent Class 1 : Adherent Class 2 : Floating Call Morphology Symmetry 02 Call Morphology Symmetry 03 Call Morphology Symmetry 04 Call Morphology Symmetry 05 Call Morphology Symmetry 12 Call Morphology Symmetry 13 Call Morphology Symmetry 14 Call Morphology Symmetry 15 Call Morphology Threshold Compactness 30% Call Morphology Threshold Compactness 40% Call Morphology Threshold Compactness 50% Call Morphology Threshold Compactness 60% Call Morphology Axial Length Ratio Call Morphology Radial Mean Call Morphology Radial Relative Deviation Call Morphology Profile 172 Call Morphology Profile 272 Call Area Area [µm²] Output Population A : Adherent Output Population B : Floating Output Population C : OutOfFocus
Define Results	Method : List of Outputs Population : Cells Selected Number of Objects Population : Cells Number of Objects Population : Adherent Number of Objects Population : Floating Number of Objects Population : OutOfFocus Number of Objects Object Results : None

Academia version: 4.1.3.12479; Timestamp: 2018-06-21 14:54:39 +0000.

Figure S1: Analysis sequence “Count attached GFP+ cells” in Harmony High-content imaging software

Analysis Sequence "Count DAPI-nuclei on kidney sections"	
Input Image	Stack Processing : Individual Planes Flatfield Correction : None
Find Nuclei	Channel : DAPI ROI : None Method : M13.um Smoothing Coefficient : 0.2 Common Threshold : 0.4 Output Population : Nuclei
Calculate Morphology Properties	Population : Nuclei Region : Nucleus Method : Standard Area Roundness Output Properties : Nucleus
Calculate Intensity Properties	Channel : DAPI Population : Nuclei Region : Nucleus Method : Standard Mean Output Properties : Intensity Nucleus DAPI
Select Population	Population : Nuclei Method : Filter by Property Nucleus Area [um ²] : < 100 Nucleus Roundness : > 0.7 Intensity Nucleus DAPI Mean : > 1000 Boolean Operations : F1 and F2 and F3 Output Population : Nuclei Selected
Find Image Region	Channel : DAPI ROI : None Method : Common Threshold Threshold : 0.043 Area : > 1000 um ² Output Population : Image Region Output Region : Image Region
Calculate Morphology Properties (2)	Population : Image Region Region : Image Region Method : Standard Area Roundness Output Properties : Image Region
Define Results	Method : List of Outputs Population : Nuclei Population : Nuclei Selected Number of Objects Population : Image Region Number of Objects Method : Formula Output Formula : a/b Population Type : Objects Variable A : Nuclei Selected - Number of Objects Variable B : Image Region - Number of Objects Output Name : Nuclei/Image Method : Formula Output Formula : a/b Population Type : Objects Variable A : Nuclei Selected - Number of Objects Variable B : Image Region - Image Region Area [um ²] Mean Output Name : Nuclei/um ² Single Cell Results : None
Acrapella version 4.0.0.113678, Timestamp: 2018-03-28 15:23:57 -0200.	

Figure S2: Analysis sequence “Count DAPI-nuclei on kidney sections” in Harmony High-content imaging software

8.2 Abbreviations

2D	two-dimensional
3D	three-dimensional
ADH	antidiuretic hormone
AQP1	aquaporin 1
ATP1A1	sodium potassium-pump, subunit alpha-1
bFGF	basic fibroblast growth factor
BM	basement membrane
BMP4	bone morphogenetic protein 4
BSA	bovine serum albumin
cDNA	complementary DNA
CKD	chronic kidney disease
ColIV	collagen IV
COM	communication
CTR	control
CV	control variable
DAPI	4',6-diamidino-2-phenylindole
diH ₂ O	distilled water
DNA	deoxyribonucleic acid
dsDNA	double stranded deoxyribonucleic acid
E	error
<i>E</i> modulus	elastic modulus
ECM	extracellular matrix
ECs	endothelial cells
EDTA	ethylenediaminetetraacetic acid
EGF	epidermal growth factor-like
EGM-2	endothelial growth medium 2
EGTA	egtazic acid
ESRD	end stage renal disease
FCS	fetal calf serum
GAG	glycosaminoglycan
GAPDH	glyceraldehyde 3-phosphate dehydrogenase
GBM	glomerular basement membrane
GDNF	glial cell-derived neurotrophic factor
HE	hematoxylin and eosin
hiPSCs	human induced pluripotent stem cells
HLB	hydrophilic-lipophilic balance
HSPG	heparan sulphate proteoglycan

HUVECs	human umbilical vein endothelial cells
IMCs	hiPSC-derived intermediate mesoderm cells
Lam-1, L111	laminin 111
Lam-10, L511	laminin 511
Lam-11, L521	laminin 521
MBVs	matrix bound vesicles
MMPs	matrix metalloproteinases
Na ⁺ /K ⁺ -ATPase	sodium potassium-pump
O/N	overnight
PAA	peracetic acid
PDGF	platelet-derived growth factor
PDMS	polydimethylsiloxane
PODXL	podocalyxin like
POMA	poly[octadecene-alt-(maleic anhydride)]
PV	process variable
qPCR	quantitative polymerase chain reaction
RA	renal artery
REGM	renal epithelial growth medium
RNA	ribonucleic acid
RNA18S5	18S ribosomal 5
ROCKi	Rho-associated protein kinase-inhibitor
RPCs	hiPSC-derived renal progenitor cells
RTECs	renal tubular epithelial cells
RT-PCR	reverse transcription polymerase chain reaction
RV	renal vein
SIX2	SIX homeobox 2
SLC12A2	Na-K-Cl cotransporter 1, solute carrier family 12 member 2
SLC12A3	sodium-chloride symporter, solute carrier family 12 member 3
SP	setpoint
SYNPO	synaptopodin
TGFβ	transforming growth factor β
U	ureter
VEGF	vascular endothelial growth factor
WT1	Wilms tumor protein

8.3 List of figures

Figure 1: Anatomy of the human kidney.....	3
Figure 2: Interactions of cells with their surrounding ECM.....	5
Figure 3: Structure and composition of renal basement membranes.....	7
Figure 4: The effect of extracellular matrix properties on the cell.....	10
Figure 5: Development of the mammalian kidney.	13
Figure 6: Human induced pluripotent stem cells.....	15
Figure 7: Differences between 2D and 3D <i>in vitro</i> tissue models.....	16
Figure 8: Decellularization of whole rat or pig kidneys.....	19
Figure 9: Recellularization	20
Figure 10: Organ preparation for decellularization of whole rat kidneys by perfusion	36
Figure 11: Schematic setup of the decellularization perfusion bioreactor	37
Figure 12: Resazurin.....	43
Figure 13: Schematic setup of the recellularization perfusion bioreactor.	51
Figure 14: Setup of the perfusion bioreactor.	52
Figure 15: User interface of the control software for the perfusion bioreactor.	54
Figure 16: Architecture of the control software for the perfusion bioreactor.	55
Figure 17: Block diagram of the pressure feedback loop.....	57
Figure 18: Step response to pump speed change.....	58
Figure 19: Reference-variable response of the control system.....	60
Figure 20: Disturbance response of the pressure control system.	61
Figure 21: Block diagram of the pH feedback loop.	62
Figure 22: Step response to CO ₂ change.	63
Figure 23: Reference-variable response of the pH control system.....	64
Figure 24: Disturbance response of the pH control system.....	65
Figure 25: The experimental process of the de- and recellularization of porcine kidneys by immersion and agitation.	66
Figure 26: Macroscopic and histological analysis of native and SDC-decellularized porcine kidney cubes at 4 °C, RT and 37 °C.....	68
Figure 27: Macroscopic and histological analysis of SDS-decellularized porcine kidney cubes at 4 °C, RT and 37 °C.....	69

Figure 28: Macroscopic and histological analysis of TX-100-decellularized porcine kidney cubes at 4 °C, RT and 37 °C.....	70
Figure 29: Composition analysis of immersion-decellularized matrices	72
Figure 30: Differentiation scheme of hiPSC-derived intermediate mesoderm cells.	73
Figure 31: Analysis of IMC viability and attachment on immersion-decellularized kidney sections.	74
Figure 32: The experimental process of kidney decellularization by perfusion and biocompatibility testing of the scaffold by reendothelialization.	77
Figure 33: Macroscopic and histological analysis of native and perfusion-decellularized rat kidneys at 4 °C and RT.....	78
Figure 34: Composition analysis of perfusion-decellularized matrices.	80
Figure 35: Characterization of human umbilical vein endothelial cells.....	80
Figure 36: Reendothelialization of perfusion-decellularized kidneys by SDC at RT.	81
Figure 37: Reendothelialization of perfusion-decellularized kidneys by SDS/TX-100 at RT	82
Figure 38: Comparative biocompatibility testing of perfusion-decellularized kidneys.	83
Figure 39: Generation of the kidney model by de- and recellularization of rat kidneys.	86
Figure 40: Differentiation scheme of hiPSC-derived endothelial cells.....	87
Figure 41: Optimization of hiPSC-ECs expansion conditions.....	88
Figure 42: Arterial seeding of hiPSC-ECs.	89
Figure 43: CD31+ endothelial cells lined the blood vessels and the glomerular capillaries in the recellularized kidneys.	90
Figure 44: Differentiation scheme of hiPSC-derived RPCs.....	90
Figure 45: Arterial seeding of RPCs.....	91
Figure 46: High-pressure arterial seeding of RPCs.....	92
Figure 47: Arterial seeding of RPCs into partly trypsin-digested scaffolds.....	93
Figure 48: Ureter seeding of RPCs without vacuum.....	94
Figure 49: Ureter seeding of RPCs with vacuum.....	95
Figure 50: Injection of RPCs into the cortex of perfusion-decellularized kidneys with a syringe.	96
Figure 51: Quantitative analysis and comparison of seeding strategies.....	97
Figure 52: PDMS gel properties.....	98
Figure 53: Renal tubular epithelial cell morphology on ECM-coated PDMS	100

Figure 54: RPC and RTEC gene expression on ECM-coated PDMS	101
--	-----

8.4 List of tables

Table 1: Species differences in renal structure	18
Table 2: Cells.....	23
Table 3: Reagents	23
Table 4: Consumables	25
Table 5: Kits	26
Table 6: Primary and secondary antibodies and nucleic acid dyes	27
Table 7: TaqMan gene expression assays.....	27
Table 8: Instruments	27
Table 9: Software and data bases	29
Table 10: List of the expansion media for hiPSC-derived endothelial cells	33
Table 11: Overview of decellularization by immersion and agitation conditions.....	35
Table 12: SDC protocol conditions for decellularization by perfusion.....	38
Table 13: SDS/TX-100 protocol conditions for decellularization by perfusion	38
Table 14: System settings for controller tuning	44
Table 15: PDMS preparations	44
Table 16: TaqMan RT Reaction Mix	45
Table 17: RT-PCR cycling conditions	45
Table 18: TaqMan qPCR Reaction Mix for a 384-well plate.....	46
Table 19: qPCR cycling conditions	46
Table 20: Dehydrating steps before embedding of tissue in paraffin blocks	46
Table 21: Rehydration of paraffin sections	47
Table 22: HE staining on rehydrated paraffin sections	47
Table 23: Antigen retrieval treatments for immunofluorescence staining	48
Table 24: Overview over the technical background of the perfusion bioreactor	51
Table 25: Tuning methods used for adjusting the pressure and pH controller.....	59
Table 26: Scoring table of immersion-decellularized porcine kidneys	76
Table 27: Scoring table of perfusion-decellularized rat kidneys.....	84
Table 28: Scoring table of perfusion-decellularized rat and porcine kidneys	85

8.5 Acknowledgements

Ich möchte mich ganz herzlich bei allen bedanken, die mich während der Durchführung meiner Doktorarbeit unterstützt haben.

Der größte Dank gilt meinen drei Betreuern am BCRT. Herzlichen Dank an **Dr. Harald Stachelscheid**, der mein Dissertationsprojekt ins Leben gerufen hat und mir immer unterstützend zur Seite stand. Des Weiteren gilt mein Dank **Dr. Andreas Kurtz** für die Möglichkeit, in seiner Arbeitsgruppe forschen zu können, sowie seine fachliche Unterstützung. Frau **Prof. Dr. Petra Reinke** möchte ich ebenfalls herzlich für ihre Betreuung danken, insbesondere für das Einbringen der klinischen Perspektive.

In zahlreichen richtungsweisenden, fachlichen Diskussionen, wöchentlichen Arbeitsgruppenmeetings sowie konstruktiven Mentoring Meetings habe ich durch meine Mentoren viel Unterstützung erfahren. Sie haben somit entscheidend zum Fortschritt und Erfolg meiner Arbeit beigetragen und mich in den letzten Jahren zu der Wissenschaftlerin ausgebildet, die ich heute bin. Herzlichen Dank.

Des Weiteren möchte ich mich bei **Prof. Dr. Roland Lauster** für seine Betreuung von universitärer Seite bedanken. Auf den alljährlichen Tagen der Biotechnologie hat er immer wieder frische Ideen in das Projekt eingebracht.

Großer Dank gilt **Michael Westphal**, der mit seiner Arbeit den Grundstein für mein Dissertationsprojekt gelegt hat und mich in viele der verwendeten Methoden eingearbeitet hat. Ebenso möchte ich mich bei **Dr. Ansgar Petersen** bedanken, dessen Expertise essenziell war für die PDMS-Experimente. **Su-Jun Oh** sowie **Cornelia Heckmann** danke ich für die Einführung in die Operationstechniken. **Johannes Hellwig** und **Dr. Aarón Xerach Herrera Martín** möchte ich für die Unterstützung bei den biomechanischen Messungen danken. **Dr. Nora Freyer** gilt mein Dank für die technische Hilfe bei den Glucose- und Lactatmessungen. Herzlichen Dank auch an die Mitglieder der BIH Stem Cell Core Facility **Judit Küchler**, **Kristin Fischer**, **Tanja Fisch** und **Janine Cernoch** für die Bereitstellung der hiPSCs, die Einweisung ins FACS und die Aushilfe

mit Materialien, wenn mal etwas gefehlt hat. Des Weiteren danke ich **Christian Hennig** und **David Holst** für die ausgezeichneten LabVIEW Kurse und Hilfestellungen.

Herzlichen Dank an die Mitglieder meiner Arbeitsgruppe **Dr. Laura Hildebrand, Dr. Bella Roßbach, Dr. Krithika Hariharan, Su-Jun Oh, Dr. Nancy Mah, Dr. Imran Ullah, Ngo Thi Thanh Thao, Enrico Fritsche, Dr. Raed Abu Dawud, Alexandra Lasch** und **Lilas Batool**. Sie haben mir nicht nur fachlich zur Seite gestanden, konstruktiv Ergebnisse mit mir diskutiert, Zellfütterungen am Wochenende übernommen oder bei Misserfolgen ein offenes Ohr für mich gehabt, sondern auch immer den Laboralltag mit Leben und Freude gefüllt. Ihr habt die letzten Jahre zu einer so schönen Zeit für mich gemacht.

Es war ein großer persönlicher Gewinn die Promotion als Mitglied der Graduiertenschule **Berlin-Brandenburg School for Regenerative Therapies (BSRT)** zu absolvieren. Daher gilt mein Dank **Dr. Sabine Bartosch**, der Koordinatorin der BSRT. Die Teilnahme an zahlreichen Kursen und Retreats, die Möglichkeit dank BSRT-Reisestipendien an internationalen Kongressen teilzunehmen, sowie die Erfahrung ein eigenes Symposium zu organisieren hat mich nicht nur wissenschaftlich, sondern auch persönlich wachsen lassen. Besonderer Dank gilt meinen „BSRT-Klassenkameraden“ **Dr. Maria Schneider, Christos Nikolaou, Dr. Stefan Sieber, Dr. Leila Amini** und **Constantin Thieme**, in deren Gesellschaft die Kurse, Retreats und Konferenzen zu besonderen Erlebnissen wurden.

Zu guter Letzt möchte ich mich ganz besonders bei meiner **Familie** und meinen **Freunden** bedanken. Ein riesiges Dankeschön geht an meine Eltern **Sabine Fischer** und **Joachim Fischer**, sowie an **Dr. Karl Schlumbach, Sebastian Fischer, Alfonso López Alloza** und **Vera Florian**. Euch allen danke ich dafür, dass ihr mich immer wieder ermutigt und bestärkt und für wunderbare Ablenkung gesorgt habt. Gemeinsames Wühlen im Garten am Wochenende oder ackern auf dem Weinberg in Spanien haben mich im wahrsten Sinne des Wortes immer wieder geerdet. Ich bin euch so dankbar für eure unermüdliche Unterstützung. Ohne euch wäre es nicht möglich gewesen!